

**University of Alberta**

**Conductive Atomic Force Microscopy Study of Electron Transport  
Through Diazonium Derived Films and Mixed – Mode Bonded  
Layers on Gold and Carbon Surfaces**

by

**Michael Shawn Reid**

A thesis submitted to the Faculty of Graduate Studies and Research  
in partial fulfillment of the requirements for the degree of

**Master of Science**

**Chemistry**

©Michael Shawn Reid

Spring 2012

Edmonton, Alberta

Permission is hereby granted to the University of Alberta Libraries to reproduce single copies of this thesis and to lend or sell such copies for private, scholarly or scientific research purposes only. Where the thesis is converted to, or otherwise made available in digital form, the University of Alberta will advise potential users of the thesis of these terms.

The author reserves all other publication and other rights in association with the copyright in the thesis and, except as herein before provided, neither the thesis nor any substantial portion thereof may be printed or otherwise reproduced in any material form whatsoever without the author's prior written permission.

## Abstract

For Molecular Electronics to become a viable replacement or complement to current electronic devices a fundamental understanding of device operation and functionality is needed. This work explores electron transport through diazonium derived molecular junctions via conductive atomic force microscopy to provide insight into the scalability of molecular devices. The attenuation coefficient and electron transport properties of nitroazobenzene on carbon; were found to be consistent with larger ensemble molecular junctions. Further, applied force significantly decreased the resistance through the layer due to reduced tunneling distance and increased contact area. Electron transport through nitroazobenzene was extended to gold surfaces and found to be in agreement with studies on carbon. Investigation of mixed-mode bonded layers of nitroazobenzene and dodecanethiol determined that surface coverage was controllable through solution concentration and sweep rate. Qualitatively it was observed that conductivity increased with nitroazobenzene coverage.

## Acknowledgements

I would like to extend a great deal of thanks and appreciation to those who I have worked and studied with throughout my time at the University of Alberta. I would like to thank my research supervisor Dr. Mark McDermott for his guidance throughout my studies. In addition my appreciation goes to the McCreery group, particularly Adam Bergren for his help getting the cAFM up and running, as well as his aid with the Simmons model. Thanks to my fellow group members for your insight and many discussions.

Much love and thanks to my great friends Sarah and Kyle. For your friendship I am forever indebted to you both. Although it seems that our adventure from Guelph to Edmonton has come to a close, it will never be forgotten and has shaped the rest of my life. I am certain we will share many more great times together. Shawn, Amelia and Marco, my time in Edmonton would not have been the same without your friendship, thank you.

To my family, I can't thank you enough for all your love and support, without it I could not have even hoped to be where I am today. I am looking forward to coming home.

Most of all I would like to express my love and thanks to Laura. Although at times I have been thousands of miles away, your love and support has spurred me forward. You are the best thing to ever happen to me and I cannot wait to spend everyday with you.

# Contents

<b>1</b>	<b>Introduction</b>	<b>1</b>
1.1	Molecular Electronics . . . . .	1
1.2	Molecular Junctions . . . . .	3
1.3	Measurement Paradigms . . . . .	5
1.3.1	Single Molecule Junctions . . . . .	5
1.3.2	Ensemble Molecular Junctions . . . . .	8
1.3.3	Conductive Atomic Force Microscopy . . . . .	10
1.4	Molecule Specific Molecular Junctions . . . . .	12
1.4.1	Self-assembled Monolayers . . . . .	12
1.4.2	Diazonium Derived Molecular Junctions . . . . .	13
1.5	Objectives . . . . .	15
<b>2</b>	<b>Probing Electron Transport Through Aryl Films on Carbon Surfaces with Conducting AFM</b>	<b>23</b>
2.1	Introduction . . . . .	23
2.2	Experimental . . . . .	26
2.2.1	Substrate Preparation . . . . .	26
2.2.2	Diazonium Salt Preparation and Surface Modification . . . . .	26
2.2.3	Atomic Force Microscopy Imaging and Film Thickness Measurements	27
2.2.4	Conductive Atomic Force Microscopy . . . . .	27
2.2.5	Scanning Electron Microscopy Tip Characterization . . . . .	28
2.3	Results and Discussion . . . . .	28
2.3.1	Modification of Conventional AFM for cAFM Measurements . . . . .	28
2.3.2	Topographic Characterization . . . . .	29
2.3.3	Effects Governing Electron Transport Through NAB Layers . . . . .	30
2.3.4	Molecular Layer Electron Transport Properties . . . . .	39
2.3.5	Junction Stability . . . . .	42
2.3.6	Conclusion . . . . .	43
<b>3</b>	<b>Diazonium Surface Modification and Characterization</b>	<b>47</b>
3.1	Introduction . . . . .	47
3.2	Experimental . . . . .	49

3.2.1	Substrate Preparation . . . . .	49
3.2.2	Diazonium Synthesis and Surface Modification . . . . .	49
3.2.3	Infrared Reflection Absorption Spectroscopy . . . . .	50
3.2.4	X-Ray Photoelectron Spectroscopy . . . . .	50
3.2.5	Atomic Force Microscopy Imaging and Film Thickness Measurements	50
3.3	Results and Discussion . . . . .	51
3.3.1	Deposition and Spectroscopic Characterization of Nitroazobenzene Diazonium salt on gold . . . . .	51
3.3.2	Investigation of Nitroazobenzene Diazonium Salt Deposition on gold .	53
3.3.3	Analysis of Multilayer Formation of NAB Layers. . . . .	59
3.4	Conclusion . . . . .	62
<b>4</b>	<b>Electron Transport Through Mixed-Mode Bonded Layers on Gold</b>	<b>67</b>
4.1	Introduction . . . . .	67
4.2	Experimental . . . . .	69
4.2.1	Template Stripped Gold . . . . .	69
4.2.2	Conductive Atomic Force Microscopy Tip Fabrication . . . . .	70
4.2.3	Surface Modification . . . . .	70
4.2.4	Infrared Reflection Adsorption Spectroscopy . . . . .	70
4.2.5	Atomic Force Microscopy . . . . .	71
4.2.6	Conductive Atomic Force Microscopy . . . . .	71
4.2.7	Scanning Electron Microscopy . . . . .	71
4.3	Results and Discussion . . . . .	71
4.3.1	Template Stripped Gold . . . . .	71
4.3.2	Spectroscopic Characterization of Mix-Mode Bonded Layers . . . . .	72
4.3.3	Topographic Characterizations of Mix-Mode Bonded Layers . . . . .	74
4.3.4	Characterization of Fabricated cAFM Tips . . . . .	82
4.3.5	Electron Transport Through Molecular Layers on Gold . . . . .	83
4.3.6	Electron Transport Through Mixed-Mode Bonded Layers on Gold . .	88
4.3.7	Inconsistencies within cAFM Measurements of Mixed Mode Bonded Layers . . . . .	90
4.3.8	Modified cAFM Tip Stability . . . . .	92
4.3.9	Conclusion . . . . .	93

<b>5</b>	<b>Conclusions and Future Work</b>	<b>98</b>
5.1	Conclusions . . . . .	98
5.2	Future Work . . . . .	99
<b>6</b>	<b>Appendix</b>	<b>103</b>
6.1	Simmons Model . . . . .	103
6.2	Conductive AFM Reproducibility . . . . .	104

## List of Tables

2.1	Calculated contact area, $A$ , and layer penetration, $\Delta d$ , for various NAB film thicknesses and applied forces. . . . .	38
2.2	Values for dielectric constant, $\epsilon$ , effective electron mass, $m_e$ , and electron transport barrier, $\phi_o$ , of NAB films at constant force (200 nN) as determined by the Simmons model. . . . .	40
2.3	Values for dielectric constant, $\epsilon$ , effective electron mass, $m_e$ , and electron transport barrier, $\phi_o$ , for 4.1 nm NAB film as determined by the Simmons model. Corrected effective electron mass in parenthesis. . . . .	40
3.1	Film thicknesses as determined by AFM scratching measurements. Errors reported are the standard deviations of the cross sectional average of NAB films. . . . .	62
4.1	Calculated percent diazonium coverage as determined by AFM, for 50 $\mu\text{M}$ and 250 $\mu\text{M}$ NAB mixed NAB/DDT layers . . . . .	78
4.2	Values for dielectric constant, $\epsilon$ , effective electron mass, $m_e$ , and electron transport barrier, $\phi_o$ , of 3.0 NAB and DDT as determined by the Simmons model. . . . .	87
4.3	Values for dielectric constant, $\epsilon$ , effective electron mass, $m_e$ , and electron transport barrier, $\phi_o$ , of mixed NAB/DDT films at various NAB percent coverages as determined by the Simmons model . . . . .	91

## List of Figures

1.1	Simplified energy level diagram of a molecular rectifier. . . . .	1
1.2	Schematic energy level diagram of (a) coherent and (b) incoherent tunneling across a molecular layer (grey) between two metals ( $M_1$ and $M_2$ ). Yellow represents filled states within the contacts. . . . .	3
1.3	Examples of Single molecule molecular junctions . . . . .	6
1.4	Schematic diagram of the formation of a break junction via gold STM tip. . . . .	7
1.5	Schematic of ensemble junctions, a) SAM bilayer formed by mercury drop electrode, b) the use of protective layer within vapour deposited SAM molecular junctions, c) vapour deposited electrodes, deposited directly on molecular layer. . . . .	9
1.6	Schematic diagram of cAFM measurement of alkanethiols using a gold coated AFM probe . . . . .	11
1.7	Schematic diagram of the formation of self-assembled monolayers. a) adsorption from solution, b) “standing up” nucleation, c) monolayer formation. Grey and red represent thiol and thiolate molecules respectively. . . . .	12
1.8	Proposed formation of diazonium salt molecular layers through radical formation, and subsequent multilayer formation . . . . .	14
2.1	Schematic of dodecanethiol self-assembled monolayers on gold displaying kinked chains and pinhole defects. . . . .	23
2.2	Schematics of various molecular junctions. a) scanning tunneling microscopy measurement of a molecular wire embedded in a mixed monolayer b) break junction c) conductive atomic force microscopy measurement of nitroazobenzene d) large area molecular junction. . . . .	24
2.3	Components used for modified conductive atomic force microscopy assembly. a) insulating acrylic sample holder displaying copper clip and cut-outs b) placement of sample within holder c) disassembled cantilever holder d) cantilever holder and wire attachment e) IV curve of dodecanethiol on gold. . . . .	28
2.4	AFM tapping mode height images of a) $5 \mu m^2$ bare PPF, b) $1 \mu m^2$ bare PPF, c) $5 \mu m^2$ NAB deposited at 200 mV/s, d) scratched image of c), e) $5 \mu m^2$ NAB deposited at 50 mV/s, f) scratched image of e). Z-scale in all images is 10 nm. . . . .	30

2.5	Current voltage measurement of a 2.5 nm NAB film on PPF at 50 nN and 100 nN applied force. . . . .	31
2.6	Current voltage measurement of a 4.1 nm NAB film on PPF at various applied forces. . . . .	31
2.7	Current voltage measurement of a 4.5 nm NAB on PPF under various applied forces. Note the reduced scale for clarity. Inset full scale IV measurement displaying behaviour at higher forces. . . . .	32
2.8	Current voltage measurement of a 6.1 nm NAB on PPF under various applied forces. Note the reduced scale for clarity. Inset full scale IV measurement displaying behaviour at higher forces. . . . .	32
2.9	Current voltage measurement at constant applied force (100 nN) for various film thicknesses. . . . .	34
2.10	Current voltage measurement at constant applied force (200 nN) for various film thicknesses. . . . .	34
2.11	$\ln(I)$ against layer thickness at 200 nN and 100 nN. Determination of attenuation coefficient, $\beta$ . . . . .	35
2.12	Typical force/distance curve for withdraw of AFM tip from the surface. . . .	35
2.13	10.0 kV high resolution SEM images of unused cAFM tips, a) along cantilever axis, b) rotated approximately $90^\circ$ . . . . .	36
2.14	Schematic of contact area calculation under the approximation of a spherical cap. Maximum possible contact area for each film thickness upper right. . . .	37
2.15	$\ln(I)$ voltage measurements (open circles) of NAB films with Simmons model fit (solid line) a) constant force (200 nN) and b) constant film thickness (4.1 nm). . . . .	40
2.16	10.0 kV high resolution SEM image of used cAFM tips, showing damage resulting from current voltage measurements. . . . .	42
3.1	Proposed mechanism of NAB layer deposition. NAB diazonium salt is reduced to form a radical intermediate which bonds to the electrode surface capable of multilayer formation . . . . .	47
3.2	Schematic depiction of the concentration difference between a) adsorption controlled and b) diffusion controlled deposition. Grey circles represent molecules which participate in electron transfer. Dashed line is included for visual aid. .	48

3.3	Cyclic voltammograms of 1 mM NAB diazonium salt solution deposited at 10 mV/s on gold . . . . .	51
3.4	Infrared Reflection Absorption spectrum of a NAB layer deposited from 1 mM solution at 10 mV/s on gold . . . . .	52
3.5	X-ray Photoelectron spectrum of the N1s region of a NAB layer deposited from 1 mM solution at 10 mV/s. . . . .	52
3.6	50 mV/s cyclic voltammogram of NAB diazonium salt solution at various concentrations on gold . . . . .	54
3.7	Cyclic voltammograms of 1 mM NAB diazonium salt solution deposited at various sweep rates on gold. . . . .	55
3.8	$\log(i_p)$ $\log(\nu)$ plot of NAB deposition at various concentrations. Inset shows the slopes determined for each concentration. . . . .	55
3.9	Proposed pathways for diazonium adsorption. Pathway 1) direct chemisorption from solution with rate constant $k_{ch}$ . Pathway 2) equilibrium between physisorption and desorption as determined by rate constants, $k_a$ and $k_d$ , followed by chemisorption . . . . .	57
3.10	5 $\mu\text{m}^2$ AFM tapping mode images a) bare gold substrate b) scratched gold substrate c) 500 $\mu\text{M}$ NAB layer deposited at 10 mV/s on gold d) scratched 500 $\mu\text{M}$ NAB layer deposited at 10 mV/s on gold. The z-scale for all images is 20 nm . . . . .	60
3.11	Film thicknesses as determined by AFM scratching measurements. . . . .	60
3.12	A) a single NAB molecule adsorbed along the surface normal B) Proposed multilayered structure of NAB films. . . . .	61
4.1	Schematic representation of the difference between mixed organic layers a) mixed alkanethiols, b) diazonium derived . . . . .	68
4.2	Simplified view of the template stripped process where grey: clean silicon wafer, yellow: gold, black: mounting substrate . . . . .	69
4.3	Atomic force microscopy height images of bare (left) thermal evaporated gold (right) template stripped gold. Z-scale 10 nm. . . . .	72
4.4	IRRAS spectra of (left) $\text{NO}_2$ stretching region and (right) C-H stretching regions for NAB modified (blue) and NAB/DDT modified (red) molecular layers. (a,b) 250 $\mu\text{M}$ NAB at 10 mV/s, (c,d) 250 $\mu\text{M}$ NAB at 200 mV/s, (e,f) 50 $\mu\text{M}$ NAB at 50 mV/s . . . . .	73

4.5	AFM height images of modified template stripped gold, a) dodecanethiol, b) nitroazobenzene c) mixed NAB/DDT layer. Z-scale 10 nm. . . . .	75
4.6	Schematic representing the influence of surrounding material on size measurements in AFM . . . . .	75
4.7	AFM images of NAB/DDT layer deposited at 200 mV/s from (top) 250 $\mu$ M NAB solution, (bottom) 50 $\mu$ M NAB solution. Height, amplitude and phase images are displayed for each concentration with z-scales of 10 nm, 0.1 V and 30° respectively. . . . .	76
4.8	Schematic representation of mixed NAB/DDT structure . . . . .	77
4.9	AFM height images of mixed NAB/DDT layers along with their respective thresholded images deposited by a) 250 $\mu$ M NAB at 100 mV/s, b) 250 $\mu$ M NAB at 200 mV/s, c) 50 $\mu$ M NAB at 100 mV/s. Z-scale 10 nm. . . . .	78
4.10	High resolution secondary electron SEM images of mixed layers deposited from 250 $\mu$ M NAB at 200 mV/s a) inside the o-ring NAB deposition area b) outside NAB deposition region that contains only a monolayer of DDT. . . . .	81
4.11	Schematic representation of a) interaction volume and b) secondary escape volume, in SEM imaging. Within b) it can be seen that angled samples produce larger secondary electron escape volumes. . . . .	81
4.12	High resolution secondary electron SEM images of (top) bare and (bottom) gold modified silicon nitride AFM tips . . . . .	82
4.13	Current voltage curve of NAB on template stripped gold for various film thicknesses . . . . .	84
4.14	Current voltage curve for DDT on template stripped gold . . . . .	84
4.15	Current voltage curve for 3.0 nm NAB film and DDT monolayer . . . . .	85
4.16	a) $\ln(I)$ vs. <i>Layer Thickness</i> of NAB on template stripped gold measured at 0.5 V for $\beta$ determination b) $\ln I $ current voltage curves of (open circles: red) 3.0 nm NAB and (open circles: purple) DDT on template stripped gold along with there respective Simmons model fits (solid line) . . . . .	87
4.17	Current voltage measurements of mixed NAB/DDT at various NAB densities deposited from 250 $\mu$ M NAB solution . . . . .	89
4.18	Current voltage measurements of mixed NAB/DDT at various NAB densities deposited from 50 $\mu$ M NAB solution . . . . .	89

4.19	Current voltage measurements of mixed NAB/DDT layers with 64% and 68% NAB coverages . . . . .	91
4.20	$\ln(I)$ current voltage measurements (open circles) of mixed NAB/DDT films with Simmons model fit (solid line) deposited from 250 $\mu\text{M}$ NAB solution . .	91
4.21	High resolution secondary electron SEM images of used “in house” modified cAFM tips using 10.0 kV . . . . .	93
6.1	Representative unaveraged conductive atomic force microscopy current volt- age curves . . . . .	105

## Nomenclature

$\beta$	attenuation coefficient
$\Delta d$	penetration depth
$\mu\text{m}$	micrometer
$\phi_o$	barrier height
$\varepsilon$	dielectric constant
$\text{\AA}$	angstrom
a	contact radius
AFM	atomic force microscopy
Ar	Argon
$\text{Bu}_4\text{NBF}_4$	tetrabutylammonium tetrafluoroborate
cAFM	conductive atomic force microscopy
$\text{cm}^{-1}$	wavenumbers
d	layer thickness
DDT	dodecanethiol
eV	electron volts
h	Plancks constant
HOMO	highest occupied molecular orbital
I	current
IRRAS	infrared reflection absorption spectroscopy
IV	current voltage
J	current density
JKR	Johnston-Kendal-Roberts
K	Kelvin

LUMO	lowest unoccupied molecular orbital
$m_e$	effective electron mass
NAB	Nitrazobenzene
nm	nanometers
nN	nanonewton
OPI	oligophenyleneimine
PDMS	poly(dimethylsiloxane)
PPF	pyrolyzed photoresist film
TCCM	thin coating contact model
V	voltage
XPS	X-Ray photoelectron spectroscopy

# 1 Introduction

## 1.1 Molecular Electronics

The beginning of the field “Molecular Electronics” is often referenced to Aviram and Ratner’s 1974 paper “Molecular Rectifiers” [1], in which uni-directional electron transport was modeled through a single organic molecule. Within their work, it was proposed that by controlling the  $\pi$ -electron density of aromatic substituents, specific regions of the molecule would be electron-rich (n-type) or electron-poor (p-type) and act as donors and acceptors respectively. By including a central  $\sigma$ -bonded species a donor-bridge-acceptor (DBA) molecule would have roughly the same electronic properties as a rectifying p-n junction. Figure 1.1a displays a schematic energy level diagram of an acceptor-bridge-donor molecular system at neutral bias. Within this, it is important to note that molecular orbitals of the acceptor ( $\pi_a$ ) to the donor ( $\pi_d$ ) remain separate due to the inclusion of the  $\sigma$ -bonded internal tunneling barrier. At neutral bias, the Fermi level ( $E_f$ ) of the contacts (anode and cathode) lie (energetically) between the highest occupied molecular orbital (HOMO) and lowest unoccupied molecular orbital (LUMO) of the DBA molecule. As a result, no charge transport is expected to occur since there are no “open” electronic states in which electrons from the contacts can occupy. Under the application of a forward bias, Figure 1.1b, the Fermi level of

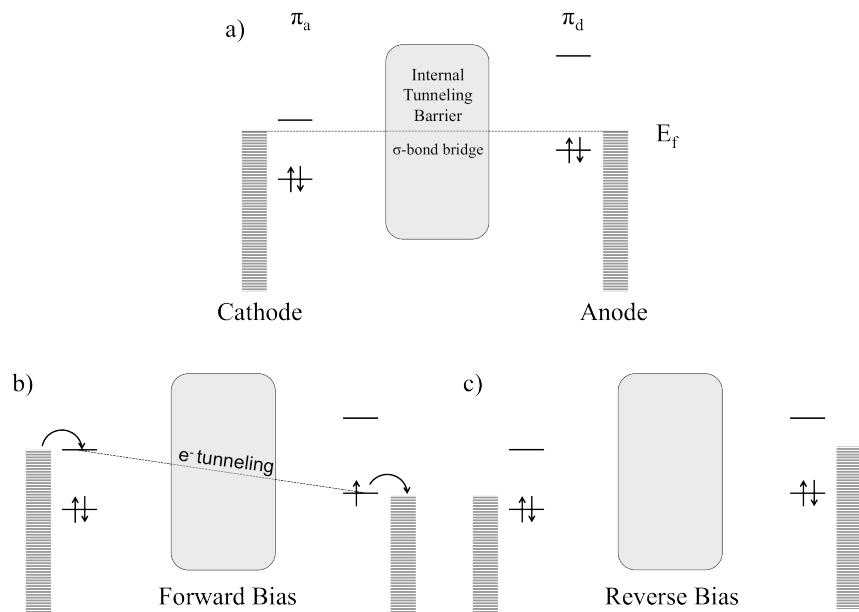


**Figure 1.1:** Simplified energy level diagram of a molecular rectifier.

the cathode is raised such that electrons can enter the LUMO of the acceptor. Similarly, as the Fermi level of the anode is reduced electrons from the donor HOMO enter the now open electronic states of the contact. As a result, the electrons from the (now occupied) acceptor LUMO can tunnel through the  $\sigma$ -bonded region into the open electronic state of the donor HOMO, allowing current to flow between the contacts. Conversely, under reverse bias, Figure 1.1c, it is that energetically there are no open states within the DBA molecule to allow electron transport between the contacts. Based on these principles Aviram and Ratner were able to calculate that a single organic molecule would display electronic behavior similar to a p-n junction rectifier[1].

It was from this that researchers began to imagine exploiting the unique and diverse properties of organic molecules to achieve specific electronic functions. Although still emerging the field has subsequently expanded, and grown to encompass a wide breadth of research, from fundamental electron transport studies of single molecule junctions[2] to complete electronic devices such as organic light emitting diodes [3] and organic solar cells[4]. Molecular Electronics however, strictly refers to a subset of organic devices that are created and operated on the molecular scale. The drive behind much of this research is based on a two key motivations. Firstly, the consistent progress of semi-conductor industry, as famously stated by Moore's law, predicts that transistor density doubles every two years. In order to maintain growth it is important that electronic devices become progressively smaller. There will come a time however, in which either manufacturing techniques[5] or stability (thermal noise)[6] will ultimately limit the size of semi-conductor components. A single molecule device has the potential to be orders of magnitude smaller than current state of the art devices, allowing for device density to increase according to Moore's law[5, 7]. Second, chemists have the ability to synthesize a variety of molecules with specific chemical and electronic structures from which electronic devices such as transistors, switches, rectifiers etc. can be created.

Although Molecular Electronics display great promise, there exists major hurdles that need to be addressed in order for molecular devices to be a practical replacement for current electronics. In terms of manufacturing, the semi-conductor industry has shown itself capable of mass producing sub 50 nm devices with extremely high yield [5, 8]. Furthermore, the electron transport within these systems has been thoroughly investigated and is well understood. In order for molecular electronics to become viable it is important that small scale devices be created in parallel and with predictable electronic behaviour[7]. In addition,

based on current technology, a critical aspect in the development of any molecular device will be its integration with conventional electronics. As a result, it is important to fully understand electron transport behaviour through molecular systems and how it is affected by its surrounding environment (temperature, pressure, contact material, etc.).

## 1.2 Molecular Junctions

A common stage for studying electron transport is the molecular junction[7]. Following the definition outlined by McCreery [9], molecular junctions are systems in which one or more molecules are in electrical contact with two conductors, such that electrons are transmitted through the molecule. Although literature has long shown examples of organic materials between electrical components, conducting polymers and organic thin film capacitors[10, 9], these devices typically involve layers that are substantially larger than molecular dimensions. In addition, although systems involving donor-bridge-acceptor molecules (excluding contacts) and modified electrodes (one contact) do display electron transport on the molecular scale, many of these systems do not exhibit transport behaviour seen in molecular junctions and are thus excluded from the definition. Charge transport through molecular junctions has been described to occur via a number of routes; the Poole-Frenkel effect, field emission (Fowler-Nordheim), thermionic (Schottky) emission and most commonly, coherent and incoherent tunneling[11] which will be discussed below, Figure 1.2[9].

Simplistically, electron tunneling, Figure 1.2, is quantum mechanically governed by the

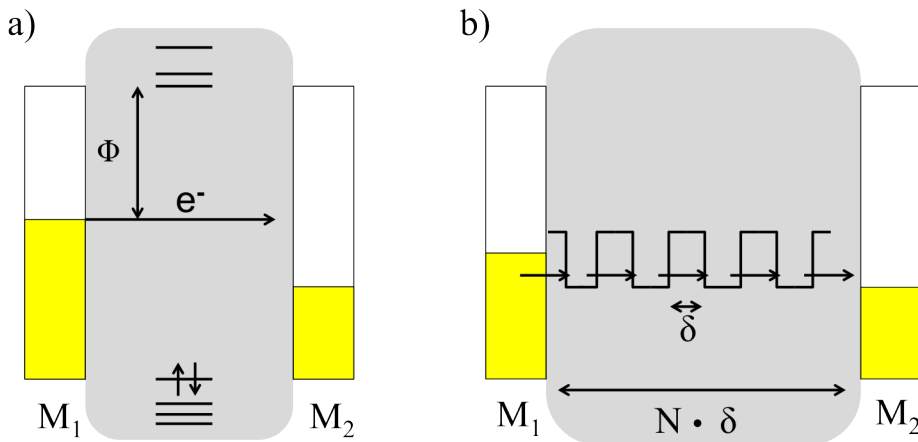


**Figure 1.2:** Schematic energy level diagram of (a) coherent and (b) incoherent tunneling across a molecular layer (grey) between two metals (M<sub>1</sub> and M<sub>2</sub>). Yellow represents filled states within the contacts.

probability that an electron will transverse a barrier. Independent of temperature[12, 13], the probability, and thus the rate of electron transport, is significantly dependent on the height and thickness of the barrier. Within molecular electronics a common method used to describe electron transport, or current density  $J$ , as a function of voltage,  $V$ , is the Simmons model[13, 14, 15, 16]:

$$J = \frac{q^2 V}{h^2 d} (2m\Phi)^{1/2} \exp \left[ \frac{-4\pi d}{h} (2m\Phi)^{1/2} \right] \quad (1.1)$$

where  $q$  and  $m$  are the electron charge and mass respectively,  $d$  is the barrier distance (or thickness),  $h$  is Planck's constant and  $\Phi$  is the barrier height. Formulated in 1963 by J. G. Simmons, the model describes inelastic nonresonant tunneling through an insulating barrier[17, 18, 19]. Within this, it is assumed that the potential barrier is spatially averaged and varies linearly with space and applied bias[15]. From Equation 1.1, current through the molecular junction is both linearly and exponentially dependent on barrier thickness and barrier height. In order to understand and compare experimental and theoretical results it is often useful to simplify Equation 1.1 to:

$$I = I_o e^{-\beta d} \quad (1.2)$$

where  $I_o$  is a constant and  $\beta$ , the attenuation coefficient has units of  $\text{\AA}^{-1}$  or  $\text{nm}^{-1}$ . It should be noted that Equation 1.2 has been described as both current density,  $J$ , or absolute current,  $I$ , as in Chapter 2. Dependent on the chemical and structural properties of the barrier, particularly the molecule - contact bond, the value of the attenuation coefficient,  $\beta$ , is often an indication of barrier height and is used to distinguish between tunneling mechanisms[20, 21, 22] within the molecular layer and will be discussed further below.

Coherent or classical tunneling, is typically described as electron transfer through a single barrier (the molecule in the case of molecular junctions) while maintaining the phase of the electron. Figure 1.2a displays an energy level diagram for coherent tunneling across a molecular junction. The barrier height,  $\Phi$ , is typically considered to be the difference between the Fermi level of the contacts and the molecular orbital energies. As in many forms of tunneling, the height and width of the barrier play a significant role in determining the probability of transport. As a result, it has been found that coherent tunneling across molecular junctions is limited to distances less than 3 nm and is described by attenuation coefficients of 5 - 10  $\text{nm}^{-1}$  [9, 21, 23, 24, 25].

Unlike coherent tunneling, in which a single electron tunneling event occurs, incoherent or “diffuse” tunneling can be thought as electron transport via series of discrete steps[9, 26, 11]. Within this process electrons tunnel coherently between sites, characterized by potential wells, where residence time is long enough to disrupt the phase of the electron. By considering Figure 1.2b the molecular layer can be visualized as a series of potential wells of length  $\delta$ . The total barrier width as a result is  $N \cdot \delta$  where  $N$  is the number of potential wells in the layer. During charge transport, electrons tunnel between individual sites giving rise to measurable current across the contacts. Currently it is not completely clear how diffuse tunneling occurs but it has been suggested that it is resultant from an electron transfer reaction between ionic and neutral sites in  $\pi$ -conjugated molecular systems[27]. Though the use of the Simmons model is not strictly valid when considering diffuse tunneling[15], Equation 1.2 is often applied to experimental results in order to determine  $\beta$  and provide insight into molecular layer properties. Many studies of molecular junctions derived from diazonium and thiol based molecular layers have found that diffuse tunneling can occur over much larger distances than coherent tunneling ( $> 3\text{nm}$ ) and yield attenuation coefficients of less than  $5 \text{ nm}^{-1}$ [13, 28, 20].

Resulting from the series of discrete steps within diffuse tunneling, it has been proposed that electron transport through molecular layers greater than 4 nm in thickness occurs via thermally activated “hopping”[12, 23, 29, 25]. Investigations by Frisbie and coworkers revealed significant changes in the attenuation coefficient as the molecular length of aromatic thiols was increased[25]. Variance in  $\beta$  suggest that the electron transport mechanism changes with layer thickness . This was further supported by thermally activated conduction observed in longer molecular chains and indicates that molecular rearrangement within the layer dictates electron transport.

## 1.3 Measurement Paradigms

### 1.3.1 Single Molecule Junctions

The establishment of scanning tunneling microscopy (STM) in 1981 by Binnig and Rohrer, ushered in a new era of surface science[30, 31]. By probing electronic surface states with tunneling current, Binnig and Rohrer were able to obtain atomically resolved images of many conductive and semi-conductive surfaces[31, 32]. It was from this, that further surface probe microscopies (SPM) were developed, most specifically (with regards to molec-

ular junctions) atomic force microscopy (AFM) and conductive atomic force microscopy (cAFM)[33]. Monitoring tunneling current through conductor and semi-conductor surfaces naturally progressed to electron transport studies of organic molecules on surfaces. The use of an atomically sharp tip allowed researchers to create molecular junctions involving single molecules[34]. Further development of single molecule junctions has subsequently divided transport studies into two broad regimes; isolating a molecule of interest within a molecular layer[35, 36, 37, 38], or bridging two electrodes with a single molecule (break junctions)[20, 39, 40, 41].

Many of the early measurements of single molecular junctions involved monitoring electron transport through thiol based self-assembled monolayers (SAMs) on gold (111) via STM, Figure 1.3[35, 36, 37, 38, 42]. Note thiol SAMs, particularly alkanethiols, have been the predominant platform in molecular electronics, and a detailed discussion of their use and formation is held in Section 1.4.1. Making use of an atomically sharp probe researchers were able to selectively measure individual molecules within the molecular layer, Figure 1.3a. Investigations of  $\alpha$ ,  $\alpha'$ -xylyl dithiol found that the current voltage curves obtained contained distinct steps, suggesting that electron transport is significantly impacted by the molecular energies of the molecule.[38, 35]. Within these studies however, due to the fact that the molecule of interest is contained within a uniform molecular layer it is not entirely

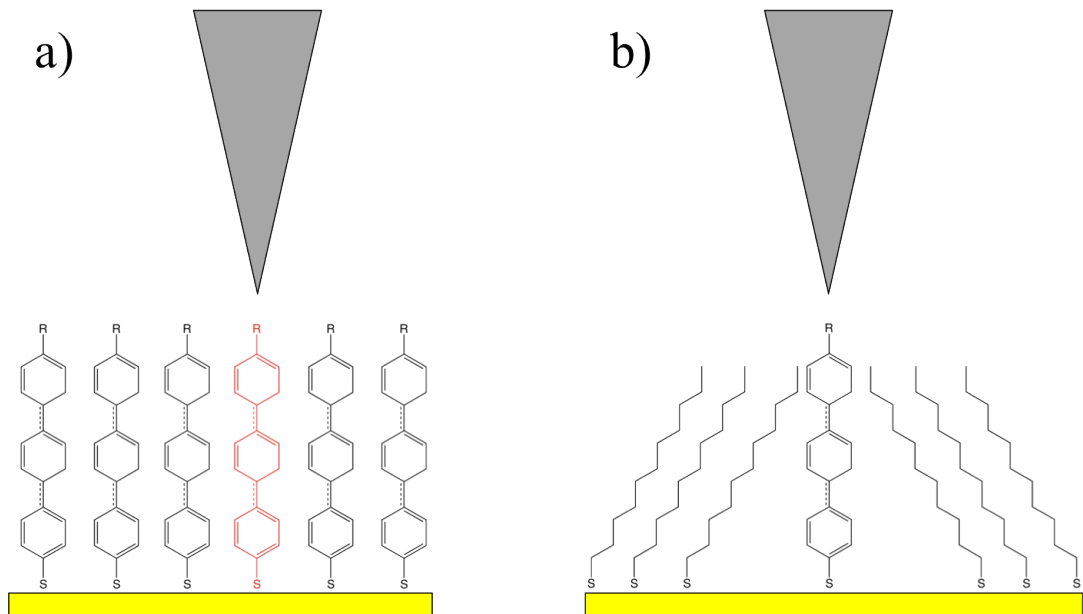


**Figure 1.3:** Examples of Single molecule molecular junctions

clear as to whether (only) a single molecule is being probed within each measurement.

In order to minimize the uncertainty resulting from the surrounding layer, researchers began to investigate molecular junctions of mixed monolayers. Similarly to studies of uniform molecular layers, mixed monolayers typically involved current voltage measurements of SAMs. Researchers were able to isolate conjugated thiols within a surrounding monolayer of alkanethiol, Figure 1.3b, as indicated by points of high conductivity distributed throughout the molecular layer[43, 36, 44, 45, 46]. It was further observed that the electron transport through the conjugated system, randomly “switched” between high and low conductance. It was proposed that conformational changes in the molecule altered the electron transfer within the molecular junction [36, 46].

Within the investigations of single molecule junctions contained in complete molecular layers, it is not entirely clear how the surrounding monolayer affects electron transport of an individual molecule. Within these systems it can no longer be assumed that the molecular energy levels of isolated molecules are maintained within the molecular layer. As a result, measurements of single molecular junctions within molecular layers do not represent the electron transport behaviour of isolated single molecules. In addition, within these measurements because the STM tip does not make contact with the surface, it is important to fully understand tip-molecule distance and its effect on electron transport due to the exponential relationship between distance and current, Equation 1.2.[34, 7, 47].

An important aspect of molecular electronics is the comparison of theoretical and experimental results. Generally molecular simulations rely on a well defined atomic positions

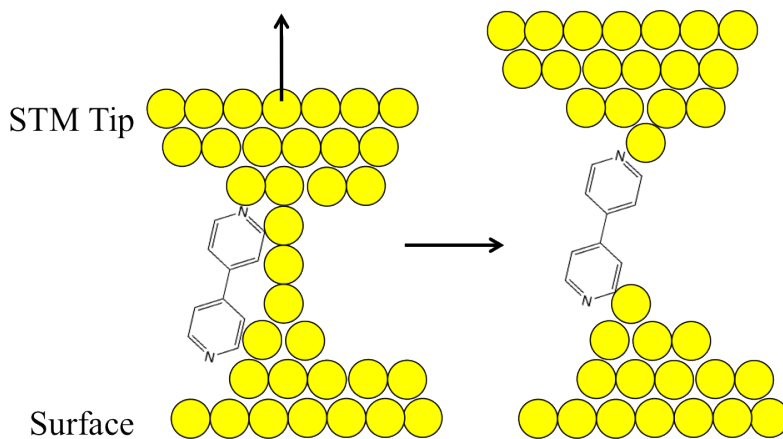


**Figure 1.4:** Schematic diagram of the formation of a break junction via gold STM tip.

and interactions[15]. As mentioned above within a monolayer the effect of the surrounding molecular layer is unclear, making it necessary to investigate isolated single molecule molecular junctions[48]. Many electron transport measurements of single molecules involve the use of break junctions, in which an (usually) isolated molecule bridges the gap between two contacts in solution, Figure 1.4. Measuring electron transport across an isolated molecule presents many technological challenges due to the fact that a microscopic structure needs to span a gap between two (generally) macroscopic electrodes[7, 49]. The gap within break junctions is generally formed through two distinct processes; mechanically breaking an electrode, or using high current to cause electromigration atoms[34]. Within each method a 1-2 nm gap is formed, however there is no control over the exact shape of the electrode and thus the geometry of the bridging molecule cannot be controlled[49]. The first use of molecular break junctions was reported in 1997 by Reed *et al.*, who mechanically broke a thin gold wire to study electron transport through phenyl-1, 4-dithiol molecules[50]. Xu and Tao; further developed break junctions by using gold STM tips to form and break gold nano filaments allowing for thousands of measurements and thus creating statistically significant data[2, 51]. Through this it was observed that conductance occurred in distinct steps and that contact geometry is an important factor in electron transport.

### 1.3.2 Ensemble Molecular Junctions

In contrast to single molecule junctions, where the geometry of an individual molecule significantly impacts electron transport, large molecular ensembles ( $>10^3$  molecules), Figure 1.5, generally exhibit transport behaviour resulting from the average molecular conformation and molecule-contact binding[34]. A distinct advantage within large area measurements is that junctions have been observed to be extremely stable over billions of cycles and at high temperatures [28, 52]. This is an important observation when considering integrating molecular systems with current electronics, where stability is of the utmost importance. Furthermore, many of the processes used to create large molecular junctions, such as metallic vapour deposition, are already in use within the semiconductor industry eliminating the need for substantial technological advancement [7, 53].

Historically, mercury has been a common platform to obtain clean, defect free, metallic surfaces[49]. Subsequently there have been numerous studies of molecular junctions using mercury drop electrodes. Within these studies there are two distinct approaches; depositing molecular layers on solid bottom electrodes and using a mercury drop to form the top

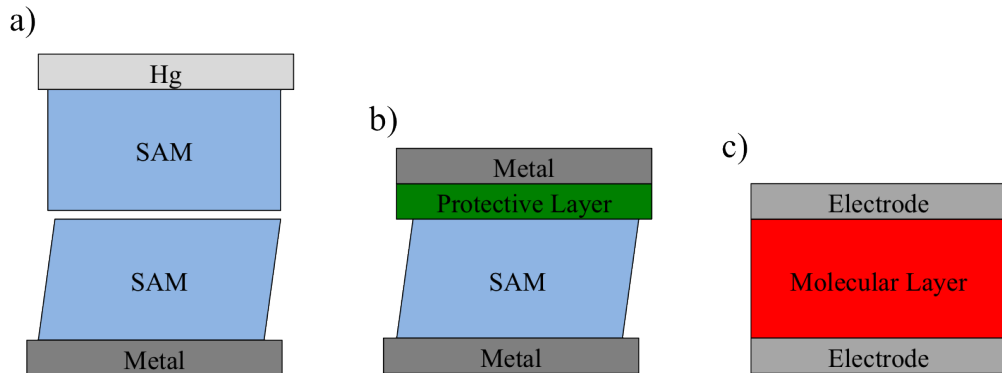


**Figure 1.5:** Schematic of ensemble junctions, a) SAM bilayer formed by mercury drop electrode, b) the use of protective layer within vapour deposited SAM molecular junctions, c) vapour deposited electrodes, deposited directly on molecular layer.

contact[54, 55, 56, 57], or forming molecular layers on two drops which are then brought into electrical contact[58, 59, 60, 61]. Note that electrochemical studies of alkanethiols in solution have been conducted using a mercury drop electrodes[62], however because only one electrical contact is present they are excluded here. Mercury drop molecular junctions involving SAMs typically result in the formation of bilayers due to the lability of the thiol molecules, Figure 1.5a [58, 59, 60, 61, 54]. Studies by Whitesides and coworkers have displayed that electron transport through bilayers of alkanethiols is reduced with increasing molecular chain length and that the defects within the molecular layer, resulting from the bottom electrode surface, lead to extreme changes in conductivity (8 orders of magnitude)[54]. McCreery and coworkers have previously used mercury drop electrodes to study electron transport through aromatic diazonium derived molecular layers on carbon[55, 56]. The current voltage behaviour was nearly independent of temperature and electron transport was altered by varying the thickness of the molecular layer. Note, a more detailed discussion of the work by McCreery and coworkers is held in Section 1.4.2.

Due to the toxicity and poor mechanical stability of mercury many researchers have transitioned to investigate molecular junctions formed by vapour deposition of solid metals[56]. Aside from the removal of toxic components and increased mechanical stability, vapour deposition offers three key advantages over mercury drop junctions. Firstly, through vapour deposition a variety of metals (Ag, Au, Ti, Cu, Pt) can be deposited, allowing researchers to investigate the effect of contact material on electron transport[52]. It is important to note that not all metals are suitable for molecular junctions, as some metallic atoms have

been observed to penetrate molecular layers causing short circuits and device failure[63, 64]. In order to increase device yield Akkerman *et al.* employed a conductive polymer to act as a “protective layer” which metallic contacts are deposited, Figure 1.5b [65, 53]. However, it is unclear what effect the protective layer has on electron transport, since the molecule-protective layer interface is ill defined. Second, by forming molecular junctions through vapour deposition, thousands of devices can be made in parallel[53] allowing researchers to gather statistically significant data. Finally, as mentioned above, the current semi-conductor industry employs vapour deposition in device formation, reducing the need for technological advancement in order to integrate molecular junctions[7].

Many thorough investigations of diazonium derived molecular junctions on carbon have been conducted by McCreery and coworkers. Typically metallic copper is vapour deposited directly onto the molecular layer[13, 66, 67], Figure 1.5c, forming micrometer sized junctions. Studies have shown that these molecular devices are stable through billions of cycles and a wide range of temperatures[28, 52], and are further discussed in Section 1.4.2.

### 1.3.3 Conductive Atomic Force Microscopy

Many researchers have shown that AFM is the most versatile, sensitive and procedurally straightforward tool within the field of nanotechnology[68]. Due to the fact that non-conductive surfaces can be studied, researchers have applied AFM to a countless number of systems including semi-conductor nanofabrication[69], cellular machinery[70], and synthetic polymers[71] to name a few. Depending on the stability of the surface, imaging can be conducted either in contact or non-contact mode. AFM imaging in contact mode involves bringing a sharp tip into physical contact with the surface. The deflection of the cantilever is monitored in feedback (typically by a laser) such that the force applied to the surface can be controlled with pico Newton precision[70]. Topographic and frictional information is obtained by monitoring the vertical and lateral deflection (respectively) of the cantilever as it moves across the sample via a piezoelectric scanner. Within non-contact mode, (typically) the cantilever is driven at resonance frequency such that the tip “taps” the surface as it is rastered, otherwise known as “tapping mode”. Under tapping mode, mechanical and adhesive properties of the surface can be obtained by monitoring the amplitude and phase shift of the oscillating tip (discussed further in Chapter 4).

One of the many extensions of AFM is conductive atomic force microscopy (cAFM), Figure 1.6. Typically a potential is applied to a metallized tip after it is brought into

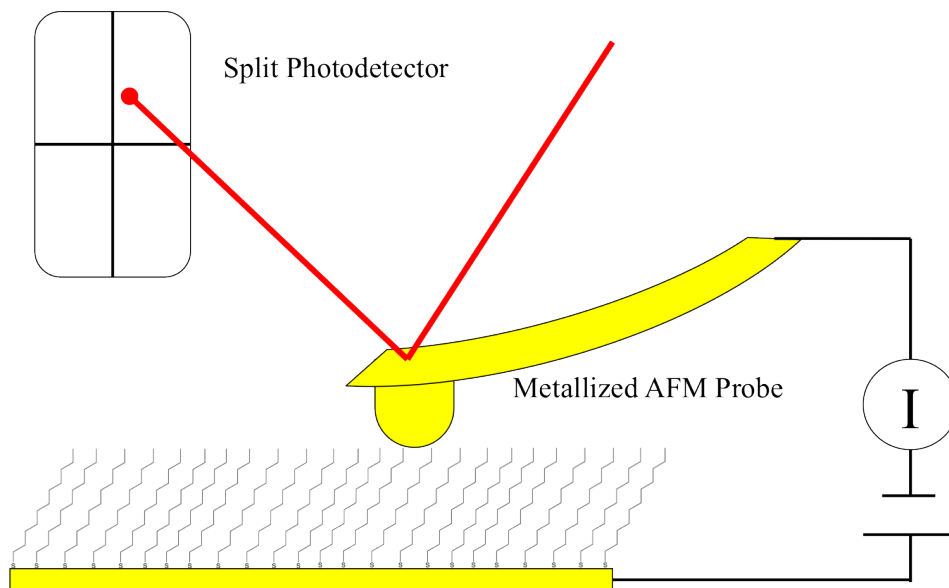


**Figure 1.6:** Schematic diagram of cAFM measurement of alkanethiols using a gold coated AFM probe

contact while monitoring the current through the sample. By rastering the tip across the sample under constant bias the conductivity of surface can be imaged[72]. In addition to imaging, by “holding” the probe at a particular location the current can be monitored under varying potential, providing insight into electron transport behaviour[73, 21, 74]. Although at its surface cAFM appears similar to its predecessor STM, there exists key fundamental differences in its methodology. Due to the fact that the cAFM probe makes physical contact with the surface there is no effect of tip-molecule distance on electron transport, as observed in STM [9, 34, 47]. Further, by monitoring the deflection of the cantilever, electron transport can be studied under various applied loads[21].

Within the above sections studies were separated by the number of molecules within the molecular junction; single molecule and ensemble junctions. Molecular junctions formed via cAFM however, typically do not involve individual molecules, but contact areas are significantly smaller than molecular junctions formed via vapour deposition and mercury drop electrodes[34, 9]. The number of molecules contained within cAFM junctions is not strictly understood[75] but observations by Frisbie *et al.* have estimated the number of molecules to be between 10 - 100s depending on the size of the molecular probe[76]. As a result, cAFM is an extremely useful technique, bridging the gap between single molecule and ensemble molecular junctions[77].

## 1.4 Molecule Specific Molecular Junctions

### 1.4.1 Self-assembled Monolayers

Thiol based self-assembled monolayers (SAM) have been at the forefront of not only molecular electronics, but many areas of surface science. Since their introduction by Nuzzo and Allara in 1983 [78], SAMs have seen prominent use in micro fabrication, surface wettability, biomedical systems, molecular recognition, bioassays, device fabrication, microcontact printing and nanoparticle functionalization [79, 63]. The wide application of SAMs over the past 30 years can be attributed to both the simple deposition procedure as well as the wide variety of ligands and functional groups that can be synthesized. Typically SAM formation occurs by molecules adsorbing to the surface from solution, Figure 1.7. Initially molecules “lay down” parallel to the substrate surface, Figure 1.7a. and as surface density increases the thiol molecules nucleate to form a “standing up” phase, Figure 1.7b. Finally complete monolayers are formed, Figure 1.7c, as molecules further adsorb. It should be noted that, SAMs are not perfect and structural defects, such as pinholes and kinked chains are common[63].

It is generally understood that the formation of well-ordered, dense monolayers arises from the nature of the gold-sulfur bond. At  $\sim 50 \text{ kcal mol}^{-1}$ [63] the sulfur-gold bond is much stronger than van der Waals forces seen in physisorbed species, but maintains a lability essential for reordering as surface density changes. Numerous studies have thoroughly characterized SAMs on a variety of surfaces (gold, copper, silver, etc.) and under various environmental conditions (temperature, redox species, etc)[79, 63].

The use of SAMs to form molecular junctions has been extensive[80, 81, 14, 82, 83, 60, 61, 21, 84, 54, 29, 59, 58, 85, 86, 25, 16, 87]. As a result, researchers have thoroughly investigated thiol based molecular junctions from those involving single molecules[50, 20, 23] to large scale massively paralleled ensemble systems[53, 65]. Note that single molecule

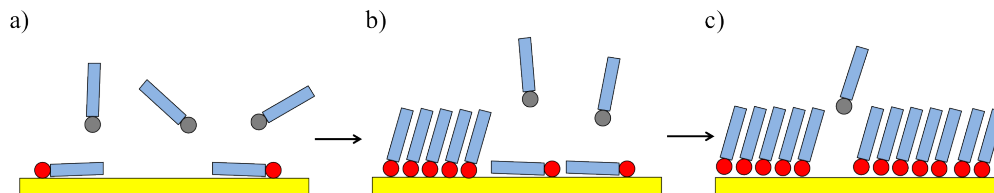


**Figure 1.7:** Schematic diagram of the formation of self-assembled monolayers. a) adsorption from solution, b) “standing up” nucleation, c) monolayer formation. Grey and red represent thiol and thiolate molecules respectively.

junctions are not technically monolayers however, because of the use of thiol molecules they are included here. Much of the popularity, as discussed above, is due to the ease of use and the formation of well defined monolayers. With regards to Molecular Electronics the fact that SAMs form spontaneously makes the formation of many devices in parallel a tangible prospect. Furthermore, having a well defined surface is important and allows researchers to compare theoretical and experimental results based on known tunneling distances, Equation 1.2.

Due to the vast use of thiols within molecular electronics it is useful to narrow the focus of studies to a few key investigations, notably the work by Frisbie and coworkers, who have extensively used cAFM to study electron transport through molecular junctions of SAMs on gold[21, 86, 88, 89, 25]. Initially their efforts were focused on characterizing electron transport under various applied forces and alkanethiol chain length. It was found that current voltage behaviour was consistent with coherent nonresonant tunneling and that the attenuation coefficient determined by cAFM ( $\sim 1 \text{ \AA}^{-1}$ ) was in good agreement with measurements of single and ensemble junctions[21]. It was further demonstrated that increasing the force applied to the surface significantly reduced the resistance across the junction, suggesting that increased contact area, tip penetration and conformational changes in the layer occurred at higher loads[84, 21]. Focus subsequently progressed to conjugated oligophenyleneimine (OPI) thiol molecular wires where fundamental tunneling mechanisms were investigated[24, 25]. It was observed that by increasing the length of the OPI wire, altered the value of the attenuation coefficient. It was concluded from this that electron transport transitioned from tunneling to thermally activated hopping at approximately 4 nm.

#### 1.4.2 Diazonium Derived Molecular Junctions

Aryl diazonium salts, although not as widely used as SAMs, have become a common platform for surface modification[90, 91, 92, 93, 94]. The electrochemical reduction of nitrobenzene diazonium salt at carbon surfaces was first reported by Pinson in 1992 [95]. From this, researchers have extended diazonium chemistry to numerous functional groups as well as deposition on various metals including gold, copper, platinum[96] as well as silicon [97]. Studies have subsequently displayed that diazonium derived molecular layers are very stable under thermal treatment[52], potential cycling in sulfuric acid [98] and ultrasonication[94], while also being stable for months under ambient laboratory conditions[95]. Chemists have

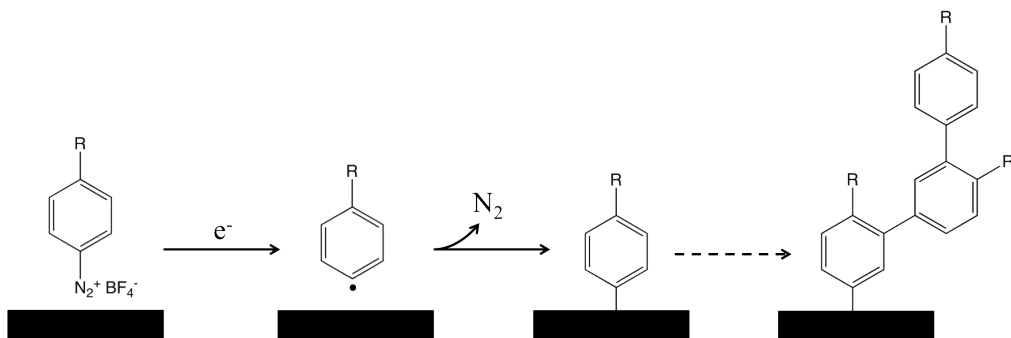


**Figure 1.8:** Proposed formation of diazonium salt molecular layers through radical formation, and subsequent multilayer formation

further tailored diazonium salts to a variety of applications ranging from fuel cells[99] to biological sensors[100, 101].

Shown in Figure 1.8, the formation of diazonium derived layers is believed to occur via the reduction of a diazonium cation producing a radical intermediate. The radical then irreversibly binds to the surface, due to the close proximity at which reduction occurred. From the radical nature in which the diazonium molecules adsorb, multilayered films have been observed[102]. Furthermore, by altering electrochemical conditions, sweep rate, concentration and number of cycles many studies have displayed over films of varying thickness[103, 66, 102, 104, 98]. Researchers have further observed that deposition can occur electrochemically[96, 39] as well as spontaneously[105, 91]. Within both electrochemical and spontaneous depositions it has been spectroscopically shown that the resulting film is covalently bound to both metal and carbon electrode surfaces [91, 96, 106].

Much of the research investigating electron transport through diazonium derived molecular layers has been spearheaded by McCreery and coworkers[107, 13, 52, 66]. They have extensively studied electron transport through ensemble molecular junctions ( $\mu m^2$ ) of nitroazobenzene and other diazonium layers on carbon, under various conditions. By using vapour deposition to form molecular junctions McCreery and coworkers have investigated a variety of contact materials and have recently displayed an all carbon molecular device[28]. Through their studies, it has been found that within these molecular junctions the attenuation coefficient ( $\sim 2.5 \text{ nm}^{-1}$ ) is in good agreement with electrochemical studies of similar layers[108]. Furthermore, similar to studies involving SAMs, the resistance of the junction exponentially increases with layer thickness. Recently a thorough investigation of the current voltage characteristics of nitroazobenzene and azobenzene[13] displayed that junctions were

stable throughout billions of cycles and up to temperatures of 180°C. In addition, within this study electron transport was determined to be consistent with nonresonant tunneling through the molecular layer.

Although the majority of the work by McCreery and coworkers has been focused on ensemble junctions, recently molecular junctions have been investigated by surface-diffusion-mediated deposition[109, 110]. Within this, molecular junctions containing 1-10 molecules were formed as “cold” gold atoms diffused across the surface to make contact with the molecular layer. It was found that electron transport was connected to the off-set between the HOMO of the diazonium layer and Fermi level of the gold, suggesting that tunneling is hole-mediated[109, 110].

## 1.5 Objectives

Within the field of molecular electronics, studies have shown that cAFM is a powerful tool, bridging the gap between single molecule junctions and large ensemble junctions. Furthermore, both SAMs and diazonium derived molecular layers have displayed significant promise in the development of molecular devices. It is in this framework that the objectives of this thesis were designed. To further develop the understanding of electron transport through diazonium derived molecular junctions, Chapter 2 used cAFM to probe current voltage characteristics of nitroazobenzene layers on carbon to compare to the results obtained by McCreery and coworkers. To further extend the applicability of diazonium molecular layers, Chapter 3 focused on the control and understanding nitroazobenzene deposition on gold surfaces. Finally, in an effort to explore electron transport properties of new molecular junctions, Chapter 4 is geared towards cAFM studies of nitroazobenzene on template stripped gold, as well as the use of mixed-mode bonded layers within molecular junctions.

## References

- [1] Aviram, A.; Ratner, M. *Chemical Physics Letters* **1974**, *29*.
- [2] Xu, B.; Tao, N. J. *Science* **2003**, *301*, 1221–1223.
- [3] Dodabalapur, A. *Solid State Communications* **1997**, *102*, 259–267.
- [4] Park, H. J.; Xu, T.; Lee, J. Y.; Ledbetter, A.; Guo, L. J. *ACS nano* **2011**, *5*, 7055–60.
- [5] Lundstrom, M. *Science* **2003**, *299*, 210–211.
- [6] Kish, L. B. *Physics Letters A* **2002**, *305*, 144–149.
- [7] McCreery, R. L.; Bergren, A. J. *Advanced Materials* **2009**, *21*, 4303–4322.
- [8] Antone Gonsalves; *Intel Debuts 32-NM Westmere Desktop Processors*; 2010.  
<http://www.informationweek.com/news/security/management/222200708>.
- [9] McCreery, R. L. *Chemistry of Materials* **2004**, *16*, 4477–4496.
- [10] Ozawa, P. J. *Transaction on Parts, Materials and Packaging* **1969**, *5*.
- [11] Mujica, V.; Roitberg, A. E.; Ratner, M. *The Journal of Chemical Physics* **2000**, *112*, 6834.
- [12] Lu, Q.; Liu, K.; Zhang, H.; Du, Z.; Wang, X.; Wang, F. *ACS nano* **2009**, *3*, 3861–8.
- [13] Bergren, A.; McCreery, R.; Stoyanov, S.; Gusarov, S.; Kovalenko, A. *The Journal of Physical Chemistry C* **2010**, 15806–15815.
- [14] Wang, W.; Lee, T.; Reed, M. *Physical Review B* **2003**, *68*, 1–7.
- [15] Vilan, A. *Journal of Physical Chemistry C* **2007**, *111*, 4431–4444.
- [16] Engelkes, V. B.; Beebe, J. M.; Frisbie, C. D. *Journal of the American Chemical Society* **2004**, *126*, 14287–96.
- [17] Simmons, J. G. *Journal of Applied Physics* **1963**, *34*, 2581.
- [18] Simmons, J. G. *Journal of Applied Physics* **1963**, *34*, 1793.
- [19] Simmons, J. G. *Journal of Applied Physics* **1963**, *34*, 238.

- [20] Xing, Y.; Park, T.-H.; Venkatramani, R.; Keinan, S.; Beratan, D. N.; Therien, M. J.; Borguet, E. *Journal of the American Chemical Society* **2010**, *132*, 7946–56.
- [21] Wold, D. J.; Frisbie, C. D. *Journal of the American Chemical Society* **2001**, *123*, 5549–56.
- [22] Anariba, F.; Steach, J. K.; McCreery, R. L. *The journal of physical chemistry. B* **2005**, *109*, 11163–72.
- [23] Tao, N. J. *Nature nanotechnology* **2006**, *1*, 173–81.
- [24] Luo, L.; Choi, S. H.; Frisbie, C. D. *Chemistry of Materials* **2011**, *23*, 631–645.
- [25] Choi, S. H.; Risko, C.; Delgado, M. C. R.; Kim, B.; Brédas, J.-L.; Frisbie, C. D. *Journal of the American Chemical Society* **2010**, *132*, 4358–68.
- [26] Mujica, V.; Ratner, M. A. *Chemical Physics* **2001**, *264*, 365–370.
- [27] Berlin, Y. A.; Hutchison, G. R.; Rempala, P.; Ratner, M. A.; Michl, J. **2003**, *107*, 3970–3980.
- [28] Yan, H.; Bergren, A. J.; McCreery, R. L. *Journal of the American Chemical Society* **2011**.
- [29] Wang, W.; Lee, T.; Reed, M. a. *Reports on Progress in Physics* **2005**, *68*, 523–544.
- [30] Binnig, G.; Rohrer, H.; Gerber, C.; Weibel, E. *Applied Physics Letters* **1982**, *40*, 178.
- [31] Binnig, G.; Rohrer, H. *Journal of Crystal Growth* **1983**, *65*, 679–680.
- [32] Marti, O.; Binnig, G.; Rohrer, H. *Surface Science* **1987**, *181*, 230–234.
- [33] Binnig, G.; Gerber, C.; Stoll, E.; Albrecht, T.; Quate, C. *Surface Science* **1987**, *190*, 1–6.
- [34] Akkerman, H. B.; Boer, B. D. *Journal of Physics: Condensed Matter* **2008**, *20*.
- [35] Andres, R.; Bein, T.; Dorogi, M.; Feng, S.; Henderson, J.; Kubiak, C.; Mahoney, W.; Osifchin, R.; Reifenberger, R. *Science (New York, N.Y.)* **1996**, *272*, 1323–5.
- [36] Donhauser, Z. J.; Mantooth, B. A.; Kelly, K. F.; Bumm, L. A.; Monnell, J. D.; Stapleton, J. J.; Price, D.; Rawlett, A. M.; Allara, D. L.; Tour, J. M.; Weiss, P. S. *Science* **2001**, *292*, 2303–2307.

- [37] Howell, S.; Kuila, D.; Kasibhatla, B.; Kubiak, C. *Langmuir* **2002**, *18*, 5120–5125.
- [38] Datta, S.; Tian, W.; Hong, S.; Reifenberger, R. *Physical review letters* **1997**, *79*, 2530.
- [39] Kergueris, C.; Bourgoïn, J.; Palacin, S. *Physical Review B* **1999**, *59*, 505–513.
- [40] Nozaki, D.; Cuniberti, G. *Nano Research* **2009**, *2*, 648–659.
- [41] Cai, L.; Skulason, H.; Kushmerick, J.; Pollack, S.; Naciri, J.; Shashidhar, R.; Allara, D.; Mallouk, T.; Mayer, T. *The Journal of Physical Chemistry B* **2004**, *108*, 2827–2832.
- [42] Fan, F.-R. F.; Lai, R. Y.; Cornil, J.; Karzazi, Y.; Brédas, J.-L.; Cai, L.; Cheng, L.; Yao, Y.; Price, D. W.; Dirk, S. M.; Tour, J. M.; Bard, A. J. *Journal of the American Chemical Society* **2004**, *126*, 2568–73.
- [43] Cygan, M. T.; Dunbar, T. D.; Arnold, J. J.; Bumm, L. A.; Shedlock, N. F.; Burgin, T. P.; Ii, L. J.; Allara, D. L.; Tour, J. M.; Weiss, P. S. *Journal of the American Chemical Society* **1998**, *7863*, 2721–2732.
- [44] Hallbäck, A.-S.; Poelsema, B.; Zandvliet, H. J. W. *Chemphyschem : a European journal of chemical physics and physical chemistry* **2007**, *8*, 661–5.
- [45] Wakamatsu, S.; Akiba, U.; Fujihira, M. *Colloids and Surfaces* **2002**, *200*, 785–790.
- [46] Wassel, R. A.; Fuierer, R. R.; Kim, N.; Gorman, C. B.; Carolina, N. *Nano* **2003**, *3*, 1617–1620.
- [47] Bumm, L. a.; Arnold, J. J.; Dunbar, T. D.; Allara, D. L.; Weiss, P. S. *The Journal of Physical Chemistry B* **1999**, *103*, 8122–8127.
- [48] Nitzan, A.; Ratner, M. *Science* **2003**, *300*, 1384–1389.
- [49] Ulgut, B.; Abruña, H. D. *Chemical reviews* **2008**, *108*, 2721–36.
- [50] Reed, M. A.; Zhou, C.; Muller, C. J.; Burgin, T. P.; Tour, J. M. *Science* **1997**, *278*, 252–254.
- [51] Li, X.; He, J.; Hihath, J.; Xu, B.; Lindsay, S. M.; Tao, N. *Journal of the American Chemical Society* **2006**, *128*, 2135–41.

- [52] Mahmoud, A. M.; Bergren, A. J.; Pekas, N.; McCreery, R. L. *Advanced Functional Materials* **2011**, *21*, 2273–2281.
- [53] Van Hal, P. a.; Smits, E. C. P.; Geuns, T. C. T.; Akkerman, H. B.; De Brito, B. C.; Perissinotto, S.; Lanzani, G.; Kronemeijer, A. J.; Geskin, V.; Cornil, J.; Blom, P. W. M.; De Boer, B.; De Leeuw, D. M. *Nature nanotechnology* **2008**, *3*, 749–54.
- [54] Weiss, E. a.; Chiechi, R. C.; Kaufman, G. K.; Kriebel, J. K.; Li, Z.; Duati, M.; Rampi, M. a.; Whitesides, G. M. *Journal of the American Chemical Society* **2007**, *129*, 4336–49.
- [55] Anariba, F.; McCreery, R. L. *The Journal of Physical Chemistry B* **2002**, *106*, 10355–10362.
- [56] Ranganathan, S.; Steidel, I.; Anariba, F.; McCreery, R. L. *Nano Letters* **2001**, *1*, 491–494.
- [57] Solak, A. O.; Ranganathan, S.; Itoh, T.; McCreery, R. L. *Electrochemical and Solid-State Letters* **2002**, *5*, E43.
- [58] Rampi, M. a.; Schueller, O. J. a.; Whitesides, G. M. *Applied Physics Letters* **1998**, *72*, 1781.
- [59] Wang, B.; Luo, J.; Wang, X.; Wang, H.; Hou, J. G. *Langmuir : the ACS journal of surfaces and colloids* **2004**, *20*, 5007–12.
- [60] York, R. L.; Slowinski, K. *Journal of Electroanalytical Chemistry* **2003**, *551*, 327–336.
- [61] York, R. L.; Nguyen, P. T.; Slowinski, K. *Journal of the American Chemical Society* **2003**, 5948–5953.
- [62] Slowinski, K.; Chamberlain, R. V.; Miller, C. J. *Journal of the American Chemical Society* **1997**, *119*, 11910–11919.
- [63] Vericat, C.; Vela, M. E.; Benitez, G.; Carro, P.; Salvarezza, R. C. *Chemical Society reviews* **2010**, *39*, 1805–34.
- [64] Kind, M.; Wöll, C. *Progress in Surface Science* **2009**, *84*, 230–278.
- [65] Akkerman, H. B.; Blom, P. W. M.; de Leeuw, D. M.; de Boer, B. *Nature* **2006**, *441*, 69–72.

- [66] Ru, J.; Szeto, B.; Bonifas, A.; McCreery, R. L. *ACS applied materials & interfaces* **2010**, *2*, 3693–701.
- [67] Anariba, F.; Steach, J. K.; McCreery, R. L. *The journal of physical chemistry. B* **2005**, *109*, 11163–72.
- [68] Moreno Flores, S.; Toca-Herrera, J. L. *Nanoscale* **2009**, *1*, 40–9.
- [69] Tseng, A. a. *Nano Today* **2011**.
- [70] Müller, D. J.; Dufrière, Y. F. *Nature nanotechnology* **2008**, *3*, 261–9.
- [71] Kumaki, J.; Sakurai, S.-I.; Yashima, E. *Chemical Society reviews* **2009**, *38*, 737–46.
- [72] Wang, W.; Dong, R.; Yan, X.; Yang, B. *Journal of Physics D: Applied Physics* **2011**, *44*, 475102.
- [73] Engelkes, V. B.; Beebe, J. M.; Frisbie, C. D. *The journal of physical chemistry. B* **2005**, *109*, 16801–10.
- [74] Mativetsky, J. M.; Pace, G.; Elbing, M.; Rampi, M. A.; Mayor, M.; Samorì, P. *Journal of the American Chemical Society* **2008**, *130*, 9192–3.
- [75] Nijhuis, C. a.; Reus, W. F.; Whitesides, G. M. *Journal of the American Chemical Society* **2009**, *131*, 17814–27.
- [76] Skulason, H.; Frisbie, C. D. *Langmuir* **2000**, *16*, 6294–6297.
- [77] Mativetsky, J.; Palma, M.; Samorì, P. *STM and AFM Studies on (Bio) molecular Systems: Unravelling the Nanoworld* **2008**, 157–202.
- [78] Nuzzo, R.; Allara, D. *Journal of the American Chemical Society* **1983**, *105*, 4481–4483.
- [79] Love, J. C.; Estroff, L. a.; Kriebel, J. K.; Nuzzo, R. G.; Whitesides, G. M. *Self-assembled monolayers of thiolates on metals as a form of nanotechnology.*, 2005; Vol. 105.
- [80] Nijhuis, C. a.; Reus, W. F.; Barber, J. R.; Dickey, M. D.; Whitesides, G. M. *Nano letters* **2010**, *10*, 3611–9.

- [81] Wang, W. *Physica E: Low-dimensional Systems and Nanostructures* **2003**, *19*, 117–125.
- [82] Song, H.; Lee, H.; Lee, T. *Ultramicroscopy* **2008**, *108*, 1196–9.
- [83] Song, H.; Lee, C.; Kang, Y.; Lee, T. *Colloids and Surfaces A: Physicochemical and Engineering Aspects* **2006**, *284-285*, 583–588.
- [84] Wold, D.; Frisbie, C. *Journal of the American Chemical Society* **2000**, *122*, 2970–2971.
- [85] Beebe, J. M.; Engelkes, V. B.; Miller, L. L.; Frisbie, C. D. *Journal of the American Chemical Society* **2002**, *124*, 11268–9.
- [86] Beebe, J. M.; Engelkes, V. B.; Liu, J.; Gooding, J. J.; Eggers, P. K.; Jun, Y.; Zhu, X.; Paddon-Row, M. N.; Frisbie, C. D. *The journal of physical chemistry. B* **2005**, *109*, 5207–15.
- [87] Engelkes, V. B.; Frisbie, C. D. *The journal of physical chemistry. B* **2006**, *110*, 10011–20.
- [88] Beebe, J. M.; Kim, B.; Frisbie, C. D.; Kushmerick, J. G. *Journal of the American Chemical Society Nano* **2008**, *2*, 827–832.
- [89] Ho Choi, S.; Kim, B.; Frisbie, C. D. *Science (New York, N.Y.)* **2008**, *320*, 1482–6.
- [90] Ceccato, M.; Bousquet, A.; Hinge, M.; Pedersen, S.; Daasbjerg, K. *Chemistry of Materials* **2011**, 110218074748045.
- [91] Laurentius, L.; Stoyanov, S. R.; Gusarov, S.; Kovalenko, A.; Du, R.; Lopinski, G. P.; McDermott, M. T. *ACS nano* **2011**, *5*, 4219–27.
- [92] McCreery, R. L.; Wu, J.; Kalakodimi, R. P. *Physical chemistry chemical physics : PCCP* **2006**, *8*, 2572–90.
- [93] Leroux, Y. R.; Hui, F.; Noël, J.-M.; Roux, C.; Downard, A. J.; Hapiot, P. *Langmuir : the ACS journal of surfaces and colloids* **2011**, *27*, 11222–8.
- [94] Shewchuk, D. M.; McDermott, M. T. *Langmuir : the ACS journal of surfaces and colloids* **2009**, *25*, 4556–63.
- [95] Delamar, M.; Hitmi, R.; Pinson, J.; Saveant, J. *Journal of the American Chemical Society* **1992**, *114*, 5883–5884.

- [96] Pinson, J.; Podvorica, F. *Chemical Society reviews* **2005**, *34*, 429–39.
- [97] Zhang, X.; Wen, Y.; Li, Y.; Li, G.; Du, S.; Guo, H.; Yang, L.; Jiang, L.; Gao, H.; Song, Y. *Journal of Physical Chemistry C* **2008**, *112*, 8288–8293.
- [98] Paulik, M.; Brooksby, P.; a.D. Abell; a.J. Downard *Journal of Physical Chemistry C* **2007**, *111*, 7808–7815.
- [99] Picot, M.; Lapinsonnière, L.; Rothballer, M.; Barrière, F. *Biosensors & bioelectronics* **2011**, *28*, 181–8.
- [100] Polsky, R.; Harper, J. C.; Dirk, S. M.; Arango, D. C.; Wheeler, D. R.; Brozik, S. M. *Langmuir* **2007**, *23*, 364–6.
- [101] Harper, J. C.; Polsky, R.; Wheeler, D. R.; Dirk, S. M.; Brozik, S. M. *Langmuir : the ACS journal of surfaces and colloids* **2007**, *23*, 8285–7.
- [102] Anariba, F.; DuVall, S. H.; McCreery, R. L. *Analytical chemistry* **2003**, *75*, 3837–44.
- [103] McCreery, R.; Dieringer, J.; Solak, A. O.; Snyder, B.; Nowak, A. M.; McGovern, W. R.; DuVall, S. *Journal of the American Chemical Society* **2003**, *125*, 10748–58.
- [104] Kariuki, J. K.; McDermott, M. T. *Langmuir* **2001**, *17*, 5947–5951.
- [105] Jayasundara, D. R.; Cullen, R. J.; Soldi, L.; Colavita, P. E. *Langmuir* **2011**.
- [106] Hurley, B. L.; McCreery, R. L. *Journal of The Electrochemical Society* **2004**, *151*, B252.
- [107] Nowak, A. M.; McCreery, R. L. *Analytical chemistry* **2004**, *76*, 1089–97.
- [108] Yang, H.-H.; McCreery, R. L. *Analytical Chemistry* **1999**, *71*, 4081–4087.
- [109] Bonifas, A. P.; McCreery, R. L. *Nature nanotechnology* **2010**, *5*, 612–7.
- [110] Bonifas, A. P.; McCreery, R. L. *Nano letters* **2011**, *11*, 4725–9.

## 2 Probing Electron Transport Through Aryl Films on Carbon Surfaces with Conducting AFM

### 2.1 Introduction

Molecular electronics, both integrated with current technology and stand alone devices, have become a large and varied field of surface science. The pursuit towards smaller, flexible and dynamic systems has driven chemists and physicists to expand upon current silicon based devices. Within this, many advances have been made: development of organic light-emitting diodes, conducting polymers and organic dielectric layers[1]. These examples though; interesting and extensive, are generally composed of films that are vastly thicker than molecular dimensions [1]. It is from the goal to create molecular scaled devices, that molecular junctions are investigated. Defined as, thin ( $< 10$  nm) organic layers between two conducting or semi-conducting materials, molecular junctions have been investigated extensively [2, 3, 4, 5, 6, 7, 8, 9, 10, 11, 12]. Notably, of these systems, thiol self assembled monolayers (SAMs) on gold have been of great interest within molecular junctions due to their ordered structure, great functionality and ease of use [12, 13, 14, 15]. The sulfur-gold bond is much stronger than van der Waals forces seen in physisorbed species, but maintains a lability essential for re-ordering as surface density changes. However, within these systems there arises several structural instabilities which make them less than ideal for molecular junction development, Figure 2.1. It has been found that the molecular order on the surface is not complete and can include missing molecules (pinholes), liquid like states and kinked chains[16]. Functionalization of the SAM surface is required to avoid short circuits and molecular rearrangement during vapour deposition of metals [1, 17, 18]. Electron transfer

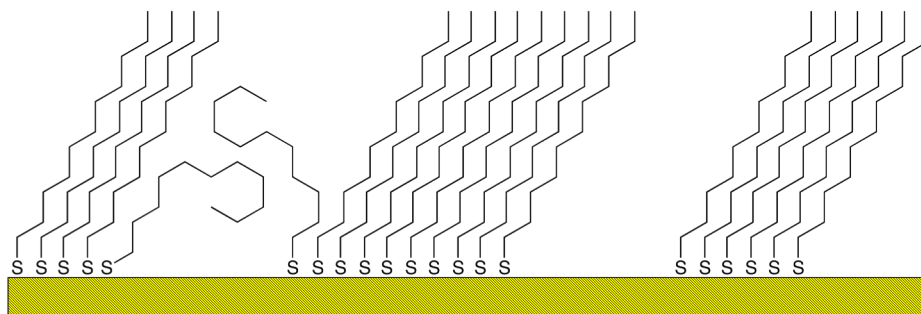


**Figure 2.1:** Schematic of dodecanethiol self-assembled monolayers on gold displaying kinked chains and pinhole defects.

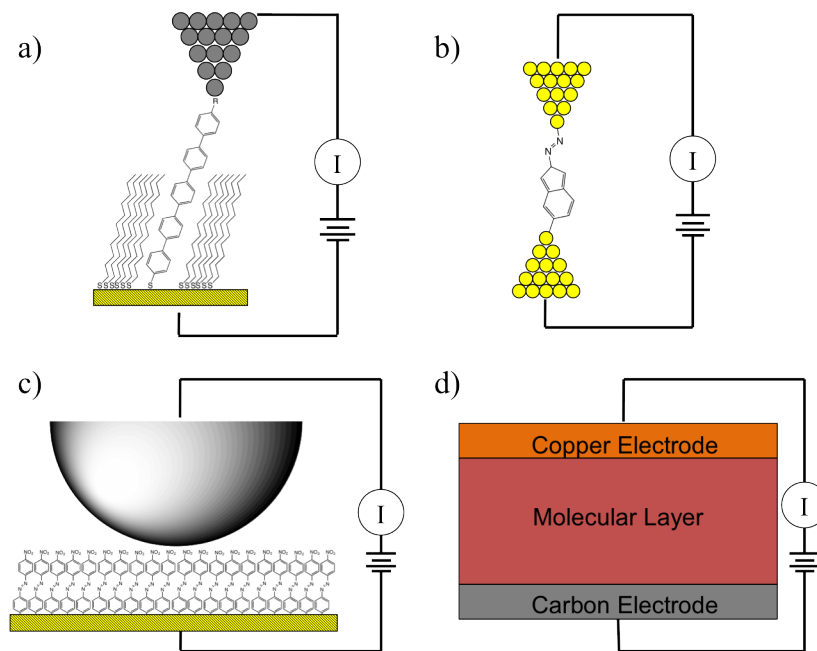


**Figure 2.2:** Schematics of various molecular junctions. a) scanning tunneling microscopy measurement of a molecular wire embedded in a mixed monolayer b) break junction c) conductive atomic force microscopy measurement of nitroazobenzene d) large area molecular junction.

within some SAM systems has also been shown to occur through defects as opposed to quantum mechanical tunneling[19]. Finally, the limited electrochemical and thermal stability of SAMs[20, 21] have made their compatibility with conventional electronics difficult due to operating potentials and temperatures ( $\sim 400\text{K}$ )[22].

It is from the limited properties of SAMs that the use of diazonium derived organic layers within molecular junctions is pursued. First reported by Pinson in 1992 [23], diazonium salts have been shown to spontaneously and electrochemically reduce to conductive surfaces (copper, gold, carbon, etc.) forming molecular layers[24, 25, 26, 7]. The bond resulting from the reduction of the diazonium to the electrode surface has been found to be covalent on carbon, copper and gold surfaces[27, 28, 23]. The strength of the covalent bond within diazonium layers leads to increased stability compared to that of SAMs under sonication, reflux, and thermal treatment[26, 25].

The pursuit to characterize electron transport through individual molecules (molecular wires) as well as massively paralleled systems ( $10^6$  molecules) has spurred the development of a wide variety of test platforms[29]. To measure transport through molecular wires, there are two routes of approach: design a probe to measure individual molecules, or isolate in-

dividual wires within molecular layers. Typically the latter is accomplished by scanning tunneling microscopy (STM) and mixed monolayers of SAMs where molecular wires extend above a background of alkanethiols, Figure 2.2a. However, there exists non-trivial effects from: the surrounding alkanthiol, tip-molecule interaction and the orientation of the molecular wire [1]. Break junctions, Figure 2.2b, on the other hand, seek to eliminate surrounding effects by measuring electron transport through individual molecules spanned between curved or atomically sharp electrodes. Measurements within these systems have shown to be difficult due to the resistivity across long molecules producing low signal-to-noise and contact geometry [29]. On the other end of the scale, systems involving thousands or millions of molecules do not suffer from low signal-to-noise or small changes in contact geometry as measurements made are an average of the entire system, Figure 2.2d. Typically these devices are constructed by vapour depositing metal on the surface of a molecular layer to act as the top electrode. These systems have been studied with a variety of molecules and electrode materials as well as have shown to be stable at high temperatures and over millions of measurements [7, 30, 25].

There exists a need to understand how electron transport scales between these different approaches. It is in this role that conductive atomic force microscopy (cAFM) is ideal, Figure 2.2c. Conductive atomic force microscopy uses a metallized probe to make electrical contact with the surface. Typically silicon tips are coated with 50 nm of metal (gold, copper, platinum) making the tip radius greater than those in STM and break junctions, involving contacts containing 10s - 100s of molecules[31, 32]. Furthermore, unique to atomic force microscopy (AFM), force can be applied (and measured) to investigate electron transport under various applied loads. Commercial cAFM systems are available and work well to image samples under low voltage and current. However, it has been found that many of these instruments are not capable of measuring (or applying) the voltages and currents necessary to fully investigate electron transport[33]. As a result, a conventional AFM system was modified to make use of an external potentiostat as described below.

McCreery *et al.* have extensively characterized micrometer sized diazonium derived molecular junctions between carbon and copper electrodes[30, 8, 6, 7]. The use of vapour deposition for top contact makes it difficult to generate junctions on the nanometer scale. Here cAFM will aid in the understanding of how electron transport in diazonium derived layer scales between macroscopic and microscopic junctions. It is from this, that the work presented in this chapter is tailored. Molecular layers of nitroazobenzene (NAB) were de-

posited on pyrolyzed photoresist films (PPF) via cyclic voltametry. Using cAFM, current voltage (IV) measurements were made on films of varying thickness and under applied loads. Contact area, penetration depth and film deformation were investigated to determine their effects on electron transport. Furthermore, transport properties such as dielectric constants, effective electron mass and transport barriers were studied by modeling IV curves with an adapted Simmons model.

## 2.2 Experimental

### 2.2.1 Substrate Preparation

Pyrolyzed photoresist films (PPF) for electron transport study were prepared by a fellow group member, Jane Cao, following the procedure demonstrated by Ranganathan *et al*[34]. Positive photoresist AZP4330-RS (Clariant Corp., NJ) was spin coated onto 1 cm<sup>2</sup> diced clean silicon wafers. Substrates were pyrolyzed using a tube furnace (Lindberg) fitted with a quartz tube under forming gas (95% N<sub>2</sub>, 5% H<sub>2</sub>) following the temperature program outlined by Ranganathan *et al.*. PPF substrates were allowed to cool over night and stored under house vacuum until surface modification.

### 2.2.2 Diazonium Salt Preparation and Surface Modification

Following a modified procedure of Starkey *et al.*[35], nitroazobenzene (NAB) diazonium salt was synthesized from 2.5 g of Disperse Orange 3 (Sigma-Aldrich) precursor. Disperse Orange 3 was partially dissolved in 30 mL of fluoboric acid (Fisher Chemicals) at 0°C under constant stirring. A chilled solution of 5 g of sodium nitrite (ACP Montreal) in 100 mL of deionized (18 MΩ) water was added drop-wise over 30 minutes until the reaction was complete. The product was then vacuum filtered using a glass frit and redissolved in cold HPLC grade acetonitrile (Fisher Chemicals). The NAB diazonium salt was recrystallized by slowly adding chilled ether (Fisher Chemicals) and allowing crystals to form at the solution surface. Following this, the product was vacuum filtered and the filtrate underwent further recrystallization. Once the yield of NAB diazonium salt was sufficient the product was allowed to dry and stored over desiccant at -20°C until needed.

Clean PPF substrates were thoroughly rinsed with deionized (18 MΩ) water, dried with Ar<sub>(g)</sub> and placed in a three electrode cell with 500 μM de-aerated NAB diazonium salt solution containing 0.1 M Bu<sub>4</sub>NBF<sub>4</sub> (Sigma-Aldrich). NAB was deposited electrochemi-

cally using a Pine Biopotentiostat model AFCPI controlled by Aftermath software (version 1.2.4532) by cycling the potential from 200 mV to -800 mV at various rates 10 mV/s, 50 mV/s, 100 mV/s and 200 mV/s against a Ag/AgNO<sub>3</sub> reference electrode and platinum mesh counter electrode.

### 2.2.3 Atomic Force Microscopy Imaging and Film Thickness Measurements

Atomic force microscopy (AFM) imaging and film thickness measurements were performed using a Nanoscope IIIa Multimode<sup>TM</sup> (Digital Instruments). Measurements were taken under ambient conditions using rectangular Si cantilevers with reflective Al coating (Olympus). The force constant and oscillating frequency of the probes were 40 N/m and  $300 \pm 10$  kHz respectively. Film thickness measurements were performed by “scratching” a  $1 \mu\text{m}^2$  area at high force in contact mode. The area was re-imaged, at  $5 \mu\text{m}^2$ , in tapping mode and the cross sectional profile was taken. Control “scratches” were performed on bare substrates to ensure forces were not sufficient to damage the substrate.

### 2.2.4 Conductive Atomic Force Microscopy

Electron transport measurements were performed using a Nanoscope IIIa Multimode<sup>TM</sup>, with an external Reference 600 potentiostat (Gamry Instruments). To conduct electron transport measurements using the Nanoscope IIIa Multimode<sup>TM</sup>, steps were required to make electrical contact to the sample and probe, as well as to ensure that both were isolated from the Multimode<sup>TM</sup>. Firstly, an acrylic sample holder with a copper clip was designed and manufactured to make electronic contact to the sample, Figure 2.3a. An Electrostatic Force Microscopy probe holder (Product #: MMEFCH) was purchased (Bruker) which isolated the tip from the housing of the Multimode, Figure 2.3c. With this, the brass clamp was loosened to allow a wire to make electronic contact to the probe. The AFM assembly was placed on an isolation table within a faraday cage to limit mechanical and electrical noise. Current voltage (IV) curves were taken in ambient conditions by cycling the potential from -2 V to 2 V against a reference within the Gamry potentiostat. Top electrical contact was made by bringing an ARROW-FMAU-50 (Nano World) gold coated (70 nm) silicon cantilever (2.8 N/m,  $75 \pm 10$  kHz) into contact at the desired force. Each curve consists of an average of 20 sweeps taken at 100 000 mV/s. IV curves were taken at three different locations on the substrate at various forces and the resultant median is displayed unless otherwise stated.

## 2.2.5 Scanning Electron Microscopy Tip Characterization

Conductive atomic force microscopy (cAFM) tips were imaged via scanning electron microscopy (SEM) using a Hitachi S4800 Field Emission SEM. Tips were imaged with a 10.0 kV accelerating voltage to determine tip radius and effective contact area.

## 2.3 Results and Discussion

### 2.3.1 Modification of Conventional AFM for cAFM Measurements

During a trip to the Frisbie lab at the University of Minnesota it was learnt that by using an external potentiostat it was possible to perform current voltage measurements using a Nanoscope IIIa Multimode<sup>TM</sup>. Furthermore, it was found that isolating the conductive tip from the AFM assembly required an insulating sample and tip holder. Employing the help

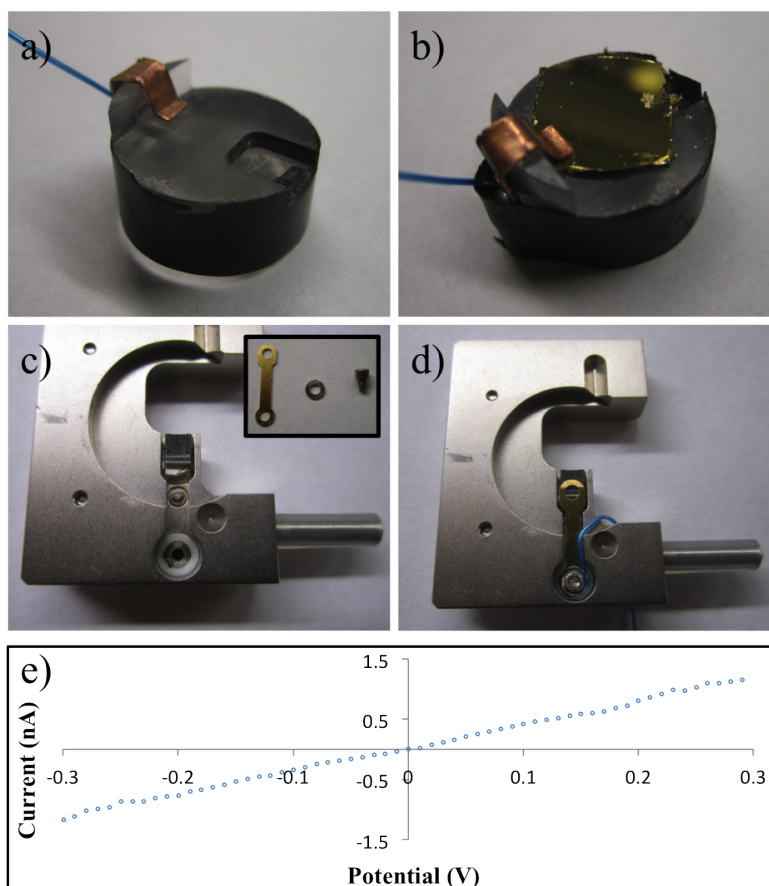


**Figure 2.3:** Components used for modified conductive atomic force microscopy assembly. a) insulating acrylic sample holder displaying copper clip and cut-outs b) placement of sample within holder c) disassembled cantilever holder d) cantilever holder and wire attachment e) IV curve of dodecanethiol on gold.

of the University of Alberta’s Department of Chemistry machine shop an acrylic sample holder was manufactured, Figure 2.3a. The sample holder design included cut-outs so that samples of varying thickness could be inserted without damaging the molecular layer of interest, Figure 2.3b. The cantilever holder purchased from Bruker, contained a teflon ring to isolate the conductive tip from the AFM housing, Figure 2.3c. Disassembling the cantilever clip allowed a wire to be inserted to make electrical contact to the tip, Figure 2.3d. The entire cAFM system was housed in a Faraday cage to reduce electrical noise. Current voltage measurements of dodecanethiol on gold, Figure 2.3e, were in good agreement with those measured by Frisbie *et al*[10]. From this it was determined that the modified cAFM assembly was working correctly and proceeded to investigate molecular junctions of NAB on PPF.

### 2.3.2 Topographic Characterization

Pyrolyzed photoresist film substrates were modified with a 500  $\mu\text{M}$  nitroazobenzene (NAB) diazonium salt solution containing 0.1 M  $\text{Bu}_4\text{NBF}_4$  electrolyte within a three electrode cell by cycling the potential from 200 mV to -800 mV at various sweep rates: 10 mV/s, 50 mV/s, 100 mV/s and 200 mV/s. Cyclic voltammograms (CV) obtained for each sample displayed a large cathodic reduction peak and chemically irreversible deposition similar to those described in literature[36, 37, 24]. The topography of the substrate and film is an important parameter for the formation of molecular junctions. Films with large topographic features make it difficult to determine the contact area of the cAFM probe. It is ideal to a uniform flat surface in which to measure electron transport. Figures 2.4a and 2.4b show 5  $\mu\text{m}^2$  and 1  $\mu\text{m}^2$  tapping mode height images (z-scale: 10 nm) of unmodified PPF substrates, respectively. Visually there are minimal surface features and the surface is extremely flat over both the 5  $\mu\text{m}^2$  and 1  $\mu\text{m}^2$  images. This is supported by calculated root mean squared (RMS) roughness of 0.35 nm over both areas which is in agreement with literature[34]. Figure 2.4c and 2.4e display surfaces modified by 500  $\mu\text{M}$  NAB diazonium salt deposited at 200 mV/s and 50 mV/s respectively. From this it is evident that the NAB has formed a uniform layer as minimal topography changes are apparent. Calculating the roughness of these surfaces over 5  $\mu\text{m}^2$  yielded values similar to bare PPF: 0.35 nm and 0.48 nm for 50 mV/s and 200 mV/s deposition respectively. By having low topographic roughness ( $< 0.5$  nm) within the NAB films, the understanding of contact area between the tip and surface is greatly simplified.

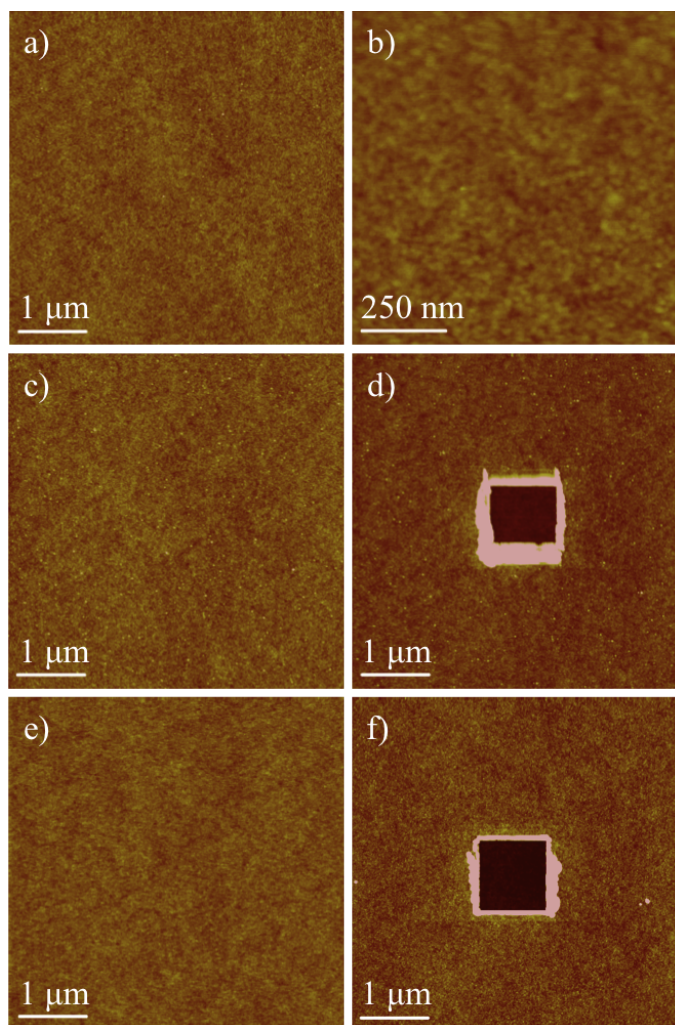


**Figure 2.4:** AFM tapping mode height images of a)  $5 \mu\text{m}^2$  bare PPF, b)  $1 \mu\text{m}^2$  bare PPF, c)  $5 \mu\text{m}^2$  NAB deposited at 200 mV/s, d) scratched image of c), e)  $5 \mu\text{m}^2$  NAB deposited at 50 mV/s, f) scratched image of e). Z-scale in all images is 10 nm.

Film thicknesses were determined by scratching a  $1 \mu\text{m}^2$  area and re-imaging over a  $5 \mu\text{m}^2$  area. Control measurements were performed to ensure forces used to remove the layer were not enough to damage the underlying PPF substrate (not shown). Figures 2.4d and 2.4f show typical scratched images for 200 mV/s and 50 mV/s. Taking the cross sectional average over the scratched and intact film yields NAB films of: 2.5 nm, 4.1 nm, 4.5 nm and 6.1 nm for layers deposited at: 200 mV/s, 100 mV/s, 50 mV/s and 10 mV/s respectively.

### 2.3.3 Effects Governing Electron Transport Through NAB Layers

Conductive atomic force microscopy (cAFM) was used to investigate electron transport through molecular layers of NAB on PPF. Current voltage (IV) measurements were taken

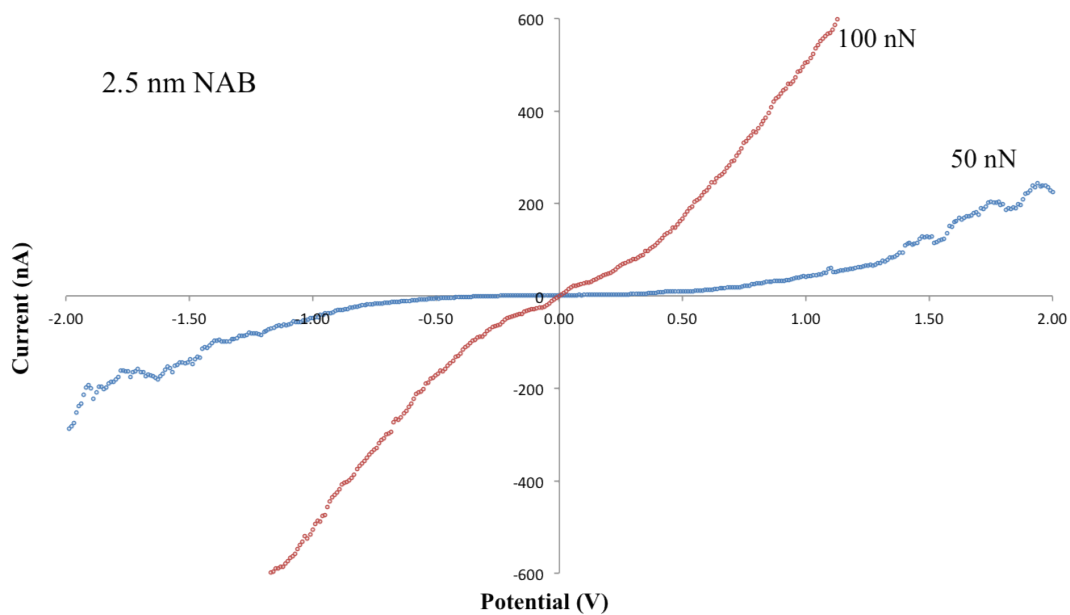


**Figure 2.5:** Current voltage measurement of a 2.5 nm NAB film on PPF at 50 nN and 100 nN applied force.

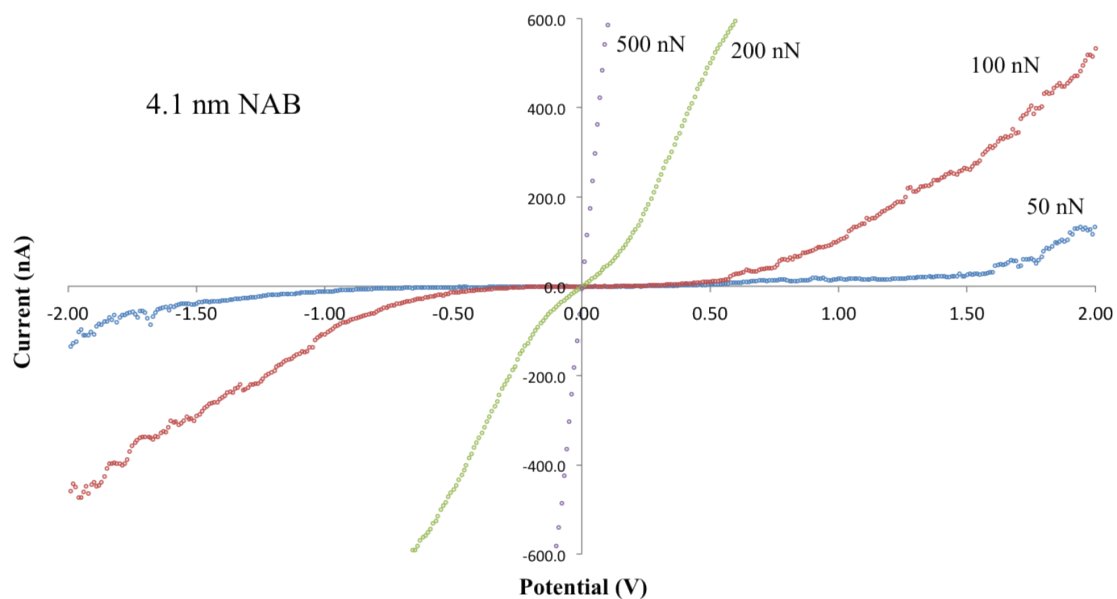


**Figure 2.6:** Current voltage measurement of a 4.1 nm NAB film on PPF at various applied forces.

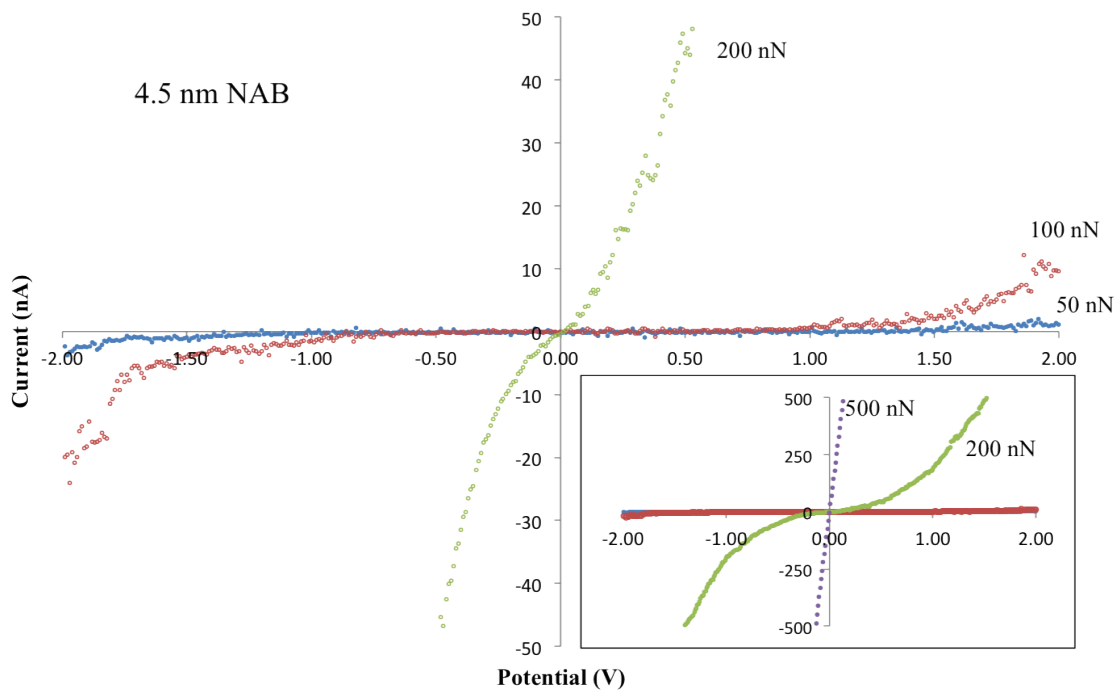


**Figure 2.7:** Current voltage measurement of a 4.5 nm NAB on PPF under various applied forces. Note the reduced scale for clarity. Inset full scale IV measurement displaying behaviour at higher forces.

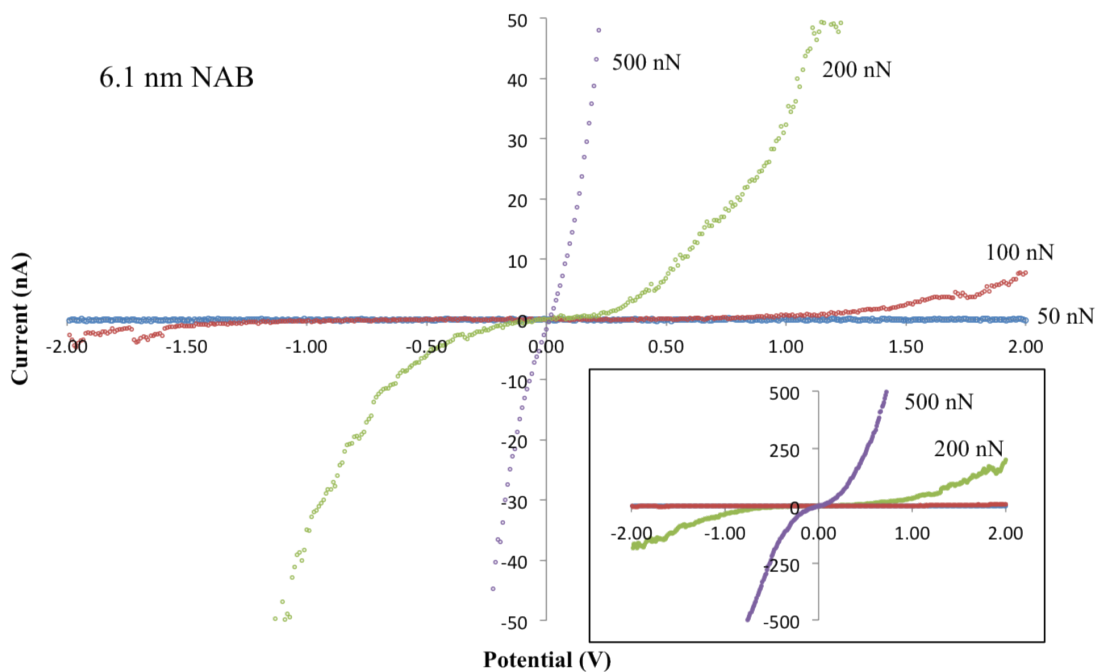


**Figure 2.8:** Current voltage measurement of a 6.1 nm NAB on PPF under various applied forces. Note the reduced scale for clarity. Inset full scale IV measurement displaying behaviour at higher forces.

in air under ambient conditions for various film thicknesses and under several applied forces (loads): 50 nN, 100 nN, 200 nN and 500 nN. Measurements were taken by cycling the voltage 20 times from -2 V to 2 V at 100 000 mV/s at three locations on each sample. Unless otherwise stated the curves below are an average of 20 cycles. [Note a representative un-averaged current voltage curve is show in Appendix 6.2] Figure 2.5 shows IV measurements of a 2.5 nm NAB film on PPF at forces of 50 nN and 100 nN. Considering the 50 nN curve, it is visible that the IV behaviour is linear over low potentials ( $\pm 0.25$  V) and deviates non-ohmically (non linear) at higher potentials. Similar behaviour is seen in the 100 nN curve, however deviation occurs at much lower potential. In both cases the low voltage linear behaviour and deviation to non linear IV response suggests electron tunneling through the molecular layer[1]. Further, it is clear that under higher loads, the magnitude of tunneling current increases. At this point it is unclear what the direct cause of this effect is, but can be considered to be a result of; deformation of the molecular layer, increased contact area between the tip and the film, and/or reduced tunneling distance as the tip penetrates the NAB layer. As a result, the determination of current densities ( $\text{A}/\text{cm}^2$ ) are not straightforward, as the tip/surface interface under different loads is not yet fully understood. As a result, Figure 2.5 and all subsequent IV figures are plotted with measured currents and not current densities.

Similar IV behaviour is seen in Figures 2.6 - 2.8 where thicker (4.1 nm, 4.5 nm, 6.1 nm) NAB films were measured. Note the scale ( $\pm 50$  nA) for Figures 2.7 and 2.8 was chosen for clarity of lower applied forces. The inset in each figure displays the full current scale of each measurement. It is clear that for each film thickness higher applied forces yield more current at a given voltage. In an effort to de-convolute the effects of: film deformation, contact area and reduced tunneling distance each parameter was considered independently. Firstly, it is considered that film deformation would cause a structural change in the molecular layer that would alter electron transport. Furthermore, it is assumed that under constant force, contact area will not change and the resultant structural change would be the same over all film thicknesses.

This was investigated by considering the 100 nN and 200 nN curves at each film thickness, Figures 2.9 and 2.10. To understand the effect of structural change on IV behaviour a simple model for quantum mechanical tunneling current is considered

$$I = I_0 e^{-\beta d} \quad (2.1)$$

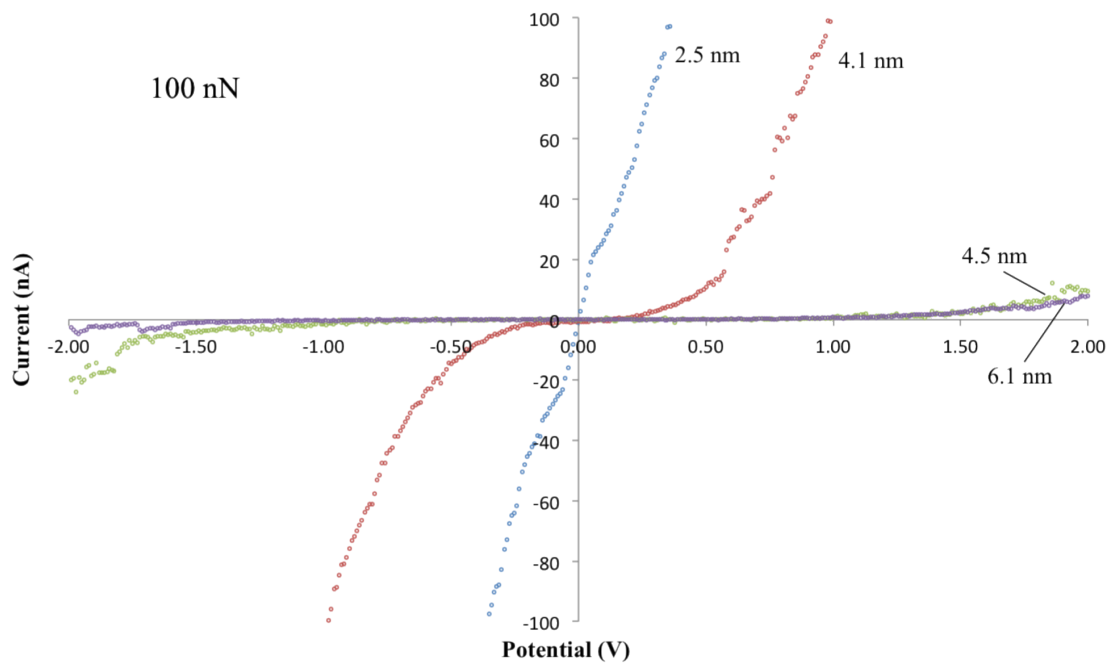


**Figure 2.9:** Current voltage measurement at constant applied force (100 nN) for various film thicknesses.

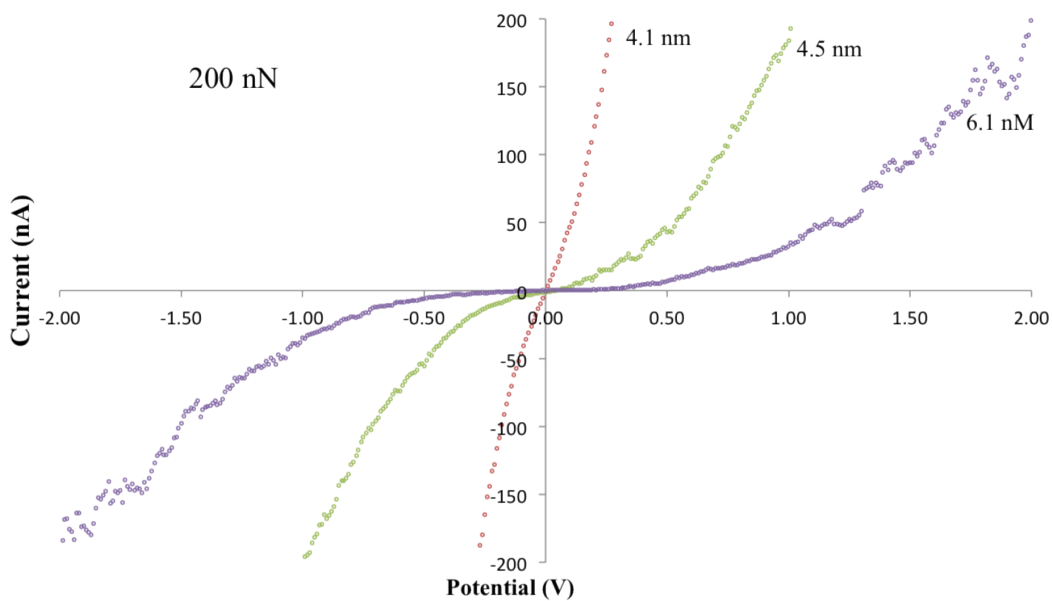


**Figure 2.10:** Current voltage measurement at constant applied force (200 nN) for various film thicknesses.

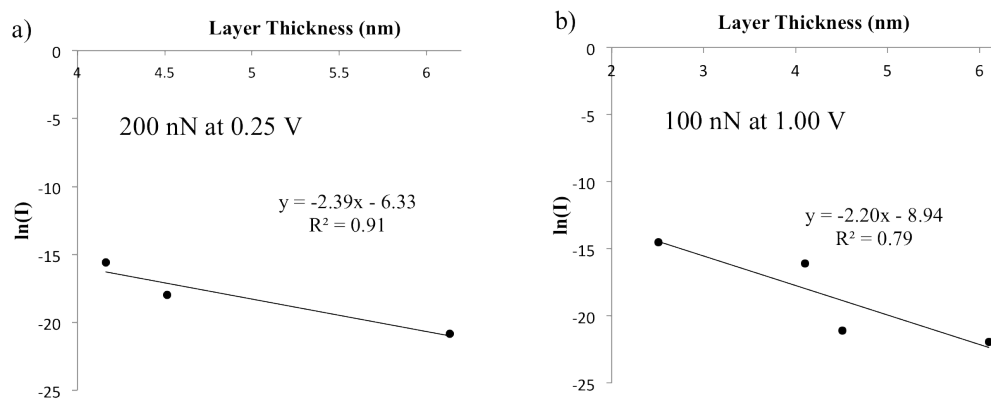


**Figure 2.11:**  $\ln(I)$  against layer thickness at 200 nN and 100 nN. Determination of attenuation coefficient,  $\beta$ .

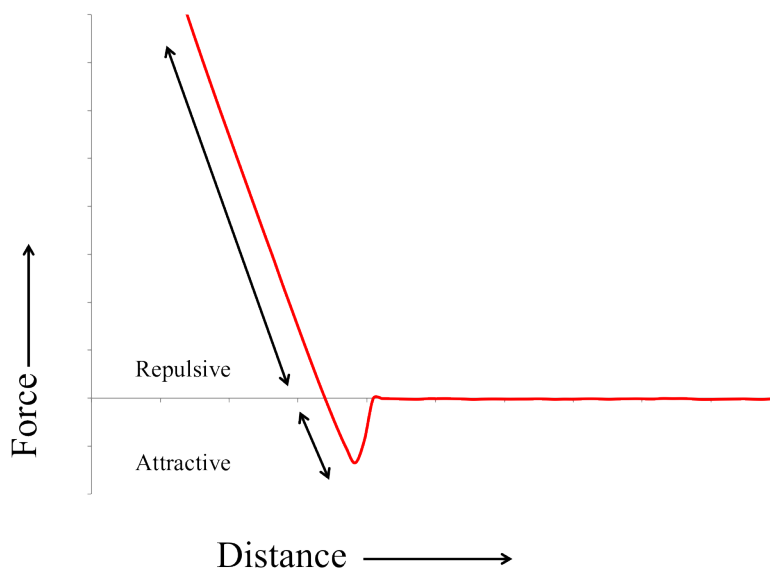


**Figure 2.12:** Typical force/distance curve for withdraw of AFM tip from the surface.

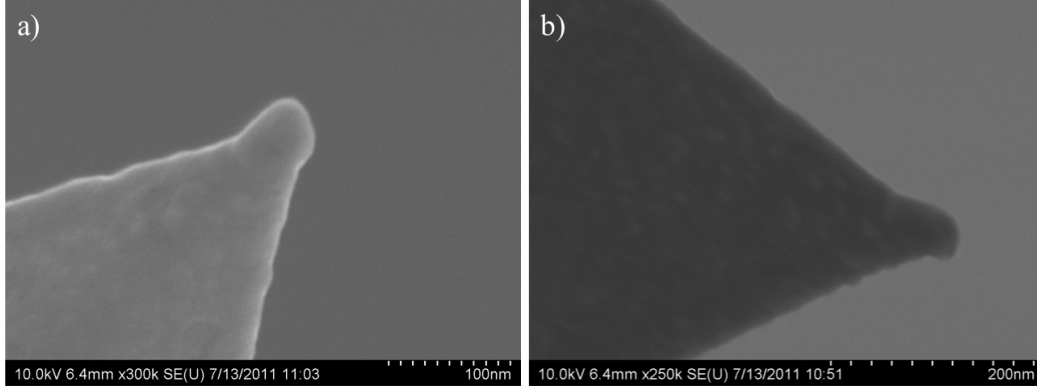


**Figure 2.13:** 10.0 kV high resolution SEM images of unused cAFM tips, a) along cantilever axis, b) rotated approximately  $90^\circ$ .

where current,  $I$ , is proportional to  $I_o$ , the current at zero layer thickness (inversely, the contact resistance) and exponentially dependent on the layer thickness,  $d$ , and the attenuation coefficient,  $\beta$ . The attenuation coefficient, is rooted in the electron tunneling mechanism and the chemical structure of the barrier. Structural changes of the NAB layer under different applied loads would be evident in  $\beta$ . Figure 2.11 shows  $\ln(I)$  plotted against film thickness for 200 nN at 0.25 V and 100 nN at 1.00 V. Note that the voltages chosen were the minimum values in which non negligible currents were measured. At first approximation it appears that the  $\beta$  values under each force are different, implying structural change within the layer. However, McCreery *et al.* [8], displayed reduction of the attenuation coefficient by measuring current at higher potentials. As a result, it can be considered that the values obtained for 100 nN and 200 nN are equivalent. Furthermore, from this and previous work investigating biphenyl and nitrobiphenyl diazonium salts on carbon surfaces [38, 39], the measured  $\beta$  ( $2.4 \text{ nm}^{-1}$ ) agrees with accepted values. It is apparent from this that the attenuation coefficient, and thus the electron tunneling mechanism, does not change under applied forces of 100 nN and 200 nN.

In order to investigate contact area and its effect on tunneling current, two contact models were considered: Johnson, Kendal and Roberts theory (JKR)[40] and thin-coating contact mechanics (TCCM)[41]. The applicability of these two theories depend on the forces governing tip and sample interaction. Fundamentally within any AFM experiment there are two force regimes that shape the deflection of the cantilever: attractive and repulsive, Figure 2.12. For attractive forces, where JKR theory applies, surface energies, work of adhesion and the surrounding medium play a significant role in maintaining contact. In contrast, TCCM

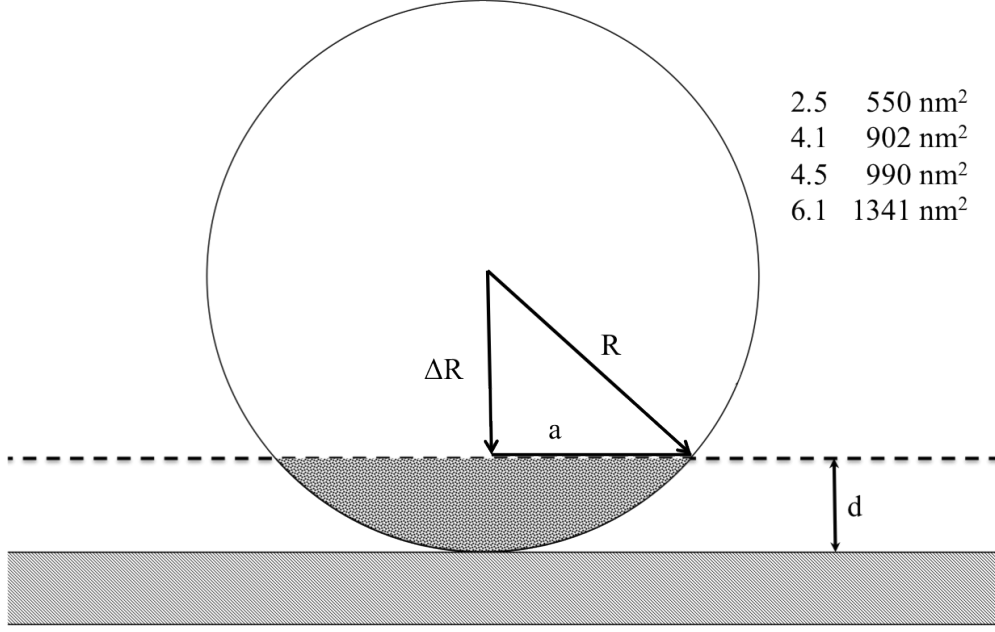


**Figure 2.14:** Schematic of contact area calculation under the approximation of a spherical cap. Maximum possible contact area for each film thickness upper right.

theory and the repulsive regime depend on the Young's modulus and the force applied to the surface. To determine which model applies to the IV measurements above, the force of attraction was measured by performing force curve analysis on NAB layers using fresh cAFM tips. It was found that the attractive force required to maintain contact ( $20 \pm 3$  nN) was much less than the minimum force applied to the surface (50 nN). As a result it was concluded that all measurements were performed under repulsive forces and thus TCCM theory was used to determine the contact area.

Briefly, TCCM theory is based on Hertz - like adhesion-less contact mechanics. It can be shown that the effective contact radius,  $a$  can determined by

$$a = \sqrt{Rd} \left( \frac{4\bar{F}}{\pi} \right)^{1/4} \quad (2.2)$$

Where  $R$  is the radius of the tip,  $d$  is film thickness and  $\bar{F}$  is the effective force applied to the layer as determined by

$$\bar{F} = \left( \frac{F}{E_u R d} \right) \quad (2.3)$$

Given  $F$  is the force applied to the layer,  $E_u$  is the uniaxial strain modulus as determined by the Young's modulus,  $E$ , and the Poisson ratio,  $\nu$ ,

**Table 2.1:** Calculated contact area,  $A$ , and layer penetration,  $\Delta d$ , for various NAB film thicknesses and applied forces.

Force (nN)	50		100		200		500		MAX
Film Thickness (nm)	A (nm <sup>2</sup> )	$\Delta d$ (nm)	A (nm <sup>2</sup> )	$\Delta d$ (nm)	A (nm <sup>2</sup> )	$\Delta d$ (nm)	A (nm <sup>2</sup> )	$\Delta d$ (nm)	A (nm <sup>2</sup> )
2.5	61	0.28	86	0.39					550
4.1	78	0.35	110	0.50	157	0.71	249	1.13	902
4.5	82	0.37	116	0.53	164	0.75	261	1.19	990
6.1	95	0.43	135	0.61	192	0.87	305	1.39	1341

$$E_u = \frac{(1 - \nu)E}{(1 + \nu)(1 - 2\nu)} \quad (2.4)$$

The Poisson ratio, a measure of a material's deformation under strain, was approximated as 0.4, along with a Young's modulus of  $E = 7 \text{ GPa}$  from measurements of aromatic thiols on gold[42]. cAFM tip radius,  $R$ , was determined via scanning electron microscopy (SEM). Figures 2.13(a) and (b) show high resolution SEM images of an unused cAFM tip along the cantilever axis and rotated at approximately  $90^\circ$ . The radius was determined to be  $35 \pm 7 \text{ nm}$  by approximating the tip to a sphere and determining maximum and minimum circles that represent the shape of the tip[31]. Using equations 2.2 - 2.4 the contact radius,  $a$ , was calculated and extended to contact area,  $A$ , by considering the area of a spherical cap, Figure 2.14. In addition, with the calculation of  $a$ , the distance the tip penetrated the layer,  $\Delta d$ , was determined, along with the maximum possible contact area. Table 2.1 shows the calculated contact areas and penetration depths for each film. Intuitively, higher forces increase the contact area along with penetration depth. It can be further seen, that under the TCCM model the effect of force,  $\bar{F}$ , is reduced with increasing film thickness, however the effective contact area is dominated by the  $\sqrt{Rd}$  term in equation 2.2. This leads to increased contact area and penetration depth for larger film thicknesses. As a result, it is clear that both contact area and reduced tunneling distance, resulting from  $\Delta d$ , are playing a role in determining IV behaviour.

To further separate the effect of contact area and tunneling distance, the work by Ru *et al*[30] was considered. From their investigation of molecular layers of NAB it was found that increasing the contact area by 5 times, increased tunneling current linearly by an order of magnitude. With this, and the results in Table 2.1, it is approximated that changes in

IV behaviour of one order of magnitude are attributed to differences in contact area. This however, is somewhat counter intuitive upon considering the exponential dependence on tunneling distance in equation 2.1 and that only two orders of magnitude are seen in cAFM IV curves. This is further investigated below.

### 2.3.4 Molecular Layer Electron Transport Properties

Electron transport through molecular layers can be considered to be fundamentally different from other systems in that tunneling occurs through molecular bonds as opposed to tunneling through space. Under this assumption, the bond structure of the layer plays a significant role in electron transport. It is well known that within molecular systems there exists a highest occupied molecular orbital (HOMO) and a lowest unoccupied molecular orbital (LUMO). Within molecular electronics it is believed that electrons and holes, are transported through the LUMO and HOMO respectively, and that the barrier to transport is influenced by the energies of these levels[8]. It was discussed earlier that the attenuation coefficient,  $\beta$ , is dependent on the structure of the molecular layer and was found to be constant over varying film thickness. This suggests that as the molecular layer grows the physical structure does not change, in that bonding occurs in the same fashion throughout the layer. As a result the changes in IV behaviour, though dependent on contact area and tunneling distance, can be investigated by considering other factors such as: the dielectric constant  $\varepsilon$ , the electron transport barrier,  $\phi_o$ , and the electron mobility or effective electron mass,  $m_e$ .

To understand how these variables change under various forces and film thicknesses, IV measurements were fitted (least-squares) with an adapted Simmons model. [Full model shown in Appendix 6.1] Fits were initiated by using values of similar systems from McCreery *et al*[8] over a potential of -0.5 V to 0.5 V. Figure 2.15a shows  $\ln |I|$  as function of potential for film thicknesses of 4.1 nm, 4.5 nm and 6.1 nm at a force of 200 nN, along with their corresponding fits (solid line). Similarly, Figure 2.15b displays  $\ln |I|$  measurements ranging from 100nN - 500 nN measurements for a constant film thickness of 4.1 nm. Table 2.2 shows that the dielectric constant increases with film thickness and both effective electron mass and barrier height are reduced agreeing with the trends seen in larger molecular junctions by McCreery *et al*[8]. Furthermore, values of effective electron masses as determined by the Simmons model are similar to those found in similar conjugated molecular systems ( $m_e = 0.16$ ) [43]. Upon considering the results in Table 2.2 it is not intuitive why the barrier

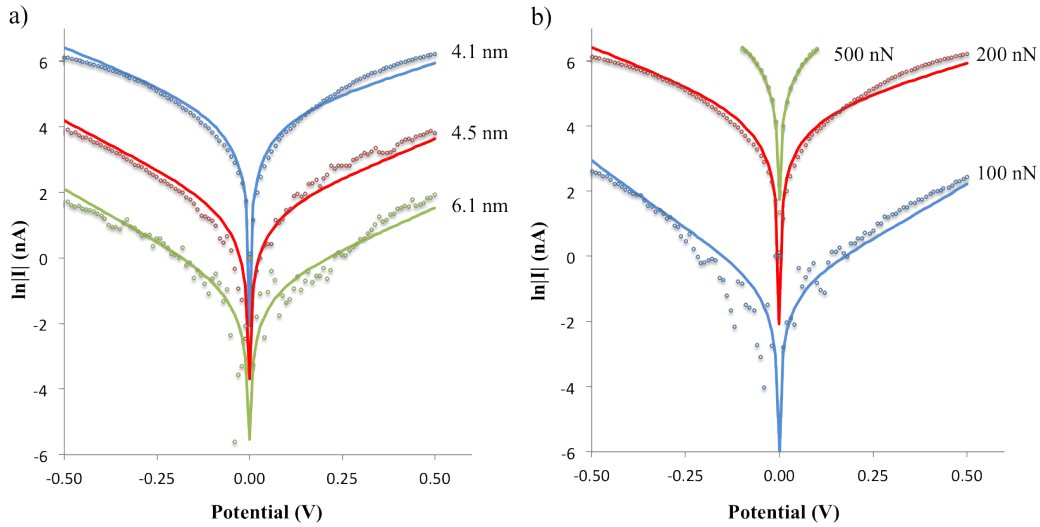


**Figure 2.15:**  $\ln(I)$  voltage measurements (open circles) of NAB films with Simmons model fit (solid line) a) constant force (200 nN) and b) constant film thickness (4.1 nm).

**Table 2.2:** Values for dielectric constant,  $\epsilon$ , effective electron mass,  $m_e$ , and electron transport barrier,  $\phi_o$ , of NAB films at constant force (200 nN) as determined by the Simmons model.

Film thickness (nm)	$\epsilon$	$m_e$	$\phi_o$ (eV)
4.1	9.00	0.14	1.23
4.5	10.60	0.18	1.08
6.1	20.00	0.11	1.02

**Table 2.3:** Values for dielectric constant,  $\epsilon$ , effective electron mass,  $m_e$ , and electron transport barrier,  $\phi_o$ , for 4.1 nm NAB film as determined by the Simmons model. Corrected effective electron mass in parenthesis.

Force (nN)	$\epsilon$	$m_e$	$\phi_o$ (eV)
100	10.00	0.34 (0.46)	0.91
200	9.00	0.14 (0.21)	1.23
500	10.03	0.10 (0.63)	1.14

height is reduced at higher film thicknesses. This however, can be explained by considering the energies of the frontier orbitals (HOMO and LUMO) as the molecular layer increases. McCreery *et al* found that as the layer grows electrons become more delocalized over the junction and HOMO and LUMO energies approach the Fermi level (work function) of the electrodes. As a result the barrier for electron (and hole) transport is reduced as the film thickness increases. Furthermore, the delocalization of electrons within the layer yield an increase in electron mobility (reduced electron mass) seen in thicker layers. Upon considering Table 2.3, the effect of force on electron transport properties is less clear. Under these conditions, the changes observed cannot be attributed to changes in electron delocalization or increase frontier orbital energy, since at constant film thickness these values should remain unchanged. This behaviour must be attributed to the manner in which the top electrode (cAFM tip) makes contact with the layer. The dielectric constant within these measurements appear to remain fairly constant under all forces, where as the effective electron mass appears to be reduced. It is unclear from Table 2.3 what effect force has on  $\phi_o$  as no trend is apparent. As discussed earlier, it was found that under higher applied loads, contact area and penetration distances increase. Correcting for the reduced tunneling distance (penetration depth, Table 2.1) within the Simmons model profoundly reduced electron mobility in all cases while only altering  $\phi_o$  and  $\epsilon$ , by a maximum of 3% and <1% respectively. It is evident from the unchanged values of,  $\epsilon$  and  $\phi_o$ , that orbital energies of the layer remain constant under corrections for penetration depth. However, the cause of the increase in effective electron mass is unclear since the above suggests that electron delocalization does not remain constant throughout the layer.

The properties determined via the Simmons Model provide a further insight into how electrons and holes are transported through NAB molecular layers. It has been found that there are several non independent properties that play a significant role in determining IV behaviour. The increased electron mobility and reduced barrier height of thicker films shed light on the less than expected dependence on tunneling distance as noted above. Furthermore it appears that dielectric constants remain unchanged over various applied forces, however, the effect on effective electron mass and barrier height is unclear due to the changes in contact area and tunneling distance.

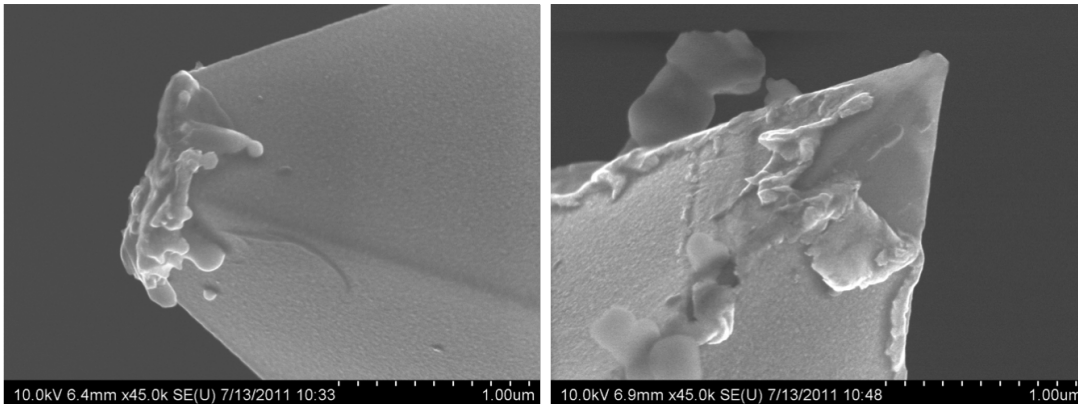


**Figure 2.16:** 10.0 kV high resolution SEM image of used cAFM tips, showing damage resulting from current voltage measurements.

### 2.3.5 Junction Stability

Within electronic devices, stability over operational conditions is of utmost importance. Extending this, molecular electronics and the use of organic molecules calls into question the stability and the rigidity of the molecular layer within these devices. Within most micro-electronic junctions, electrode interfaces are fixed and difficult to characterize. Conductive atomic force microscopy on the other hand, has a unique capability in that the top electrode is mobile. As a result the surface as well as the cAFM tip can be imaged after IV experiments to investigate device components before and after measurement.

With regards to the stability of NAB on PPF, it was found that in some cases after IV measurements electrical contact between the molecular layer and cAFM was lost. To investigate this using the cAFM tip several NAB surfaces were imaged in tapping mode after IV measurements. In most cases clear topographic images could not be obtained. Furthermore, moving the tip to a new location (several  $\mu\text{m}$  away) electrical contact still could not be made. As a result, it was considered that the cAFM tip was damaged and unable to accurately image the surface or make electrical contact. To evaluate this, used cAFM tips were imaged using high resolution SEM, Figure 2.16. Comparing Figure 2.13 to Figure 2.13 it becomes apparent that after IV measurements the cAFM tips have been altered drastically.

It is well known that the motion of charge carriers in a material causes Joule heating. The extent of this heating and the resulting temperature change is dependent on the resistivity, current density and the material's ability to dissipate heat. For bulk conductors

with low resistivities the maximum current density before the melting point is reached is approximately  $10^4$  A/cm<sup>2</sup> [44]. Microelectronics however, involve thin metal films in thermal contact with semi-conducting materials (silicon, silicon oxide, silicon nitride etc.) which dissipate heat allowing current densities to reach  $10^5$  -  $10^6$  A/cm<sup>2</sup> [44]. Due to the very small contact area within cAFM, low amounts of current generate high current densities. Approximating contact area to 100 nm<sup>2</sup> and current to 500 nA (100 nN curve Figure 2.6) the current density is calculated to  $5 \times 10^5$  A/cm<sup>2</sup> within IV measurements of NAB. Assuming that the gold on the cAFM tip acts similarly to other thin metal films on silicon based devices, it is evident that the current densities are approaching the limits set by Joule heating. From this and Figure 2.16, it is not unreasonable to believe that the gold on the cAFM tip is melting causing the molecular junction to fail. This however, does not provide information about the stability of the layer under these conditions. McCreery *et al* [25] have shown NAB junction stability at temperatures of 300° C for 30 minutes but these are far less than the temperatures required to melt gold (>1000° C). Furthermore under the forces investigated it is possible that tip failure is due to mechanical damage. As a result further investigation into the stability of NAB within the molecular junction is required.

### 2.3.6 Conclusion

Electron transport through NAB films on carbon surfaces was investigated by conductive atomic force microscopy. The effect of applied load and film thickness on IV behaviour was studied by considering changes in molecular structure as well as contact area and penetration depth of the cAFM tip. It was found that the NAB structure was constant throughout all measurements, and that increased contact area and reduced tunneling distance played a significant role in conductivity. Furthermore, IV measurements were fit to an adapted Simmons model to determine the properties of the molecular layer in relation to electron transport. It was determined that the trends of increasing dielectric constant, and reduced electron mobility and electron transport barriers at higher film thicknesses were in agreement with McCreery and coworkers implying that electron transport is scaleable between 10s to millions of molecules. Exploring the stability of the molecular junction determined that current densities within these systems are sufficient to irreversibly damage the cAFM tips used.

## References

- [1] McCreery, R. L. *Chemistry of Materials* **2004**, *16*, 4477–4496.
- [2] Cai, L.; Skulason, H.; Kushmerick, J.; Pollack, S.; Naciri, J.; Shashidhar, R.; Allara, D.; Mallouk, T.; Mayer, T. *The Journal of Physical Chemistry B* **2004**, *108*, 2827–2832.
- [3] Kushmerick, J. G.; Lazorcik, J.; Patterson, C. H.; Shashidhar, R.; Seferos, D. S.; Bazan, G. C. *Nano Letters* **2004**, *4*, 639–642.
- [4] Li, X.; Ren, H.; Wang, L.; Cheng, K.; Yang, J.; Luo, Y. *The Journal of Physical Chemistry C* **2010**, *114*, 14240–14242.
- [5] Nijhuis, C. a.; Reus, W. F.; Whitesides, G. M. *Journal of the American Chemical Society* **2009**, *131*, 17814–27.
- [6] McCreery, R.; Dieringer, J.; Solak, A. O.; Snyder, B.; Nowak, A. M.; McGovern, W. R.; DuVall, S. *Journal of the American Chemical Society* **2003**, *125*, 10748–58.
- [7] McCreery, R. L.; Wu, J.; Kalakodimi, R. P. *Physical chemistry chemical physics : PCCP* **2006**, *8*, 2572–90.
- [8] Bergren, A.; McCreery, R.; Stoyanov, S.; Gusarov, S.; Kovalenko, A. *The Journal of Physical Chemistry C* **2010**, 15806–15815.
- [9] Wold, D.; Frisbie, C. *Journal of the American Chemical Society* **2000**, *122*, 2970–2971.
- [10] Wold, D. J.; Frisbie, C. D. *Journal of the American Chemical Society* **2001**, *123*, 5549–56.
- [11] Song, H.; Lee, C.; Kang, Y.; Lee, T. *Colloids and Surfaces A: Physicochemical and Engineering Aspects* **2006**, *284-285*, 583–588.
- [12] Choi, S. H.; Risko, C.; Delgado, M. C. R.; Kim, B.; Brédas, J.-L.; Frisbie, C. D. *Journal of the American Chemical Society* **2010**, *132*, 4358–68.
- [13] Weiss, E. a.; Chiechi, R. C.; Kaufman, G. K.; Kriebel, J. K.; Li, Z.; Duati, M.; Rampi, M. a.; Whitesides, G. M. *Journal of the American Chemical Society* **2007**, *129*, 4336–49.
- [14] Nijhuis, C. A.; Reus, W. F.; Whitesides, G. M. *Journal of the American Chemical Society* **2010**, *132*, 18386–401.

- [15] Nijhuis, C. a.; Reus, W. F.; Barber, J. R.; Dickey, M. D.; Whitesides, G. M. *Nano letters* **2010**, *10*, 3611–9.
- [16] Vericat, C.; Vela, M. E.; Benitez, G.; Carro, P.; Salvarezza, R. C. *Chemical Society reviews* **2010**, *39*, 1805–34.
- [17] Baunach, T.; Ivanova, V.; Kolb, D. M.; Boyen, H.-G.; Ziemann, P.; Bttner, M.; Oelhafen, P. *Advanced Materials* **2004**, *16*, 2024–2028.
- [18] Kind, M.; Wöll, C. *Progress in Surface Science* **2009**, *84*, 230–278.
- [19] Benítez, G.; Vericat, C.; Tanco, S.; Remes Lenicov, F.; Castez, M. F.; Vela, M. E.; Salvarezza, R. C. *Langmuir : the ACS journal of surfaces and colloids* **2004**, *20*, 5030–7.
- [20] Kawaguchi, T.; Yasuda, H.; Shimazu, K.; Porter, M. *Langmuir* **2000**, *16*, 9830–9840.
- [21] Delamarche, E.; Michel, B.; Biebuyck, H.; Gerber, C. *Advanced Materials* **1996**, *8*, 719–729.
- [22] Liu, Z.; Yasserli, A. a.; Lindsey, J. S.; Bocian, D. F. *Science (New York, N.Y.)* **2003**, *302*, 1543–5.
- [23] Delamar, M.; Hitmi, R.; Pinson, J.; Saveant, J. *Journal of the American Chemical Society* **1992**, *114*, 5883–5884.
- [24] Lehr, J.; Williamson, B. E.; Flavel, B. S.; Downard, A. J. *Langmuir : the ACS journal of surfaces and colloids* **2009**, *25*, 13503–9.
- [25] Yan, H.; Bergren, A. J.; McCreery, R. L. *Journal of the American Chemical Society* **2011**.
- [26] Shewchuk, D. M.; McDermott, M. T. *Langmuir : the ACS journal of surfaces and colloids* **2009**, *25*, 4556–63.
- [27] Laurentius, L.; Stoyanov, S. R.; Gusarov, S.; Kovalenko, A.; Du, R.; Lopinski, G. P.; McDermott, M. T. *ACS nano* **2011**, *5*, 4219–27.
- [28] Hurley, B. L.; McCreery, R. L. *Journal of The Electrochemical Society* **2004**, *151*, B252.
- [29] Luo, L.; Choi, S. H.; Frisbie, C. D. *Chemistry of Materials* **2011**, *23*, 631–645.

- [30] Ru, J.; Szeto, B.; Bonifas, A.; McCreery, R. L. *ACS applied materials & interfaces* **2010**, *2*, 3693–701.
- [31] Skulason, H.; Frisbie, C. D. *Langmuir* **2000**, *16*, 6294–6297.
- [32] McCreery, R. L. *Chemistry of Materials* **2004**, *16*, 4477–4496.
- [33] Chisholm, R.; Phd; University of Alberta; 2011.
- [34] Ranganathan, S.; McCreery, R. L. *Analytical Chemistry* **2001**, *73*, 893–900.
- [35] Starkey, E. B. *Sociometry* **1943**, *6*, 68.
- [36] Gam-Derouich, S.; Mahouche-Chergui, S.; Turmine, M.; Piquemal, J.-Y.; Hassen-Chehimi, D. B.; Omastová, M.; Chehimi, M. M. *Surface Science* **2011**, *605*, 1889–1899.
- [37] Paulik, M.; Brooksby, P.; a.D. Abell; a.J. Downard *Journal of Physical Chemistry C* **2007**, *111*, 7808–7815.
- [38] Yang, H.-H.; McCreery, R. L. *Analytical Chemistry* **1999**, *71*, 4081–4087.
- [39] Anariba, F.; Steach, J. K.; McCreery, R. L. *The journal of physical chemistry. B* **2005**, *109*, 11163–72.
- [40] Israelachvili, J. *Intermolecular & Surface Forces*; Academic Press: San Diego, 1992.
- [41] Reedy, E. *Journal of Materials Research* **2007**, *22*, 2617–2622.
- [42] Yang, Y.; Ruths, M. *Langmuir : the ACS journal of surfaces and colloids* **2009**, *25*, 12151–9.
- [43] Joachim, C.; Magoga, M. *Chemical Physics* **2002**, *281*, 347–352.
- [44] Ho, P. S.; Kwok, T. *Reports on the Progress of Physics* **1989**, *301*.

### 3 Diazonium Surface Modification and Characterization

#### 3.1 Introduction

Understanding and developing the field of molecular electronics has hinged on the ability to modify surfaces in a controllable fashion. With the implementation of tools such as scanning tunneling microscopy and atomic force microscopy the ability to accurately visualize and characterize surfaces has vastly improved over the later part of the 20th century. First published in 1983 by Nuzzo and Allara[1], self-assembled alkanethiols on gold have been at the forefront of the modification of noble metal surfaces. Due to their ease of use and controllable functionality self-assembled alkanethiols have been prominent in micro fabrication, molecular electronics, surface wettability, biomedical systems and molecular recognition[2]. The ability for these molecules to form dense, well-ordered monolayers arises from the nature of the gold-sulfur bond. At  $\sim 50 \text{ kcal mol}^{-1}$ [2] the sulfur-gold bond is much stronger than van der Waals forces seen in physisorbed species, but maintains a lability essential for reordering as surface density changes. It is the strength of this gold sulfur bond that has made alkanethiols widely applied but, it too is the source of thermal and electrochemical instability. With a narrow electrochemical window[3] and minimal temperature stability[4] alkanethiols have limited application in current electronics given high operating potentials and temperatures reaching  $\sim 400\text{K}$ [5]. It is within this framework that robust and experimentally simple surface modification is pursued.

First reported by Pinson in 1992 [6], the use of diazonium salts to electrochemically

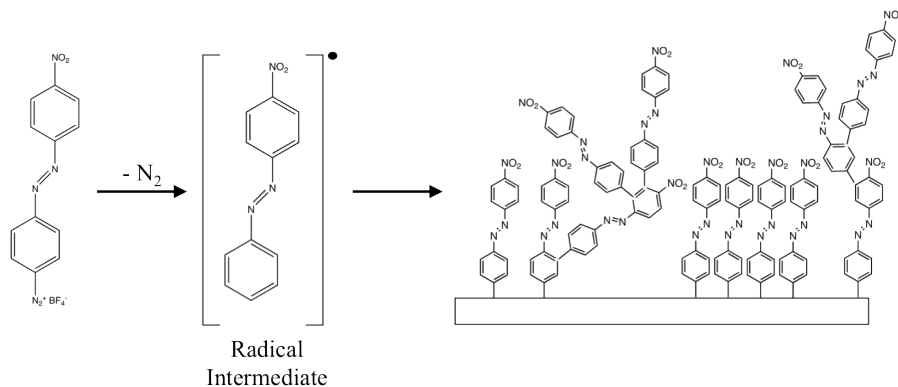


**Figure 3.1:** Proposed mechanism of NAB layer deposition. NAB diazonium salt is reduced to form a radical intermediate which bonds to the electrode surface capable of multilayer formation

modify surfaces has recently become of great interest[7, 8, 9, 10, 11]. Since Pinson’s initial work, investigating nitrobenzene diazonium derived aryl layers on carbon, the field has expanded to encompass a multitude of functional groups for protein binding [12] and photonic crystal formation [13] as well as a variety surfaces including gold, copper, platinum[14] and silicon [15]. Further, the stability of these aryl layers has been shown to out-perform self-assembled alkanethiols under thermal treatment[16], potential cycling in sulfuric acid [17] and ultrasonication[11], while being stable for months under ambient laboratory conditions[6]. Chemists ability to tailor diazonium salts has lead to widespread applications ranging from fuel cells[18] to biological sensors[19, 20].

The formation of diazonium derived layers on conductive surfaces has been shown to occur both spontaneously[21], and electrochemically. It is believed in both processes deposition occurs via the reduction of a diazonium cation producing a radical intermediate. This intermediate then irreversibly binds to the surface due to the close proximity at which reduction occurred. Figure 3.1 presents the mechanism in which diazonium surface modification occurs. Through this process it has been shown that the resulting film is covalently bound to gold and carbon electrode surfaces [8, 22]. Further, researchers have shown it possible to control layer thickness under appropriate conditions [23, 24].

An important step in any surface modification is understanding what occurs at the interface between the surface and the solution. Within electrochemistry, deposition of molecules occurs through two distinct pathways: adsorption controlled or diffusion controlled, Figure 3.2. Within the latter regime, electron transfer occurs as molecules move from bulk solution to the electrode surface under the influence of a concentration difference. Electrochemical

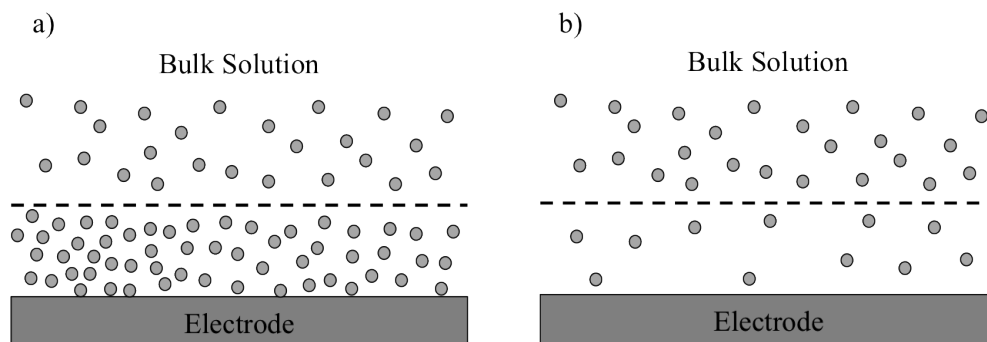


**Figure 3.2:** Schematic depiction of the concentration difference between a) adsorption controlled and b) diffusion controlled deposition. Grey circles represent molecules which participate in electron transfer. Dashed line is included for visual aid.

reduction decreases concentration at the surface, causing molecules to diffuse from the bulk solution towards the electrode. On the other hand, during adsorption controlled deposition, a high concentration (higher than bulk solution) of molecules forms at or near the electrode surface which are subsequently reduced. The rates in which electron transfer occurs for these processes are distinct and yield currents that can be used to understand the mechanism of layer formation.

The work presented in this chapter investigates the nature in which diazonium salt forms molecular layers on gold. Molecular layers of nitroazobenzene (NAB) were formed via cyclic voltametry at various sweep rates and concentrations. Successful deposition of NAB was characterized spectroscopically with Infrared Reflection Absorption Spectroscopy (IR-RAS) and X-ray Photoelectron Spectroscopy (XPS). Film thickness and extent of multilayer growth was determined through Atomic Force Microscopy (AFM).

## 3.2 Experimental

### 3.2.1 Substrate Preparation

Glass microscope slides (Fisher Scientific) were cleaned using a hot piranha solution of 1:3  $\text{H}_2\text{O}_2$ :  $\text{H}_2\text{SO}_4$  for 10 minutes. After cleaning, the slides were rinsed thoroughly under deionized (18 M $\Omega$ ) water, blown dry with  $\text{Ar}_{(g)}$ , and placed into the thermal evaporating system (Torr International Inc.). Metal films of 5 nm chromium and 300 nm gold were deposited onto the slides at  $4 \times 10^{-6}$  mbar. Following this the substrates were stored under house vacuum until use. [Warning: Piranha solution should be handled with extreme care; it is a strong oxidant and reacts violently with many organic materials. It also presents an explosion danger. All work should be performed under a fume hood.]

### 3.2.2 Diazonium Synthesis and Surface Modification

Following a modified procedure of Starkey *et al*[25], nitroazobenzene (NAB) diazonium salt was synthesized from 2.5 g of Disperse Orange 3 (Sigma-Aldrich) precursor. Disperse Orange 3 was partially dissolved in 30 mL of fluoboric acid (Fisher Chemicals) at 0°C under constant stirring. A chilled solution of 5 g of sodium nitrite (ACP Montreal) in 100 mL of deionized (18 M $\Omega$ ) water was added drop-wise over 30 minutes until the reaction was complete. The product was then vacuum filtered using a glass frit and redissolved in cold HPLC grade acetonitrile (Fisher Chemicals). The NAB diazonium salt was recrystallized

by slowly adding chilled ether (Fisher Chemicals) and allowing crystals to form at the solution surface. Following this, the product was vacuum filtered and the filtrate underwent further recrystallization. Once the yield of NAB diazonium salt was sufficient the product was allowed to dry and stored over desiccant at  $-20^{\circ}\text{C}$  until needed. Prior to surface modification gold substrates were cleaned in a 1:3  $\text{H}_2\text{O}_2$ :  $\text{H}_2\text{SO}_4$  hot piranha solution. Following this, substrates were thoroughly rinsed with deionized (18 M $\Omega$ ) water, dried with  $\text{Ar}_{(g)}$  and placed in a three electrode cell with de-aerated NAB diazonium salt solution containing 0.1 M  $\text{Bu}_4\text{NBF}_4$  (Sigma-Aldrich). NAB was deposited electrochemically using a Pine Biopotentiostat model AFCPI controlled by Aftermath software (version 1.2.4532) by cycling the potential from 200 mV to -1000 mV at various rates 10 mV/s, 50 mV/s, 100 mV/s and 200 mV/s against a  $\text{Ag}/\text{AgNO}_3$  reference electrode and platinum mesh counter electrode.

### 3.2.3 Infrared Reflection Absorption Spectroscopy

Infrared reflection absorption spectroscopy (IRRAS) measurements were made using a Matson Infinity FT-IR spectrometer equipped with a mercury-cadmium-tellurium detector cooled to 77K with liquid  $\text{N}_2$  and set to a glancing angle of  $80^{\circ}$ . Spectra were collected over 1000 scans to a resolution of  $2\text{ cm}^{-1}$ . Background spectra were collected using deuterated octadecanethiol monolayers on gold. Between spectra collection the instrument was purged with  $\text{N}_{2(g)}$  for 8 minutes. Spectra were analyzed using Essential FT-IR software.

### 3.2.4 X-Ray Photoelectron Spectroscopy

Modified gold surfaces were studied by XPS using a AXIS Ultra spectrometer (Kratos Analytical) at the Alberta Centre for Surface Engineering and Sciences (ACSES). Samples were measured at a base pressure below  $10^{-7}$  Pa using a monochromated Al  $\text{K}\alpha$  source ( $h\nu = 1486.7\text{ eV}$ ). Survey spectra were taken from 1000 eV to 0 eV binding energy using analyzer pass energy of 160 eV at a resolution of 0.3 eV. High resolution spectra of the N1s region were taken with pass energy of 20 eV and resolution of 0.1 eV.

### 3.2.5 Atomic Force Microscopy Imaging and Film Thickness Measurements

AFM imaging and film thickness measurements were performed using a Nanoscope IIIa Multimode<sup>TM</sup> (Digital Instruments). Measurements were taken under ambient conditions using rectangular Si cantilevers with reflective Al coating (Olympus). The force constant and oscillating frequency of the probes were 40 N/m and  $300 \pm 10\text{ kHz}$  respectively. Film

thickness measurements were performed by “scratching” a  $1 \mu\text{m}^2$  area at high force in contact mode. The area was re-imaged, at  $5 \mu\text{m}^2$ , in tapping mode and the cross sectional average was taken. Control “scratches” were performed on bare substrates to ensure forces were not sufficient to damage the substrate.

### 3.3 Results and Discussion

#### 3.3.1 Deposition and Spectroscopic Characterization of Nitroazobenzene Diazonium salt on gold

Gold substrates were modified with 1 mM nitroazobenzene (NAB) diazonium salt solution using a three electrode cell in the presence of 0.1 M  $\text{Bu}_4\text{NBF}_4$  electrolyte by cycling the potential from 200 mV to -1000 mV against a  $\text{Ag}/\text{Ag}^+$  reference electrode. Infrared reflection absorption spectroscopy (IRRAS) and X-ray photoelectron spectroscopy (XPS) measurements were performed on modified gold slide electrodes to qualitatively confirm successful deposition of NAB. Figure 3.3 displays a typical cyclic voltammogram (CV) for 1 mM NAB deposition. It can be seen that as the potential is swept, a large cathodic peak appears due to the reduction of NAB at the gold electrode. Further, the lack of an oxidation peak

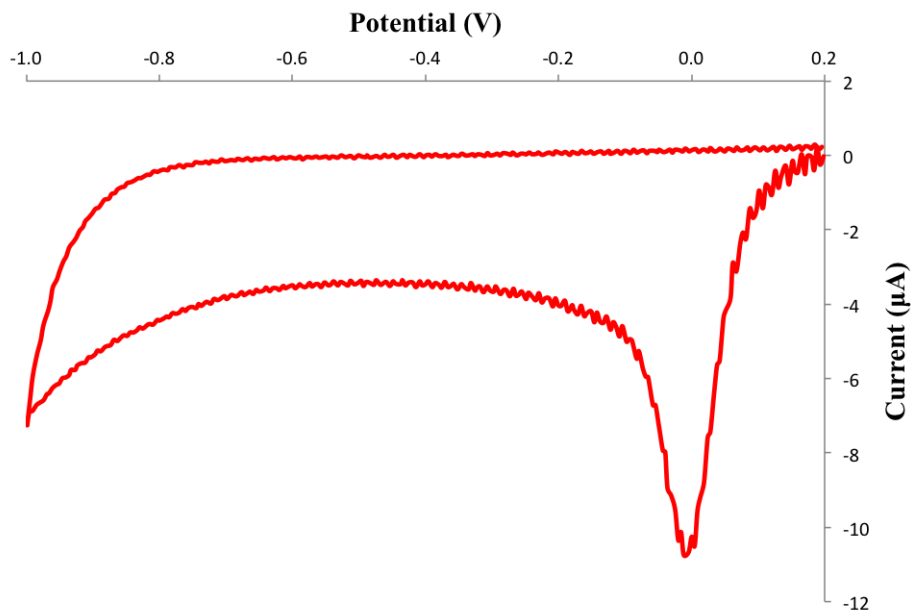


**Figure 3.3:** Cyclic voltammograms of 1 mM NAB diazonium salt solution deposited at 10 mV/s on gold

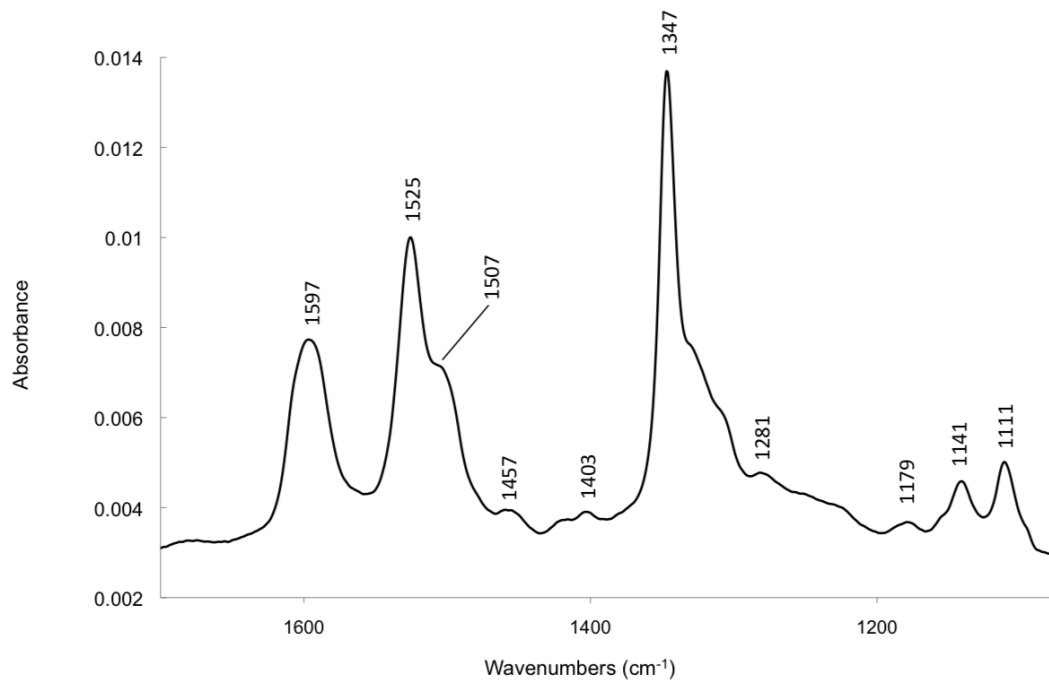


**Figure 3.4:** Infrared Reflection Absorption spectrum of a NAB layer deposited from 1 mM solution at 10 mV/s on gold

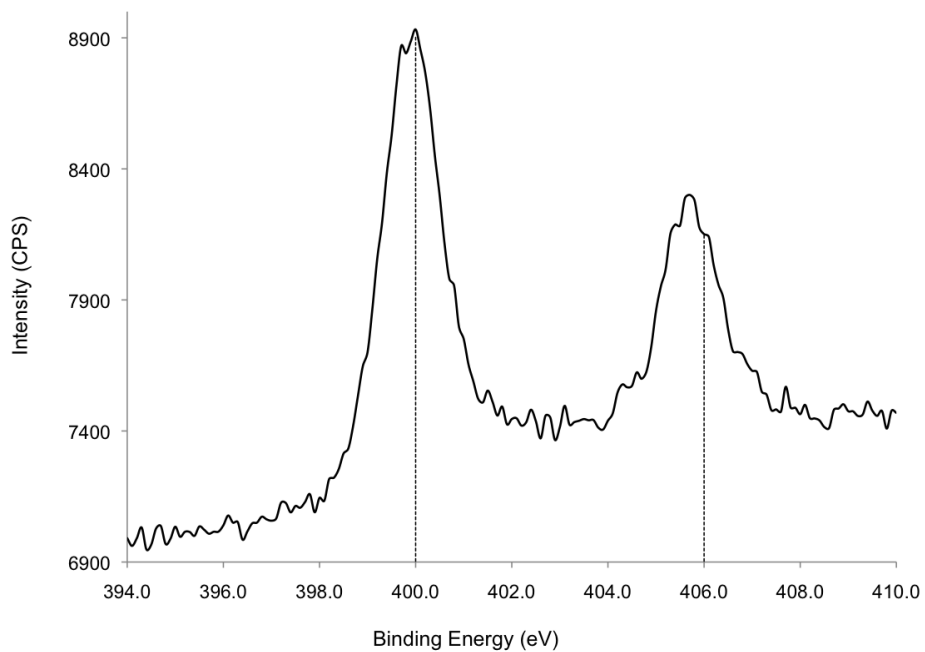


**Figure 3.5:** X-ray Photoelectron spectrum of the N1s region of a NAB layer deposited from 1 mM solution at 10 mV/s.

seen in the CV confirms the chemically irreversible nature of diazonium salt reduction[26]. Note that the “wobble” seen in the CV is a bit limiting artifact from the current setting on the potentiostat and does not affect layer deposition.

Figure 3.4 presents an IRRAS spectrum of NAB modified gold surfaces. The spectrum is dominated by the vibrational modes stemming from the nitro group and aromatic rings of the NAB molecule. The peaks seen at  $1347\text{ cm}^{-1}$  and  $1525\text{ cm}^{-1}$ , have been assigned to the symmetric ( $\nu_{sNO_2}$ ) and asymmetric ( $\nu_{aNO_2}$ )  $NO_2$  stretches respectively, and are consistent with Shewchuk *et al*[27]. As well, peaks arising from benzene ring stretching are evident at  $1597\text{ cm}^{-1}$  and as a shoulder to the  $1525\text{ cm}^{-1}$  asymmetric  $NO_2$  stretch at approximately  $1507\text{ cm}^{-1}$  [28]. Furthermore, phenyl- $NO_2$  and phenyl-NN stretches are seen at  $1111\text{ cm}^{-1}$  and  $1141\text{ cm}^{-1}$  respectively. Finally, small peaks at  $1457\text{ cm}^{-1}$  and  $1403\text{ cm}^{-1}$  are characterized as N=N and N=N-ring stretching modes respectively. The combination of these peaks strongly suggests the presence of NAB on the surface. To further confirm surface modification XPS measurements of the N1s region was performed, Figure 3.5. The N1s region was chosen due to the different binding energies for nitrogen in azo and nitro components of NAB. Figure 3.5 displays two peaks and the presence of two distinct bonding environments for nitrogen. The peak seen at 405.7 eV is resultant from  $NO_2$ , where the larger peak at 400.0 eV is due to N=N [29]. From the characteristic peaks seen in the IRRAS and XPS spectra it was determined that gold surfaces were successfully modified with NAB diazonium salt and proceeded to investigate the effects of sweep rate and concentration NAB despoition and layer growth.

### 3.3.2 Investigation of Nitroazobenzene Diazonium Salt Deposition on gold

Gold substrates were modified with nitroazobenzene (NAB) diazonium salt using a three electrode cell at various concentrations: 1 mM, 500  $\mu\text{M}$ , 200  $\mu\text{M}$  and 100  $\mu\text{M}$  in the presence of 0.1 M  $Bu_4NBF_4$  electrolyte by cycling the potential from 200 mV to -1000 mV against a Ag/Ag<sup>+</sup> reference electrode. At each concentration, NAB was grafted to the gold surface by sweeping the potential at rate of 10 mV/s, 50 mV/s, 100 mV/s and 200 mV/s. Figure 3.6 shows cyclic voltammograms (CV) for NAB diazonium salt deposited at 50 mV/s. Similarly to Figure 3.3, a large cathodic peak is seen due to the reduction of NAB at the gold electrode. Note again that the “wobble” seen in the CVs for lower concentrations is a bit limiting artifact from the current setting on the potentiostat and does not affect layer deposition. It is clear from Figure 3.6 that higher concentrations of NAB diazonium salt produce larger reduction

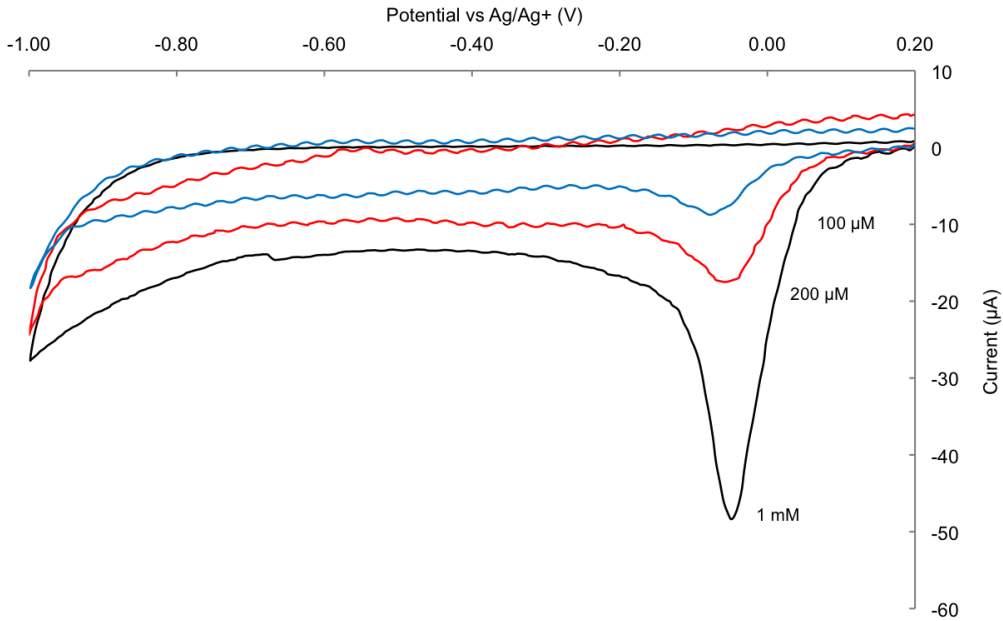


**Figure 3.6:** 50 mV/s cyclic voltammogram of NAB diazonium salt solution at various concentrations on gold

peak currents.

To understand how NAB is reduced at the electrode surface, two situations are considered: solution bound NAB diazonium salt under diffusion control and adsorbed diazonium salt. For diffusion controlled systems, assuming that the reduction of NAB at the surface follows irreversible Nernstian boundary conditions and is a one electron reaction, the peak current,  $i_p$ , is given by[26]:

$$i_p = F A C_o^* D_o^* \nu^{1/2} \left( \frac{\alpha F}{RT} \right)^{1/2} \pi^{1/2} \chi(bt) \quad (3.1)$$

Where,  $F$  is the Faraday constant,  $A$  is the area,  $D_o^*$  is the diffusion coefficient,  $C_o^*$  is the bulk concentration,  $\nu$  is the sweep rate,  $R$  is the resistance,  $T$  is the absolute temperature,  $\alpha$  is the transfer coefficient and  $\chi(bt)$  is a tabulated value of a function determining the normalized charge transfer for irreversible systems. For our purposes  $i_p$  can be reduced to

$$i_p = B \nu^{1/2} \quad (3.2)$$

where

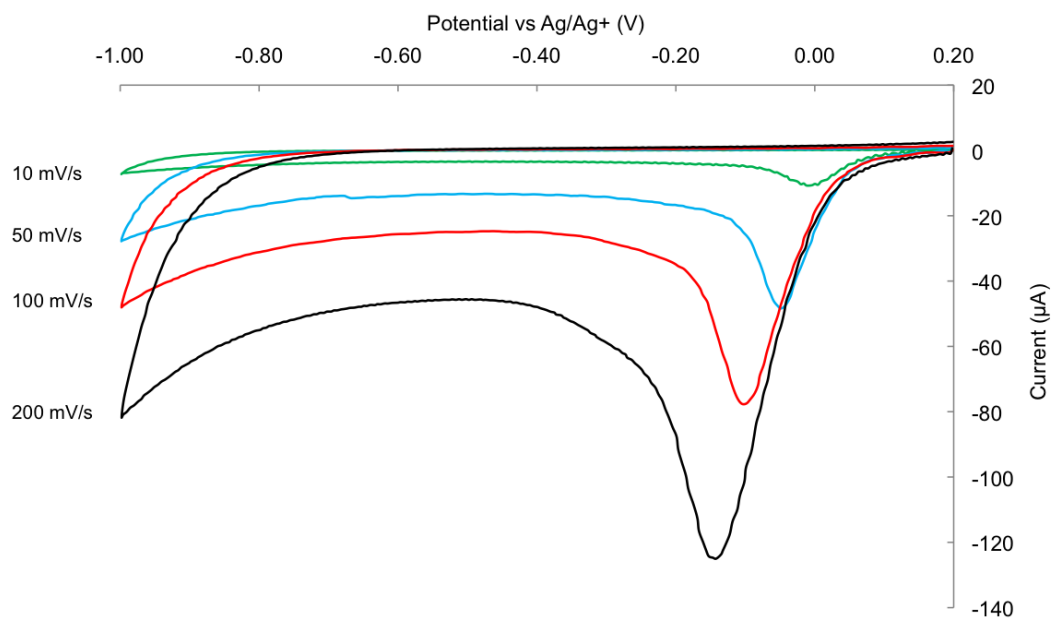


**Figure 3.7:** Cyclic voltammograms of 1 mM NAB diazonium salt solution deposited at various sweep rates on gold.

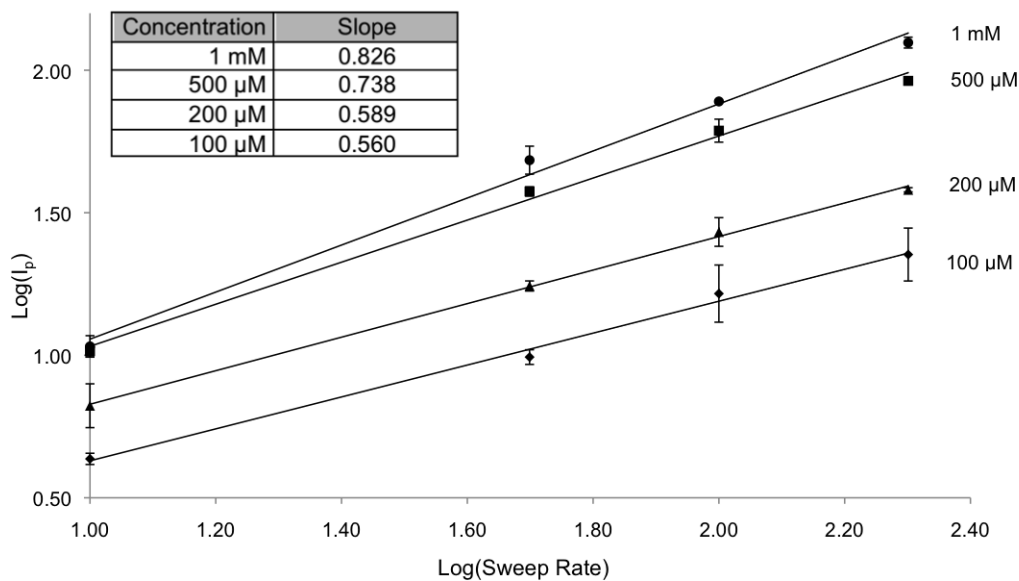


**Figure 3.8:**  $\log(i_p)$   $\log(\nu)$  plot of NAB deposition at various concentrations. Inset shows the slopes determined for each concentration.

$$B = FAC_o^*D_o^* \left( \frac{\alpha F}{RT} \right) \pi^{1/2} \chi(bt)$$

From equation 3.2 it is seen that the peak current is proportional to the square root of the sweep rate for diffusion controlled deposition. For species that are adsorbed to the surface and follow a Nernstian reaction the peak current is determined by:

$$i_p = \frac{n^2 F^2}{4RT} \nu A \Gamma_o^* \quad (3.3)$$

where  $n$  is the number of electrons and  $\Gamma_o^*$  is the surface species excess at equilibrium. Similarly this is reduced to

$$i_p = G\nu \quad (3.4)$$

where

$$G = \frac{n^2 F^2}{4RT} A \Gamma_o^*$$

Equation 3.4 shows the peak current for surface adsorbed species is directly proportional to the sweep rate, this differs distinctly from Equation 3.2 for diffusion controlled systems. To probe which regime controls deposition of NAB, surfaces were modified under different sweep rates,  $\nu$ , and concentrations. Figure 3.7 shows CVs for 1 mM solution of NAB diazonium salt at various sweep rates. It can be seen that peak potential,  $E_p$ , increases (negatively) with sweep rate. This is characteristic of a quasi-reversible redox system[26].

From equations 3.2 and 3.4 plotting  $\log(i_p)$  vs.  $\log(\nu)$  and determining the slope will provide information on which regime controls NAB deposition. For purely adsorption controlled systems it is expected that the  $\log(i_p)$  will be directly proportional to  $\log(\nu)$  yielding  $slope = 1$ . On the other hand the squareroot dependence within diffusion controlled systems will produce  $slope = 0.5$ . Figure 3.8 shows  $\log(i_p)$  vs  $\log(\nu)$  for 1mM, 500  $\mu$ M, 200  $\mu$ M and 100  $\mu$ M and their respective slopes, inset. From this it is clear that higher concentrations yield slopes between 0.5 and 1 implying that peak current is determined by both adsorbed and diffusing NAB diazonium cations. At lower concentrations the slopes of the  $\log(i_p)$  vs.  $\log(\nu)$  are approximately 0.5 indicating that current results mainly from diffusing NAB diazonium cations. This result is counter intuitive due to the relationship between diffusion current and concentration. From Equation 3.1 it is evident that  $i_p$  is de-

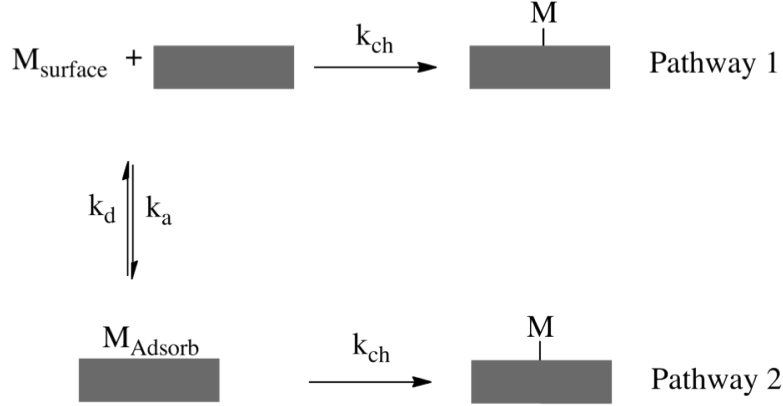


**Figure 3.9:** Proposed pathways for diazonium adsorption. Pathway 1) direct chemisorption from solution with rate constant  $k_{ch}$ . Pathway 2) equilibrium between physisorption and desorption as determined by rate constants,  $k_a$  and  $k_d$ , followed by chemisorption

pendent on bulk concentration,  $C_o^*$ , and thus diffusion should dominate deposition at higher concentrations. However, the results of Figure 3.8 can be explained upon considering the work by Jayasundara *et al*[21]who found that Langmuir reversible adsorption best describes deposition of diazonium salts on gold. From Jayasundara *et al* [21] spontaneous adsorption of nitrobenzene diazonium salt can follow one of two pathways, shown in Figure 3.9. Within this, molecules close to the electrode,  $M_{\text{surface}}$  can interact with the surface by chemically bonding or by adsorbing through van der Waals forces,  $M_{\text{Adsorb}}$ .

In both cases the surface coverage,  $\theta$ , is understood through the Langmuir Equation, equation 3.5, where it is assumed that all adsorption sites are equivalent, adsorbates are immobile and do not interact and that the surface is unchanged and homogeneous.

$$k = \frac{\theta}{C \cdot (1 - \theta)} \quad (3.5)$$

Following pathway one, the diazonium is directly reduced to the electrode surface and coverage is dependent on the chemisorption rate constant,  $k_{ch}$ , and the concentration  $C$ . Under these conditions it is simple to determine the change in coverage over time

$$\frac{d\theta}{dt} = k_{ch}(1 - \theta) \cdot C \quad (3.6)$$

Integrating with respect to time

$$\theta(t) = 1 - e^{-Ctk_{ch}} \quad (3.7)$$

Following this mechanism the diazonium would be irreversibly reduced at the surface and electron transfer would be complete with no intermediate steps. If this pathway were taken the chemisorbed molecules would no longer be available for reduction and would not generate any current during cyclic voltametry. Under the second pathway molecules adsorb to the surface but are not immediately reduced. The change in coverage over time is given by:

$$\frac{d\theta}{dt} = k_a(1 - \theta) \cdot C - k_d\theta$$

Under these conditions there are two possible routes; desorption or reduction to the surface. If it is assumed that the rate of reduction is much faster than that of desorption,  $k_{ch} \gg k_d$ , the net effect would be determined by the rate of adsorption and the above equation would be reduced to equation 3.6. However, if the rate of reduction is such that  $k_{ch} \ll k_d$  then the above equation is valid, as an equilibrium between adsorption and desorption would occur. Integrating the above equation yields:

$$\theta(t) = A[1 - e^{-k_{obs}t}] \quad (3.8)$$

Where  $A = k_a \cdot C / (1 + k_d/k_a \cdot C)$  and  $k_{obs}$ , the observed rate constant, is given by  $k_{obs} = k_a \cdot C + k_d$ . By monitoring monolayer formation using quartz crystal microbalance (QCM) Jayasundara *et al* [21] found that equation 3.8 best described the adsorption of nitrobenzene to the gold surface. Further, it was seen that for concentrations above 100  $\mu\text{M}$ , monolayer formation is very rapid, occurring on the order of seconds. Relating this to the deposition of NAB, at higher concentrations adsorption is very rapid and the change in  $i_p$  is in part determined by adsorbed NAB species. For lower concentrations adsorption does occur but at much slower rates resulting in  $i_p$  being controlled by diffusion. From Figure 3.8 it can be seen, that at higher concentrations the deposition does not result from purely adsorbed NAB (*slope*  $\neq 1$ ). The peak current in this case is dependent on both adsorbed and diffusing of NAB diazonium cations. From Jayasundara *et al* and the results in Figure 3.8 it is apparent that adsorption of NAB diazonium to the surface do not play a significant role in peak current for concentrations below 500  $\mu\text{M}$ .

### 3.3.3 Analysis of Multilayer Formation of NAB Layers.

The topography and thickness of aryl layers deposited at different concentrations and sweep rates were obtained by atomic force microscopy (AFM). To compare the unmodified gold surface and NAB modified surfaces, initial images of unmodified substrates were taken, Figure 3.10a. The thermally evaporated gold electrode is rough and composed of small gold crystallites. In comparing this to the modified surface, Figure 3.10c it is evident that there is little noticeable difference between the modified and unmodified topography. It appears that the topography of NAB on the surface is templated by the underlying gold structure.

To determine film thickness, AFM “scratching” measurements were made on modified gold electrodes. AFM scratching has been shown to be an accurate way to measure organic film thicknesses [30, 31, 32]. This method involves repeatedly rastering the AFM tip over and area with forces sufficient to remove the adsorbed aryl layer but not enough to damage the substrate below. The affected area is re-imaged over a larger area with tapping mode AFM. From these images, a cross sectional profile across the bare substrate and the intact film provides information on layer thickness and the multilayered nature of NAB.

Film thickness measurements were made by scratching a  $1 \mu\text{m}^2$  area and re-imaging over  $5 \mu\text{m}^2$ . To ensure that the forces used to remove the aryl layer were not great enough to damage the underlying gold substrate, bare electrodes were scratched at high forces and re-imaged. Figure 3.10b shows a bare gold electrode that was scratched at forces sufficient to remove NAB from the surface. From this there is no clear modification or height difference between the scratched area (centre) and the surrounding intact substrate. Figure 3.10d presents an image of the displaced film shown in Figure 3.10c displaying a clear distinction between the substrate and the undamaged NAB layer. Taking the cross sectional average over the  $5 \mu\text{m}^2$  image and  $1 \mu\text{m}^2$  scratched area provides the height of the of the deposited NAB film. Figure 3.11 displays the measured film thickness of various samples. Note that error bars were removed for clarity. Film thickness values along with standard deviation are displayed in Table 3.1.

From Figure 3.11 the effect of concentration and sweep rate on film thickness is evident. Intuitively more concentrated solutions yield thicker films and *vice versa*. Further, faster sweep rates produce thinner films than slower rates, even though the peak current observed in cyclic voltammograms for 200 mV/s is much greater than that for 10 mV/s (Figure 3.7). This is explained by the fact that slower sweep rates naturally take longer and as a result the

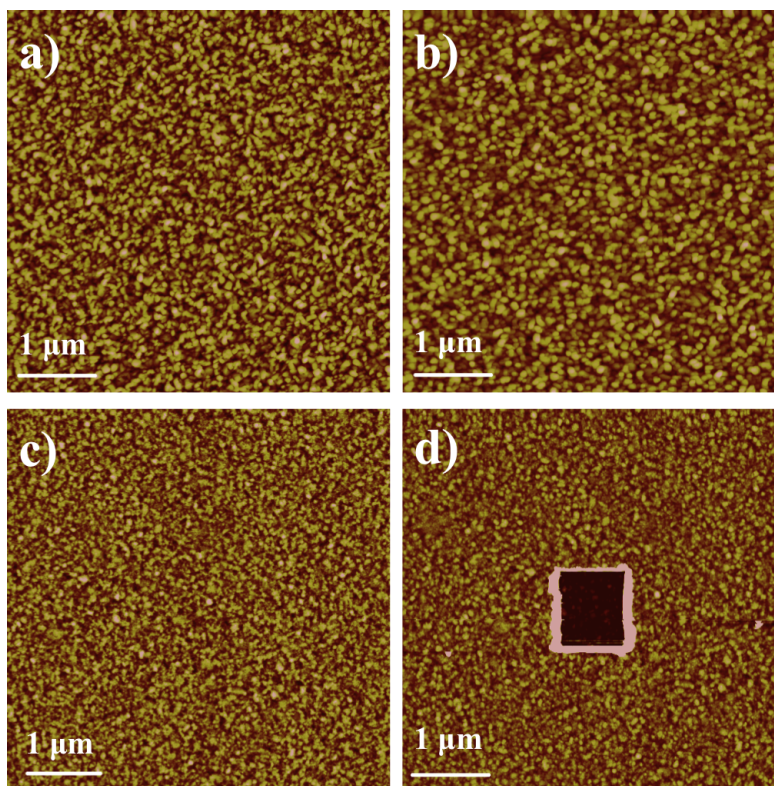


**Figure 3.10:**  $5 \mu\text{m}^2$  AFM tapping mode images a) bare gold substrate b) scratched gold substrate c)  $500 \mu\text{M}$  NAB layer deposited at  $10 \text{ mV/s}$  on gold d) scratched  $500 \mu\text{M}$  NAB layer deposited at  $10 \text{ mV/s}$  on gold. The z-scale for all images is  $20 \text{ nm}$

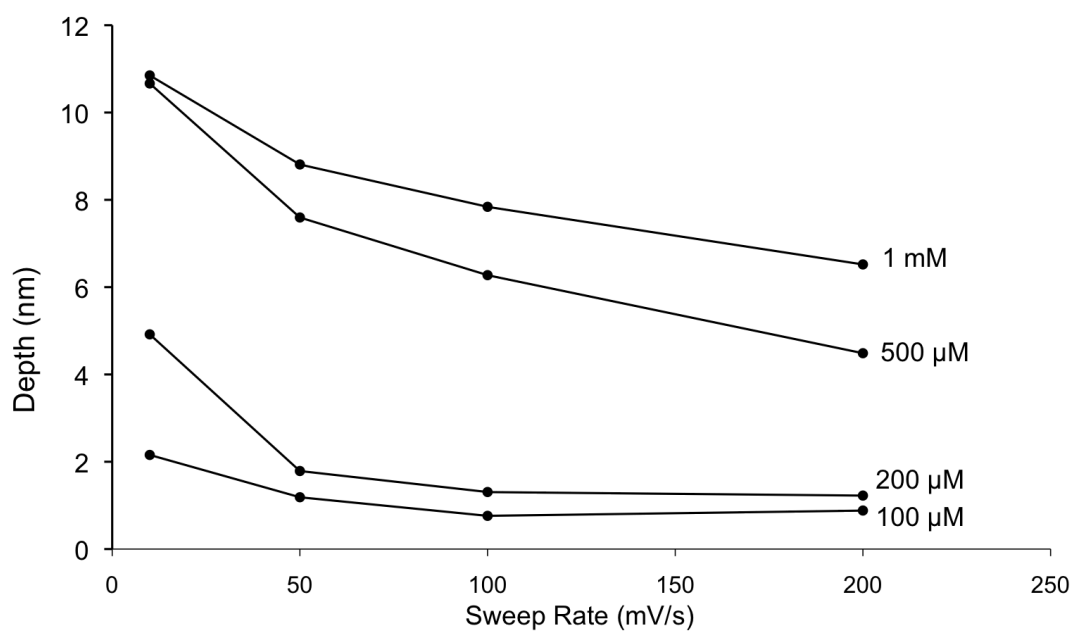


**Figure 3.11:** Film thicknesses as determined by AFM scratching measurements.

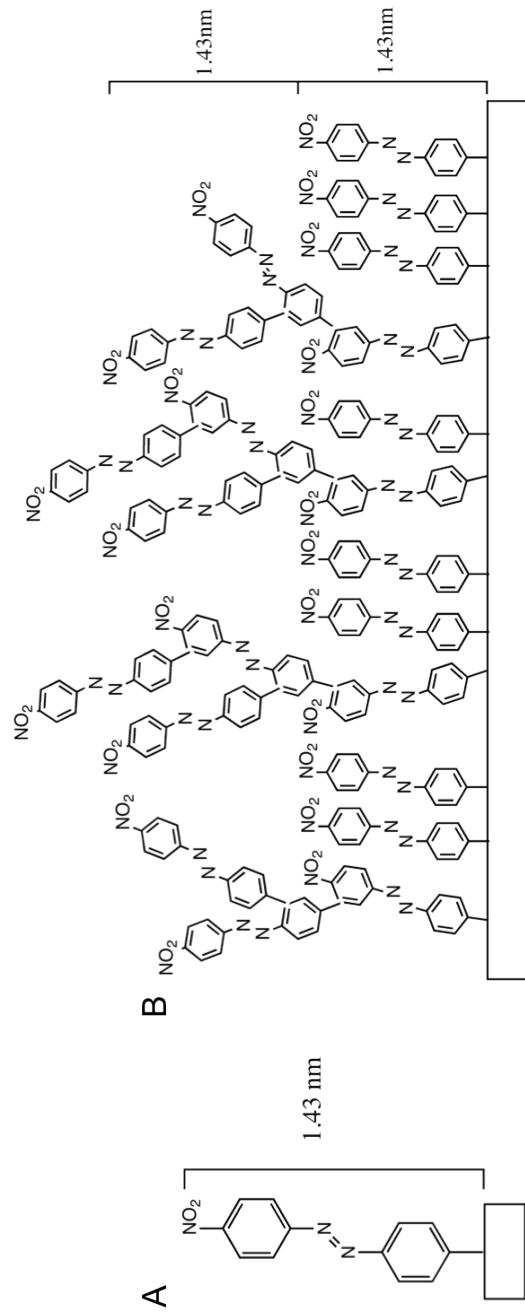


**Figure 3.12:** A) a single NAB molecule adsorbed along the surface normal B) Proposed multilayered structure of NAB films.

**Table 3.1:** Film thicknesses as determined by AFM scratching measurements. Errors reported are the standard deviations of the cross sectional average of NAB films.

Sweep Rate (mV/s)	10		50		100		200	
Concentration	Thickness (nm)	# of Layers						
1 mM	11 ± 1	7.69	9 ± 1	6.29	7.8 ± 0.8	5.45	7 ± 1	4.90
500 μM	10.7 ± 0.5	7.48	7.6 ± 0.5	5.31	6.3 ± 0.4	4.41	4.5 ± 0.6	3.15
200 μM	4.9 ± 0.6	3.43	1.8 ± 0.4	1.26	1.3 ± 0.6	0.91	1.2 ± 0.8	0.84
100 μM	2.1 ± 0.7	1.47	1.2 ± 0.6	0.84	0.8 ± 0.5	0.56	0.9 ± 0.6	0.63

reduction potential is maintained for a greater period of time. The film grows thicker over the prolonged time the reduction potential was applied. Upon further analysis of Figure 3.11 there is a distinct separation between concentrations above and below 500 μM. This finding further supports the different mechanisms of NAB deposition described to in section 2.3.1.

To determine the nature of layer growth, film thicknesses were compared to the size of individual NAB molecules. Figure 3.12a shows the height of a NAB molecule bound perpendicularly to a surface at 1.43 nm [30]. The orientation in which subsequent molecules deposit is not strictly understood and possible bonding configurations are shown in Figure 3.12b. Within this scheme there is no clear distinction between layers. As a result a monolayer of NAB is considered to be 1.43 nm thick, and multilayers are approximated as multiples of this, thus 2 layers of NAB is 2.86 nm thick and so on. Table 3.1 shows film thicknesses of samples deposited under various conditions along with the number of layers within the film. The errors stated were determined by taking the standard deviation across the intact region of the cross sectional average. It should be noted that this error is highly dependent on the structure and irregularity of the gold substrate and differs between samples. From this table it is evident that by adjusting the concentration and sweep rate of deposition, multilayer growth can be controlled. Furthermore, multilayer growth does not appear to follow 1.43 nm regularity indicating a less ordered layer growth as illustrated in Figure 3.12B.

### 3.4 Conclusion

This work has shown successful modification of gold electrodes by electrochemically reducing NAB. The manner in which these films grow was investigated by comparing ad-

sorption and diffusion controlled deposition regimes. It was found that film growth at concentrations above 500  $\mu\text{M}$  is strongly influenced by adsorbed species where for concentrations below 500  $\mu\text{M}$  growth is controlled by diffusion of molecules from bulk solution to the electrode surface. The thickness of the films were determined by AFM scratching techniques and seen to be highly dependent on sweep rate and concentration. The structure and multilayer nature of these films were determined to be irregular and unordered.

## References

- [1] Nuzzo, R.; Allara, D. *Journal of the American Chemical Society* **1983**, *105*, 4481–4483.
- [2] Vericat, C.; Vela, M. E.; Benitez, G.; Carro, P.; Salvarezza, R. C. *Chemical Society reviews* **2010**, *39*, 1805–34.
- [3] Kawaguchi, T.; Yasuda, H.; Shimazu, K.; Porter, M. *Langmuir* **2000**, *16*, 9830–9840.
- [4] Delamarche, E.; Michel, B.; Biebuyck, H.; Gerber, C. *Advanced Materials* **1996**, *8*, 719–729.
- [5] Liu, Z.; Yasserli, A. a.; Lindsey, J. S.; Bocian, D. F. *Science (New York, N.Y.)* **2003**, *302*, 1543–5.
- [6] Delamar, M.; Hitmi, R.; Pinson, J.; Saveant, J. *Journal of the American Chemical Society* **1992**, *114*, 5883–5884.
- [7] Ceccato, M.; Bousquet, A.; Hinge, M.; Pedersen, S.; Daasbjerg, K. *Chemistry of Materials* **2011**, 110218074748045.
- [8] Laurentius, L.; Stoyanov, S. R.; Gusarov, S.; Kovalenko, A.; Du, R.; Lopinski, G. P.; McDermott, M. T. *ACS nano* **2011**, *5*, 4219–27.
- [9] McCreery, R. L.; Wu, J.; Kalakodimi, R. P. *Physical chemistry chemical physics : PCCP* **2006**, *8*, 2572–90.
- [10] Leroux, Y. R.; Hui, F.; Noël, J.-M.; Roux, C.; Downard, A. J.; Hapiot, P. *Langmuir : the ACS journal of surfaces and colloids* **2011**, *27*, 11222–8.
- [11] Shewchuk, D. M.; McDermott, M. T. *Langmuir : the ACS journal of surfaces and colloids* **2009**, *25*, 4556–63.
- [12] Corgier, B. P.; Marquette, C. A.; Blum, L. J. *Journal of the American Chemical Society* **2005**, *127*, 18328–32.
- [13] Thompson, C. M.; Ruminski, A. M.; Sega, A. G.; Sailor, M. J.; Miskelly, G. M. *Langmuir : the ACS journal of surfaces and colloids* **2011**, *27*, 8967–73.
- [14] Bonifas, A. P.; McCreery, R. L. *Nature nanotechnology* **2010**, *5*, 612–7.

- [15] Zhang, X.; Wen, Y.; Li, Y.; Li, G.; Du, S.; Guo, H.; Yang, L.; Jiang, L.; Gao, H.; Song, Y. *Journal of Physical Chemistry C* **2008**, *112*, 8288–8293.
- [16] Mahmoud, A. M.; Bergren, A. J.; Pekas, N.; McCreery, R. L. *Advanced Functional Materials* **2011**, *21*, 2273–2281.
- [17] Paulik, M.; Brooksby, P.; a.D. Abell; a.J. Downard *Journal of Physical Chemistry C* **2007**, *111*, 7808–7815.
- [18] Picot, M.; Lapinsonnière, L.; Rothballer, M.; Barrière, F. *Biosensors & bioelectronics* **2011**, *28*, 181–8.
- [19] Polsky, R.; Harper, J. C.; Dirk, S. M.; Arango, D. C.; Wheeler, D. R.; Brozik, S. M. *Langmuir* **2007**, *23*, 364–6.
- [20] Harper, J. C.; Polsky, R.; Wheeler, D. R.; Dirk, S. M.; Brozik, S. M. *Langmuir : the ACS journal of surfaces and colloids* **2007**, *23*, 8285–7.
- [21] Jayasundara, D. R.; Cullen, R. J.; Soldi, L.; Colavita, P. E. *Langmuir* **2011**.
- [22] Pinson, J.; Podvorica, F. *Chemical Society reviews* **2005**, *34*, 429–39.
- [23] McCreery, R.; Dieringer, J.; Solak, A. O.; Snyder, B.; Nowak, A. M.; McGovern, W. R.; DuVall, S. *Journal of the American Chemical Society* **2003**, *125*, 10748–58.
- [24] Ru, J.; Szeto, B.; Bonifas, A.; McCreery, R. L. *ACS applied materials & interfaces* **2010**, *2*, 3693–701.
- [25] Starkey, E. B. *Sociometry* **1943**, *6*, 68.
- [26] Bard, A. J.; Faulkner, L. R. *Electrochemical Methods: Fundamentals and Applications*, 2nd ed.; Wiley & Sons: New York, 2000.
- [27] Shewchuk, D. M.; Reid, M.; Mcdermott, M. T.
- [28] Itoh, T.; McCreery, R. L. *Journal of the American Chemical Society* **2002**, *124*, 10894–902.
- [29] Nowak, A. M.; McCreery, R. L. *Analytical chemistry* **2004**, *76*, 1089–97.
- [30] Anariba, F.; DuVall, S. H.; McCreery, R. L. *Analytical chemistry* **2003**, *75*, 3837–44.

- [31] Brooksby, P. a.; Downard, A. J. *Langmuir : the ACS journal of surfaces and colloids* **2005**, *21*, 1672–5.
- [32] Fave, C.; Leroux, Y.; Trippé, G.; Randriamahazaka, H.; Noel, V.; Lacroix, J.-C. *Journal of the American Chemical Society* **2007**, *129*, 1890–1.

## 4 Electron Transport Through Mixed-Mode Bonded Layers on Gold

### 4.1 Introduction

Current electronic devices can operate under high temperature, pressure and voltage ranges[1, 2]. Within these systems, silicon-based semiconductors possess a rigid framework which provides stability over a variety of operational conditions. Organic layers however, are well known to be dynamic systems and have been shown to be highly dependent on; temperature, pressure and surface material[3, 4, 5]. As a result in order to adapt molecular junctions to conventional electronics, it is important to explore electron transport within a range of conditions<sup>1</sup>.

Over the last several decades, with the development of techniques such as; surface enhance Raman spectroscopy (SERS), scanning electron microscopy (SEM) and atomic force microscopy (AFM), scientists have been able to thoroughly investigate and characterize a countless number of surfaces. As a result, molecular surface modification has grown to become an extremely rich field, ranging from sophisticated reaction pathways within photovoltaics to much simpler self-assembled systems[6]. Within the latter, there have been numerous studies involving organosilanes, alkanethiols and aryl diazonium layers; which graft either spontaneously or under the influence of light, potential bias or heat[6]. Many of these systems have significant roles in device fabrication[7], bioassays[5], and nano-structure formation [8].

Since their introduction by Nuzzo in 1983 [9], thiol based self-assembled monolayers (SAMs) on gold have been at the forefront of organic surface modification. The growth in popularity of SAMs over the last 30 years can be attributed to both the simple deposition procedure as well as the wide variety of ligands and functional groups that can be synthesized. Within this, alkanethiols have received the majority of interest due to their ability to form dense well ordered monolayers. As a result, alkanethiols have been thoroughly characterized on a variety of surfaces (gold, copper, silver, etc.) and under various environmental conditions (temperature, redox species, etc)[8, 5]. Furthermore, Frisbie *et al.* have extensively studied alkanethiols within molecular junctions *via* conductive atomic force

---

<sup>1</sup>A portion of this chapter has been submitted for publication as Shewchuck, D. M., Reid, M. S., McDermott, M. T. "Mixed-Mode Bonded Layers on Gold: Characterization of Mixed Layers of Diazonium Derived Aryl Molecules and Alkanethiolates" Langmuir, submitted.

microscopy (cAFM), finding that electron transport is greatly influenced by chain length and contact force[3, 10, 11]. (Note that all future reference to self assembled monolayers, SAMs, refer to alkanethiols on gold).

As discussed in previous chapters, diazonium salts offer an interesting pathway for surface modification. First reported by Pinson *et al.*, diazonium salts have grown in popularity and shown to produce stable molecular layers both spontaneously[12, 13] and electrochemically[14, 15, 16]. Furthermore, unlike monolayer formation within SAMs, radical formation during deposition can produce film coverages ranging from submonolayer[17, 18] to several hundred nanometers[19]. McCreery *et al.* have developed large scale diazonium derived molecular junctions that are stable over millions of cycles and a wide range of temperatures[20]. Work extensively characterizing electron transport through diazonium layers however, has been limited to carbon and copper, due to penetration of metallic atoms into the organic layer during vapour deposition[21]. As a result, it is unclear how contact material influences charge transport.

Another approach extends organic surface modification to incorporate mixed molecular layers and it can be considered to serve two distinct goals; to create a film with properties that fit a desired application or to isolate a region/molecule of interest on the surface. The monolayer formation within SAMs naturally allows for distinction between molecular species within the mixed layer resulting from different chain lengths, Figure 4.1a. As a result, formation of mixed alkanethiol layers has been extensively shown through patterning[22, 23, 24] and coadsorption[25]. Mixed molecular layers solely derived from diazonium salts, on the other hand have proven to be much more difficult to characterize due to the radical, unselective formation of multilayers, Figure 4.1b. Downard *et al.* have recently displayed

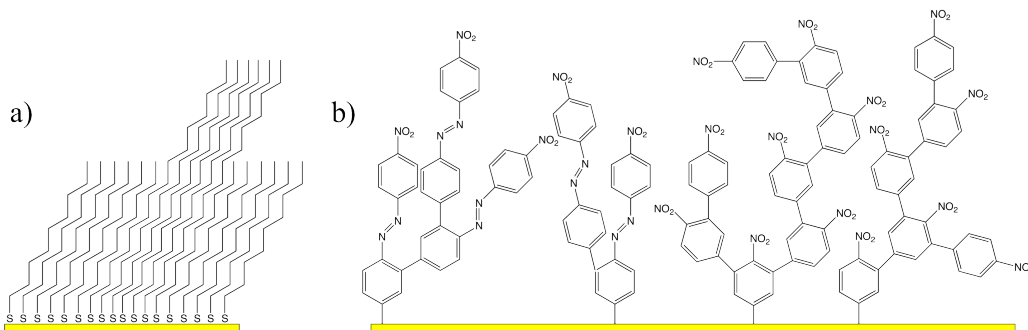


**Figure 4.1:** Schematic representation of the difference between mixed organic layers a) mixed alkanethiols, b) diazonium derived

binary diazonium layers created by back filling scratched diazonium layers[26] and two step grafting processes[27].

Molecular layers on gold; will not only provide insight into the effect of contact material on electron transport but also yield a unique opportunity to investigate mixed molecular layers composed of both covalently bound diazonium species and alkanethiols. The work presented in this chapter seeks to characterize these systems and understand how electron transport is affected. Organic films of nitroazobenzene (NAB) were deposited electrochemically by cyclic voltammetry on gold electrodes. Template stripped (TS) gold surfaces were used to aid in the study of surface topography and electron transport due to large crystallite size and low surface roughness. Mixed layers of NAB and dodecanethiol (DDT) were created by incubating NAB modified surfaces overnight in thiol solution. Surfaces were characterized by infrared reflection absorption spectroscopy (IRRAS), atomic force microscopy (AFM) and scanning electron microscopy (SEM). Current voltage (IV) behaviour of both pure and mixed layers was studied by conductive atomic force microscopy (cAFM). Furthermore the influence of film thickness and diazonium surface coverage on electron transport was investigated. The Simmons model was used to determine fundamental electron transport properties within the organic layer.

## 4.2 Experimental

### 4.2.1 Template Stripped Gold

Following the Blackstock *et al* procedure[28], (Figure 4.2) silicon wafers were cleaned using a hot piranha solution of 1:3  $\text{H}_2\text{O}_2$  :  $\text{H}_2\text{SO}_4$  for 10 minutes. After cleaning, wafers were thoroughly rinsing with deionized (18 M $\Omega$ ) water and dried with  $\text{Ar}_{(g)}$ . Wafers were then placed in the thermal evaporating system (Torr International Inc.) where 300 nm of gold was deposited under  $4 \times 10^{-6}$  mbar pressure. Mounting substrates ( 1 cm square silicon wafer) were bonded to the exposed Au surface with EPO-TEK 377 (Epoxy Technologies, MA) epoxy and baked at 150 °C for 1 h until cured. Template stripped (TS) gold substrates were stored under house vacuum and removed from the silicon wafer as needed.



**Figure 4.2:** Simplified view of the template stripped process where grey: clean silicon wafer, yellow: gold, black: mounting substrate

## 4.2.2 Conductive Atomic Force Microscopy Tip Fabrication

Contact mode silicon nitride atomic force microscopy (AFM) tips (Nanoprobe <sup>TM</sup>) were cleaved from the wafer and placed into a thermal evaporating system (Torr International Inc.). Tips were metallized under  $4 \times 10^{-6}$  mbar pressure by depositing 3 nm of chromium followed by 45 nm of gold onto the cantilever surface. Gold modified conductive atomic force microscopy (cAFM) tips were stored in atmospheric conditions and used within a week of modification.

## 4.2.3 Surface Modification

Nitroazobenzene (NAB) diazonium salts were synthesized as described earlier in Section 2.2.2. Gold substrates for infrared reflection absorption spectroscopy were prepared and modified with NAB diazonium salt solution following the same procedure as in Sections 3.2.1 and 3.2.2. Recall, clean substrates were thoroughly rinsed with deionized (18 M $\Omega$ ) water, dried with Ar<sub>(g)</sub> and placed in a three electrode cell with de-aerated NAB diazonium salt solution containing 0.1 M Bu<sub>4</sub>NBF<sub>4</sub> (Sigma-Aldrich). NAB was deposited electrochemically using a Pine Biopotentiostat model AFCPI controlled by Aftermath software (version 1.2.4532) by cycling the potential from 200 mV to -800 mV at various rates against a Ag/AgNO<sub>3</sub> reference electrode and platinum mesh counter electrode. Template stripped gold substrates were modified under the same conditions within an o-ring electrochemical cell. Fresh, 1 mM dodecanethiol (DDT) solutions were prepared with anhydrous ethanol prior to surface modification and de-aerated with Ag<sub>(g)</sub>. Following NAB surface modification and characterization samples were immersed in DDT solution over night.

## 4.2.4 Infrared Reflection Adsorption Spectroscopy

Infrared reflection absorption spectroscopy (IRRAS) measurements were made, as described in Section 2.2.3, using a Matson Infinity FT-IR spectrometer equipped with a mercury-cadmium-tellurium detector cooled to 77K with liquid N<sub>2</sub> and set to a glancing angle of 80°. IRRAS spectra were collected for both NAB and DDT modified surfaces. Spectra were analyzed and compared using Essential FT-IR software.

#### 4.2.5 Atomic Force Microscopy

Atomic force microscopy (AFM) imaging was performed using a Nanoscope IIIa Multimode<sup>TM</sup> (Digital Instruments). Measurements were taken under ambient conditions using rectangular Si cantilevers with reflective Al coating (Olympus). The force constant and oscillating frequency of the probes were 40 N/m and  $300 \pm 10$  kHz respectively. Using ImageJ software NAB and DDT surface coverage within the mixed-mode bonded layers was determined by thresholding the pixel intensity of the height images to separate the two phases.

#### 4.2.6 Conductive Atomic Force Microscopy

Conductive atomic force microscopy (cAFM) was performed using a modified Nanoscope IIIa Multimode<sup>TM</sup> (Digital Instruments) and an external Reference 600 potentiostat (Gamry Instruments) as described in Section 3.2.4. Recall current voltage (IV) curves were taken in ambient conditions by cycling the potential from -2 V to 2 V against an internal reference within the Gamry potentiostat. Top electrical contact was made by bringing a modified AFM tip (Section 4.2.2) into contact with the molecular layer. Each curve consists of an average of 20 sweeps taken at 100 000 mV/s. IV curves were taken at three different locations on the substrate the resultant median is displayed unless otherwise stated.

#### 4.2.7 Scanning Electron Microscopy

Modified conductive atomic force microscopy tips were imaged before and after usage by scanning electron microscopy (SEM) using a Hitachi S4800 Field Emmison SEM. Tips were imaged with a 10.0 kV accelerating voltage. In addition mixed-mode bonded layers were imaged using 1.0 kV accelerating voltage. SEM images were collected by Rongbing Du and Daniel Salamon.

### 4.3 Results and Discussion

#### 4.3.1 Template Stripped Gold

Scanning probe microscopy requires a firm understanding of how the tip interacts with the surface. Many factors such as, surface roughness, the surrounding medium, and tip shape govern tip-surface interaction and ultimately effect AFM measurements. Furthermore, variations within these factors alter this interaction making it difficult to compare measurements made between samples. Within conductive atomic force microscopy (cAFM), it is especially

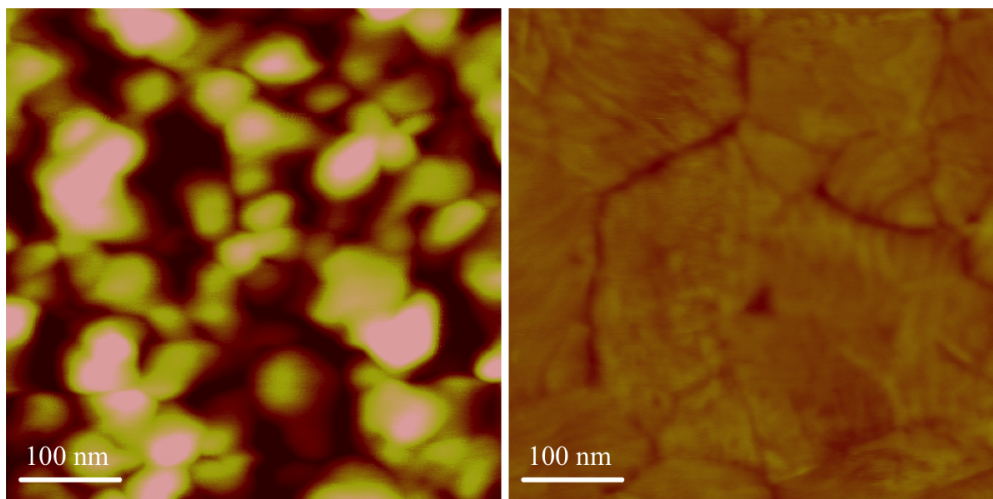


**Figure 4.3:** Atomic force microscopy height images of bare (left) thermal evaporated gold (right) template stripped gold. Z-scale 10 nm.

important to have low topographic roughness to minimize changes in contact area between measurements[29]. It is from this that template stripped (TS) gold is pursued as a way to reduce surface roughness compared to thermally evaporated gold substrates. Template stripped gold substrates were prepared by evaporating 300 nm of gold onto clean silicon wafers and bonding mounting substrates to the exposed gold surface. Template stripped substrates were then removed from the silicon wafer exposing the templated gold surface as needed. Figure 4.3 shows 500 nm<sup>2</sup> tapping mode height image of bare thermally evaporated gold substrate (left) and TS gold (right). It is evident that the thermal evaporated gold surface is significantly more rough than that of the TS gold. This is further shown by the root mean squared roughness of 2.3 nm and 0.2 nm, respectively over the 500 nm<sup>2</sup> area. In addition, it can be seen in Figure 4.3 that the size of each gold crystallite within TS gold is much larger than thermal evaporated gold. As a result molecular layers formed on the TS gold surface provides a more uniform surface for cAFM measurements due to the reduced roughness and large crystallites.

#### 4.3.2 Spectroscopic Characterization of Mix-Mode Bonded Layers

Thermal evaporated gold substrates were modified with a 250  $\mu$ M and 50 $\mu$ M nitroazobenzene (NAB) diazonium salt solution containing 0.05 M  $Bu_4NBF_4$  electrolyte within a three electrode cell by cycling the potential from 200 mV to -800 mV at various sweep rates: 10 mV/s, 50 mV/s, 100 mV/s and 200 mV/s. Similar to the results in previous

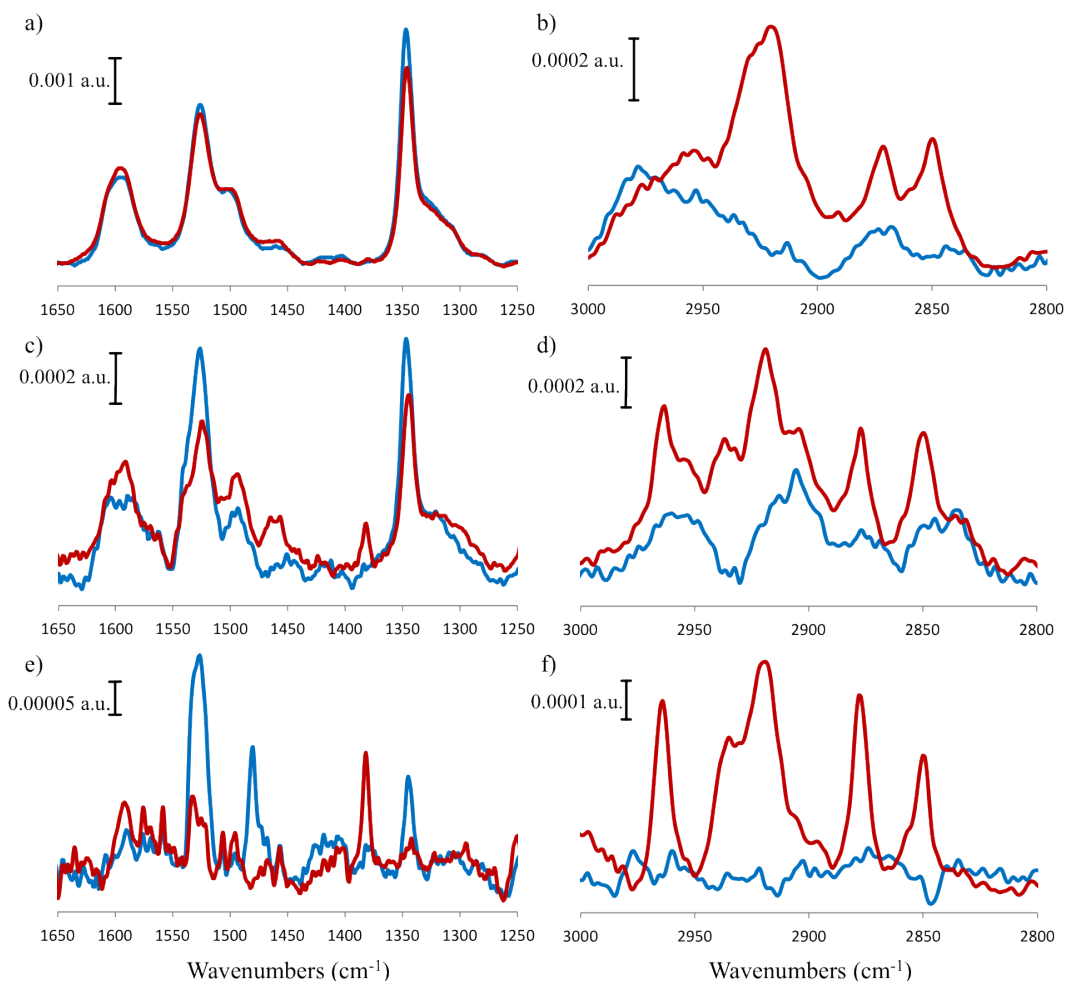


**Figure 4.4:** IRRAS spectra of (left)  $\text{NO}_2$  stretching region and (right) C-H stretching regions for NAB modified (blue) and NAB/DDT modified (red) molecular layers. (a,b)  $250 \mu\text{M}$  NAB at  $10 \text{ mV/s}$ , (c,d)  $250 \mu\text{M}$  NAB at  $200 \text{ mV/s}$ , (e,f)  $50 \mu\text{M}$  NAB at  $50 \text{ mV/s}$

chapters, each cyclic voltammogram (CV) displayed a large cathodic reduction peak and irreversible diazonium deposition. Substrates were then immersed in  $1 \text{ mM}$  dodecanethiol (DDT) solution overnight to produce mixed NAB/DDT modified surfaces. Infrared reflection absorption spectroscopy (IRRAS) was used to characterize surface modification before and after DDT incubation. Figure 4.4 displays IRRAS spectra of NAB modified (blue) and NAB/DDT modified (red) surfaces near the  $\text{NO}_2$  stretching and CH stretching regions of various samples. It can be seen that after NAB deposition, characteristic symmetric ( $\nu_{s\text{NO}_2} : 1347 \text{ cm}^{-1}$ ) and asymmetric ( $\nu_{a\text{NO}_2} : 1525 \text{ cm}^{-1}$ )  $\text{NO}_2$  stretches; are present. In addition, it is visible that slower sweep rates and higher concentrations produce larger  $\text{NO}_2$  peak intensities. Upon DDT surface modification (red), the  $\text{NO}_2$  peaks within the  $250 \mu\text{M}$

NAB depositions remain, indicating that NAB is maintained on the surface. The reduction in the  $\text{NO}_2$  peak intensity, seen in Figures 4.4(a) and (c), is attributed to the loss of loosely bond NAB during DDT immersion[30, 31], and is discussed further below. The 50  $\mu\text{M}$  NAB deposition, Figure 4.4e, shows that after DDT incubation the symmetric and asymmetric  $\text{NO}_2$  peaks are significantly reduced. Due to the low peak intensity and water background within the spectra, it is unclear if NAB remains on the surface and requires further characterization (see Section 4.3.3). Considering the CH stretching region of the mixed layers, Figures 4.4(b),(d) and (f), it is visible from the presence of the various  $\text{CH}_2$  ( $\nu_s$  : 2850  $\text{cm}^{-1}$ ,  $\nu_a$  : 2919  $\text{cm}^{-1}$ ) and  $\text{CH}_3$  ( $\nu_s$  : 2877  $\text{cm}^{-1}$ ,  $\nu_a$  : 2964  $\text{cm}^{-1}$ ) bands that DDT has self-assembled on the NAB modified gold surface. Within this region, the  $\text{CH}_2$   $\nu_a$  stretching peak position serves as a diagnostic for order within the alkanethiol layer[32]. Higher peak positions ( $> 2920 \text{ cm}^{-1}$ ) suggest alkanethiols form a liquid-like state on the surface with no extended order. The position of the  $\text{CH}_2$   $\nu_a$  stretching peak (2921  $\text{cm}^{-1}$ ) in higher NAB coverages, Figure 4.4b, suggests disorder throughout the DDT layer. As a result, it can be considered that the covalently bound NAB structures interrupt extended alkanethiol chain packing, shifting the  $\text{CH}_2$   $\nu_a$  peak to higher values. On the other hand, lower  $\text{CH}_2$   $\nu_a$  stretching positions ( $> 2920 \text{ cm}^{-1}$ ) indicate that alkanethiol chain packing is well ordered. This is apparent for lower NAB coverages where peak position has shifted to 2919  $\text{cm}^{-1}$ , Figure 4.4f, indicating that DDT has formed more extended crystallin structures.

### 4.3.3 Topographic Characterizations of Mix-Mode Bonded Layers

Template stripped gold substrates were modified with a 250  $\mu\text{M}$  and 50 $\mu\text{M}$  NAB diazonium salt solution containing 0.05 M  $\text{Bu}_4\text{NBF}_4$  electrolyte within a three electrode o-ring cell by cycling the potential from 200 mV to -800 mV at various sweep rates: 10 mV/s, 50 mV/s, 100 mV/s and 200 mV/s. After NAB deposition, modified substrates were immersed in a 1 mM dodecanethiol solution for 24 hours. To build upon spectroscopic results and to understand NAB structure within mixed NAB/DDT layers surface topography was investigated after each step of modification. Figure 4.5 shows 500  $\text{nm}^2$  tapping mode height images of NAB and DDT modified surfaces. The morphology of a DDT monolayer, Figure 4.5a, is significantly different from that of a NAB film, Figure 4.5b. During the self-assembly, the lability of the gold-sulfur bond allows for molecular re-arrangement of alkanethiols as surface densities increase, ultimately resulting in dense uniform monolayers[5]. As a result, the monolayer conform to the surrounding surface structure. This can be seen in Figure 4.5a

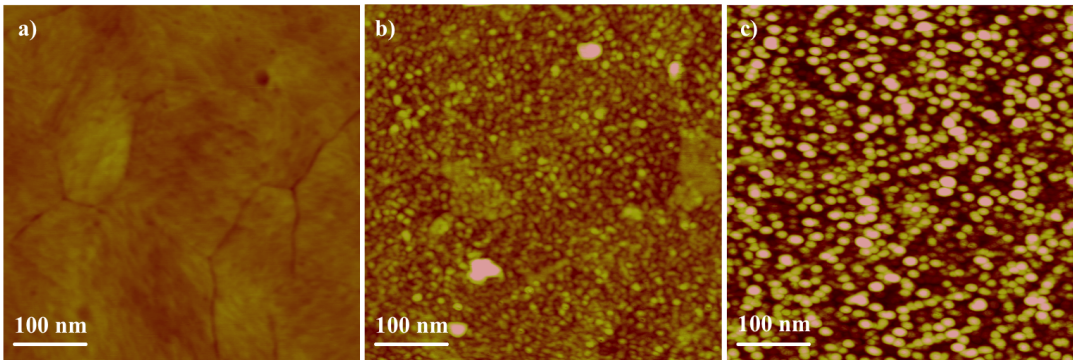


**Figure 4.5:** AFM height images of modified template stripped gold, a) dodecanethiol, b) nitroazobenzene c) mixed NAB/DDT layer. Z-scale 10 nm.

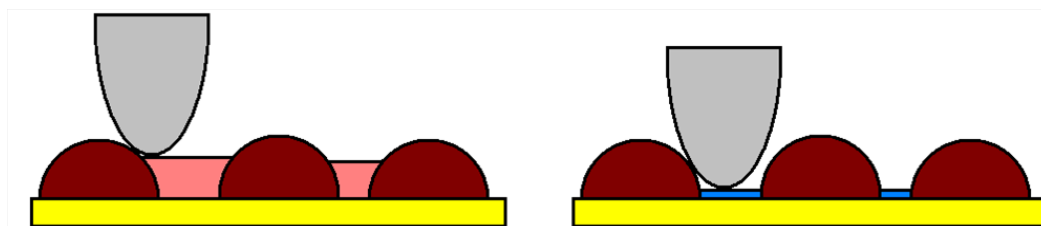


**Figure 4.6:** Schematic representing the influence of surrounding material on size measurements in AFM

where the underlying gold grain boundaries are visible. In contrast, Figure 4.5b indicates that NAB adsorbs in a “knobular” or “bumpy” fashion forming small semi-spherical structures. Furthermore, the height of these structures ( 2.5 - 4 nm) indicate that NAB forms multilayers on the gold surface agreeing with previous chapters and literature[14, 33, 15]. Figure 4.5c displays an image of the resulting mixed NAB/DDT layer after DDT modification of the NAB surface similar to that in Figure 4.5b. The topography within Figure 4.5c, displays bumpy, semi-spherical structures similar to that of the NAB surface, Figure 4.5b, indicating that NAB remains on the surface, in agreement with IRRAS spectra and previous work within our group[31]. From this however, the NAB structures have become larger (4 - 7 nm) and more defined after DDT modification. This change can be explained by considering Figure 4.6 and the  $\text{NO}_2$  stretching region within the IRRAS spectra collected previously, Figure 4.4.

After DDT incubation (red) it can be seen that the intensity of the symmetric and asymmetric  $\text{NO}_2$  stretching peaks is reduced, implying that some NAB has been removed from the surface. Previously it has been shown that NAB physisorbs to electrode surfaces, adhering through brief rinsing and sonication treatments[30]. From this it is plausible that during

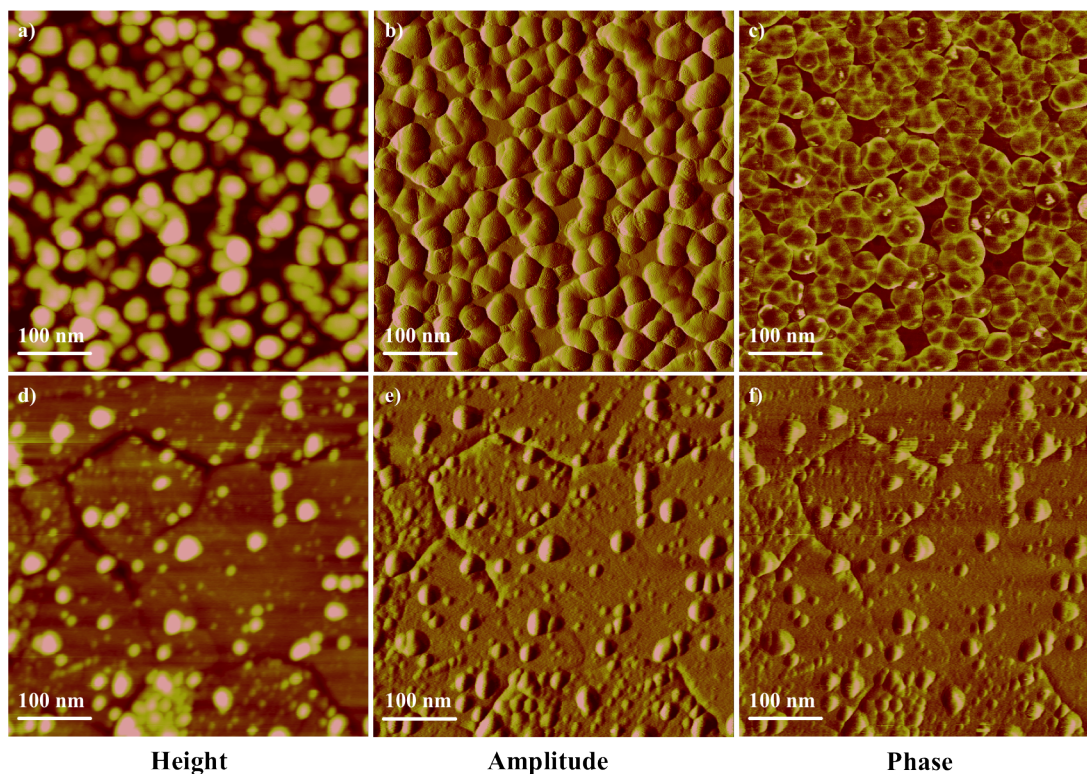


**Figure 4.7:** AFM images of NAB/DDT layer deposited at 200 mV/s from (top) 250  $\mu\text{M}$  NAB solution, (bottom) 50  $\mu\text{M}$  NAB solution. Height, amplitude and phase images are displayed for each concentration with z-scales of 10 nm, 0.1 V and  $30^\circ$  respectively.

electrochemical modification, NAB forms both covalently attached molecular structures[34] as well as loosely bound physisorbed species[30]. As a result, physisorbed molecules on the surface convolute AFM images of NAB by reducing the measured height of the covalently bound structures relative to the surrounding species, Figure 4.6 (left). Immersing NAB surfaces in thiol solution for 24 hours replaces physisorbed NAB molecules with DDT on the gold surface. As a result, there is a greater height difference between NAB and the DDT monolayer, Figure 4.6(right), subsequently increasing the measured size of the NAB structures. Furthermore, it is also possible that adsorption of DDT acts to “squeeze” NAB on the surface altering its structure and increasing the height of the covalently bound species as discussed further below.

Figure 4.7 shows height, amplitude and phase shift images of 250  $\mu\text{M}$  (Figure 4.7a, b, c) and 50  $\mu\text{M}$  (Figure 4.7d, e, f) NAB mixed NAB/DDT layers deposited at 200 mV/s. Tapping mode AFM images are collected by rastering an oscillating (kHz) cantilever over the surface. Height information is collected as the piezo extends or retracts the sample in order to maintain constant oscillation amplitude. However, amplitude images can be

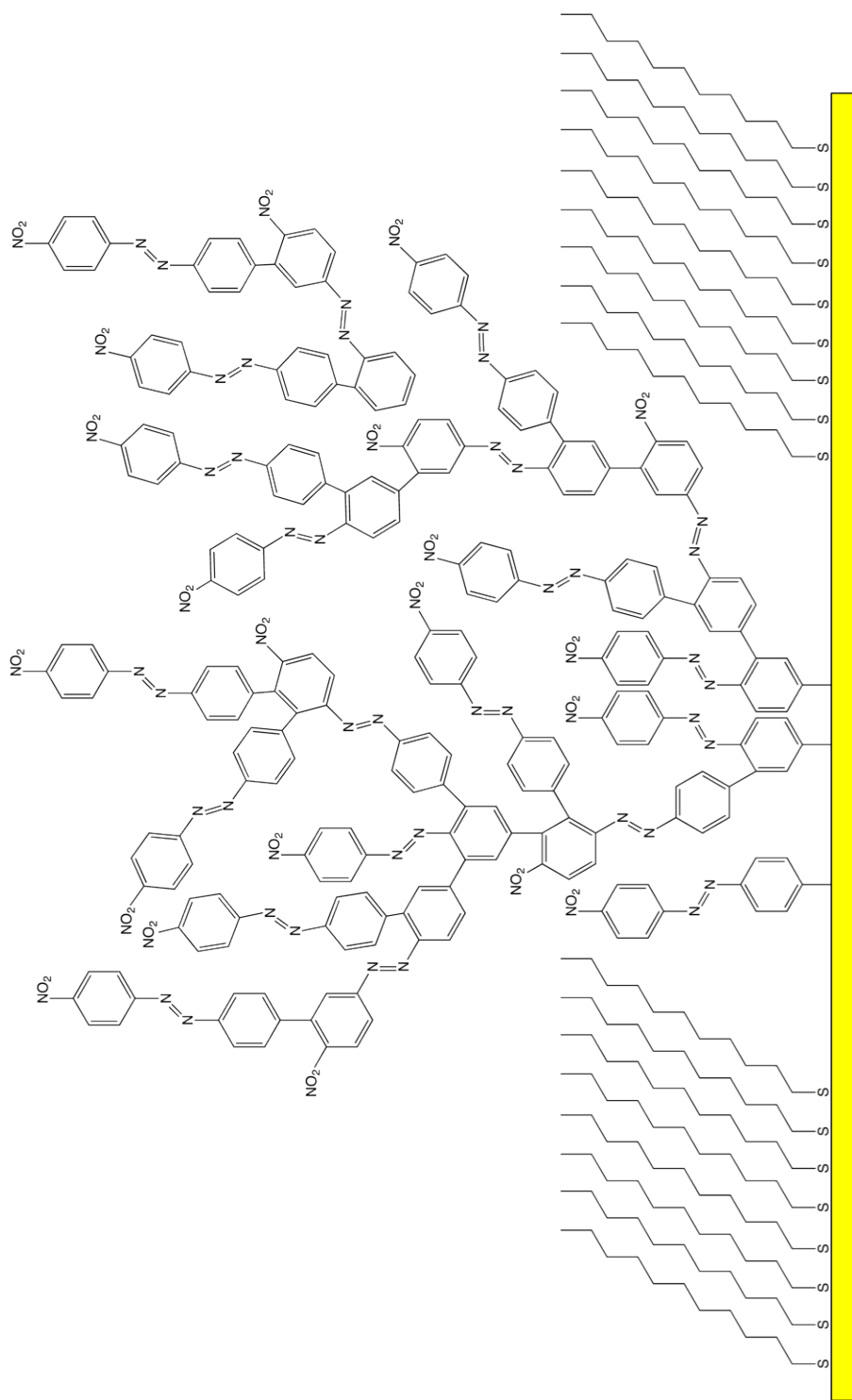


**Figure 4.8:** Schematic representation of mixed NAB/DDT structure

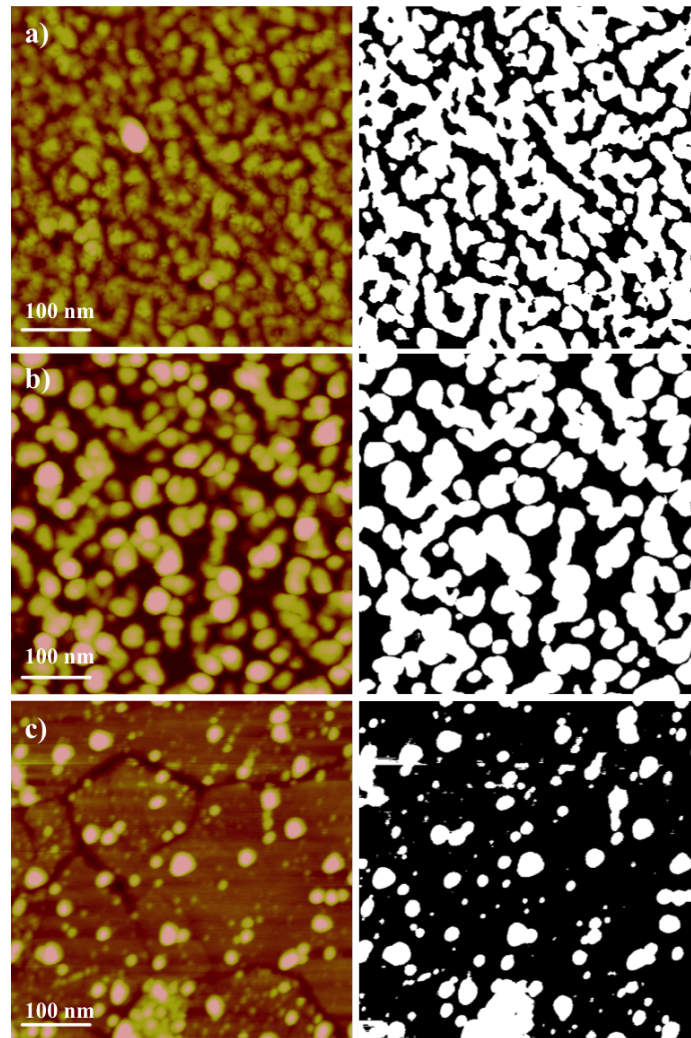


**Figure 4.9:** AFM height images of mixed NAB/DDT layers along with their respective thresholded images deposited by a) 250  $\mu\text{M}$  NAB at 100 mV/s, b) 250  $\mu\text{M}$  NAB at 200 mV/s, c) 50  $\mu\text{M}$  NAB at 100 mV/s. Z-scale 10 nm.

**Table 4.1:** Calculated percent diazonium coverage as determined by AFM, for 50  $\mu\text{M}$  and 250  $\mu\text{M}$  NAB mixed NAB/DDT layers

Concentration	10 mV/s	50 mV/s	100 mV/s	200 mV/s
50 $\mu\text{M}$	77	68	51	20
250 $\mu\text{M}$	NA	74	64	59

collected due to the fact that gains are finite and changes in amplitude do occur. The phase shift image is collected by monitoring the change (or shift) in cantilever oscillation relative to the drive frequency. As the tip interacts with the sample, energy is dissipated to the surface creating a phase shift and providing information about the mechanical and/or adhesive properties of the surface.

From Figure 4.7 semi-spherical NAB structures form in submonolayer densities on the gold surface. From the 250  $\mu\text{M}$  mixed layer, Figures 4.7(a-c), it is apparent that NAB covers the majority of the surface, however there exist lower (height) regions in which it is believed that DDT self-assembles (more clearly seen in Figures 4.7(b) and (c)). In addition, the difference in phase shift between the two regions, Figures 4.7(c) and (f), indicate different mechanical and/or adhesive properties of the two species further confirming the presence of a mixed molecular layer. As a result of the high NAB coverage, DDT molecules are forced to conform to the structure of the NAB, reducing the crystallinity of the thiol layer and shifting the  $\text{CH}_2 \nu_a$  peak higher, Figure 4.4b. In contrast, the 50  $\mu\text{M}$  NAB deposition, Figure 4.7(d-f), shows low density NAB within large areas of DDT. As a result, DDT is allowed to form more extended crystalline (less liquid-like) monolayers within the mixed layer as indicated position of the  $\text{CH}_2 \nu_a$  peak, Figure 4.4e, in the 50  $\mu\text{M}$  deposition. Furthermore, within the Figures 4.7(a) and (d) various sizes of NAB structures are visible, ranging in height between 1-4 nm for smaller species and 6-10 nm for larger species. Upon considering film thicknesses of similar NAB films (2-5 nm, Section 4.3.5) it is apparent that the NAB structure has been altered within the mixed NAB/DDT layer. To understand how NAB structure is effected by DDT adsorption, the stress within the layer must be considered. Godin *et al.* observed that the forces that occur during DDT self-assembly were sufficient to deflect a gold coated AFM cantilever. In addition it was found that gold surfaces with large grains (such as TS gold) undergo significantly more deflection than smaller grained surfaces[35]. As a result, it is not unreasonable to assume that the NAB on the surface will be exposed to similar forces during DDT adsorption. As DDT layer density increases the drive to produce extended well ordered crystalline-like layers “squeezes” NAB structures increasing their height. Figure 4.8 displays a schematic representation of the proposed mixed NAB/DDT layer.

In order to approximate the percentage of diazonium derived molecules on the surface, AFM height images were processed by selecting a pixel intensity threshold to visually isolate the NAB structures from the surrounding DDT monolayer. The threshold was chosen such that surface coverage calculations were consistent throughout the samples. Height and

threshold images are shown in Figure 4.9. Table 4.1 shows the calculated percent NAB coverage of various mixed NAB/DDT layers. NAB surface density decreases with higher sweep rate and lower concentrations. It should be noted that, due to tip broadening within AFM measurements, the percent NAB determined will be over estimated. However, changes in surface coverage for various film preparation conditions are valid in a relative sense.

Previous work on patterned SAMs has shown that SEM can provide contrast between two chemically distinct regions[24, 23, 36]. High resolution SEM was used to further characterize mixed NAB/DDT layers. Figure 4.10a shows a secondary electron SEM image of a 250  $\mu\text{M}$  NAB mixed layer deposited at 200 mV/s within the o-ring deposition area. In order to interpret the different regions displayed in 4.10a, the interaction volume and electron scattering process must be considered. During SEM measurements, accelerated electrons interact within a small region at the materials surface. The volume in which this interaction occurs is on the order of nanometers and is dependent on the composition of the sample, Figure 4.11a [37]. Secondary electrons, generated through inelastic scattering, can escape the material only from the upper-most region of the interaction volume. As a result, the signal obtained from secondary electrons is highly surface sensitive, providing topographic information of the sample. Furthermore due to the small escape depth,  $\lambda$ , of secondary electrons, features at an angle to the electron beam axis provide a larger escape volume than those normal to the beam axis Figure 4.11b[37]. Approximating the angle of the feature to be  $45^\circ$  volume is increased by a factor of  $\sqrt{2}$  compared to surfaces normal to the electron beam. Based on these concepts, it can be assumed that the semi-spherical NAB structures within the mixed organic layer will generate more secondary electrons than the DDT monolayer, and provide a higher (brighter) signal on the SEM image. The root of the contrast within the SEM images is not strictly understood but is considered to result from; impurities on the surface, desorption of these impurities by the electron beam or damage to the molecular layer by the primary or secondary electrons[36]. As a result the bright circular species seen in Figure 4.10a are assigned to NAB structures within the mixed layer. This is supported by Figure 4.10b, where the edge (outside the o-ring) of the TS gold sample was imaged. In this region the lack of contrast and topographic features indicate that a single molecular species is present. As a result of the topography and the visible TS gold grain boundaries it can be assumed the only DDT is present. Furthermore, within 4.10b there is varying contrast between the TS gold crystallites. It is not entirely clear what effects the contrast, but could result from different molecular orientations within the DDT layer. Note

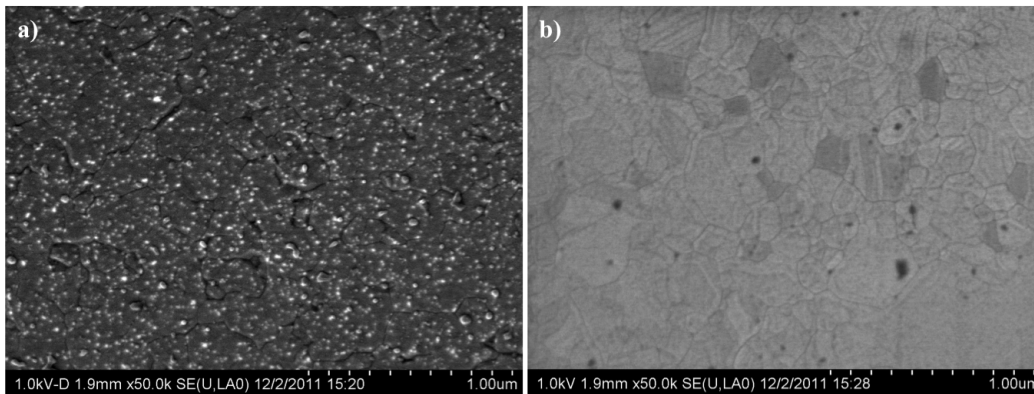


**Figure 4.10:** High resolution secondary electron SEM images of mixed layers deposited from 250  $\mu\text{M}$  NAB at 200 mV/s a) inside the o-ring NAB deposition area b) outside NAB deposition region that contains only a monolayer of DDT.

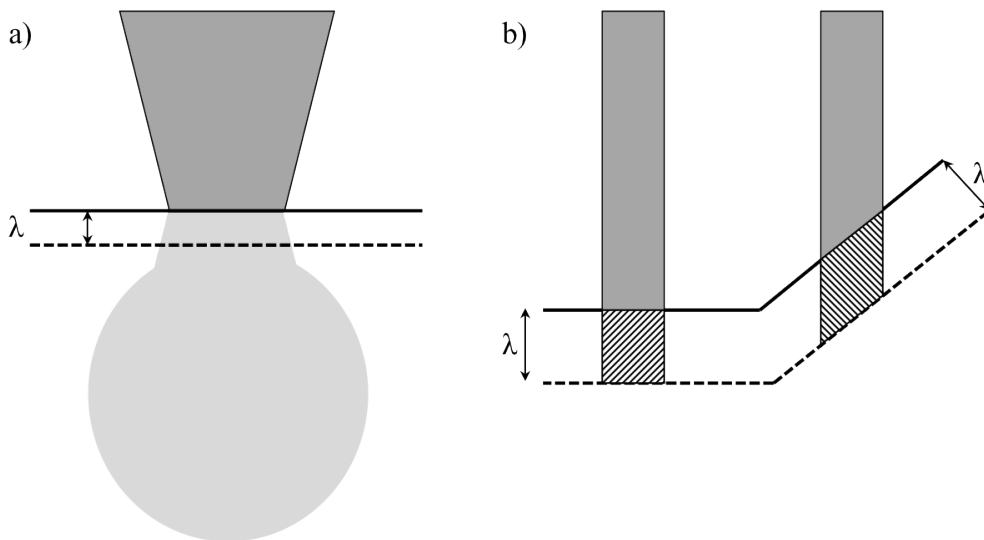


**Figure 4.11:** Schematic representation of a) interaction volume and b) secondary escape volume, in SEM imaging. Within b) it can be seen that angled samples produce larger secondary electron escape volumes.

that a direct comparison between Figure 4.10(a) and (b) is not entirely valid due to the different contrast mechanisms between the regions[36].

#### 4.3.4 Characterization of Fabricated cAFM Tips

In order to make electrical contact with the molecular layer silicon nitride AFM tips were modified by thermally depositing 3 nm of chromium and 45 nm of gold. Unmodified and metallized tips; were imaged by high resolution SEM, Figures 4.12(a, b) and Figures 4.12(c, d), respectively to study the topography of the metallized tips.. Following the procedure outlined in Section 2.3.3 tip radii were calculated to be  $27 \pm 10$  nm and  $51 \pm 9$  nm for unmodified and gold coated tips, in agreement with similar tip procedures in literature [38]. Furthermore, it visible from Figures 4.12(b) and (c) that the surface topography has been altered after metal deposition. As a result, it was determined that the silicon nitride tips were successfully modified and proceeded to investigate molecular junctions of organic layers on gold.

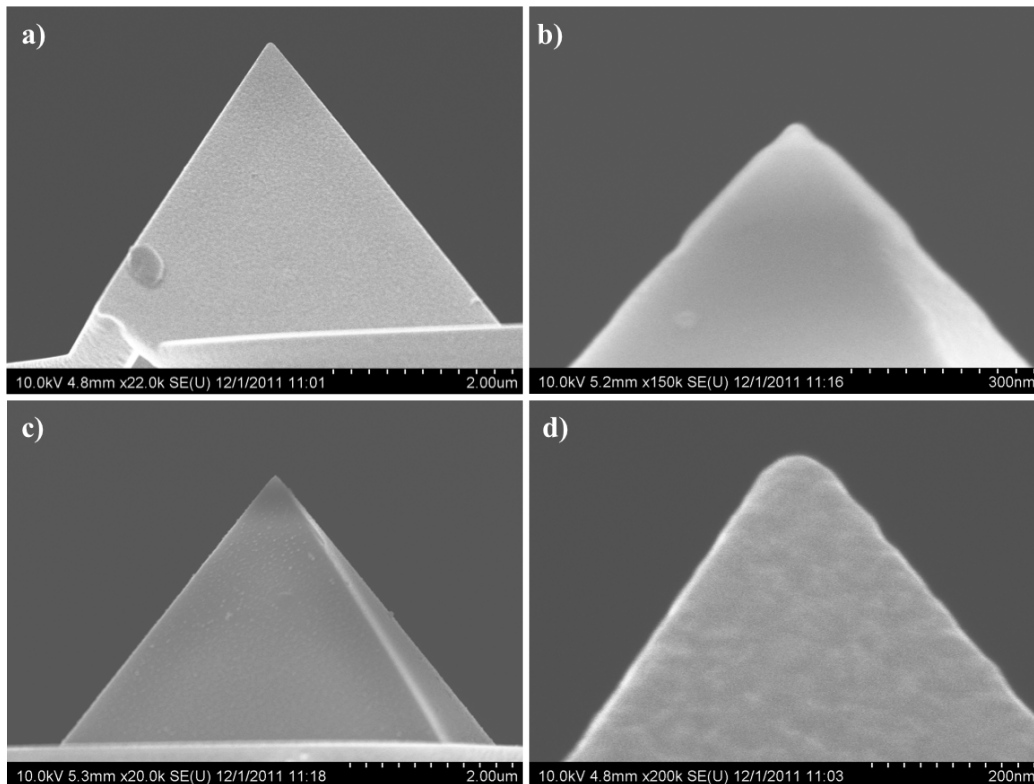


**Figure 4.12:** High resolution secondary electron SEM images of (top) bare and (bottom) gold modified silicon nitride AFM tips

#### 4.3.5 Electron Transport Through Molecular Layers on Gold

Conductive atomic force microscopy (cAFM) was used to investigate electron transport through molecular layers of NAB and DDT on template stripped gold in order compare to measurements made on PPF (Section 2.3). Similar to previous sections NAB films were deposited electrochemically from 250  $\mu\text{M}$  NAB diazonium salt solution at 50 mV/s, 100 mV/s and 200 mV/s. Film thicknesses were determined by AFM to be 5.1 nm, 4.6 nm and 3.0 nm respectively. Monolayers of DDT were deposited by incubating template stripped gold surfaces in 1 mM solution of DDT for 24 hours. Current Voltage (IV) measurements were taken in air under ambient conditions for DDT and various film thicknesses of NAB at constant force. Measurements were taken by cycling the voltage 20 times from -2 V to 2 V for NAB and -0.5 to 0.5 for DDT at 100 000 mV/s at three locations on each sample. Unless otherwise stated the curves below are an average of 20 cycles. Figure 4.13 displays IV curves of NAB on gold at various film thicknesses. It can be seen that current voltage behaviour on gold is similar to that of NAB molecular junctions on PPF (Section 2.3). Considering the curve for the 3.0 nm film, current increases linearly through low voltage ranges ( $\pm 0.25$  V), followed by non-linearity at higher potentials. Similar behaviour is observed throughout the various film thicknesses, however it is evident that the linear region extends over larger potentials for thicker films. It is to be expected that tunneling distance, contact area and penetration depth will play a role in determining IV behaviour within the cAFM measurements, however, under constant force it is considered that contact area and penetration depth do not significantly change (see Table 2.1). As a result, the various current responses seen in Figure 4.13 can be attributed to the differences in effective tunneling distance between samples.

As discussed in Chapters 1 and 2, electron transport within molecular layers is believed to occur via tunneling through the highest occupied molecular orbital (HOMO) and the lowest occupied molecular orbital (LUMO). The efficiency and manner in which tunneling occurs is highly dependent on the nature and energies of the frontier orbitals. As a result, it is expected that due to the differences in molecule-substrate bonding and molecular structure, electron transport through molecular layers of NAB and DDT will be significantly different. Figure 4.14 shows an IV measurement of a DDT monolayer on TS gold from -0.5 V to 0.5 V. This displays nearly linear IV behavior over the entire potential window, consistent with literature [3]. It should be noted however, in literature non-linear current behaviour

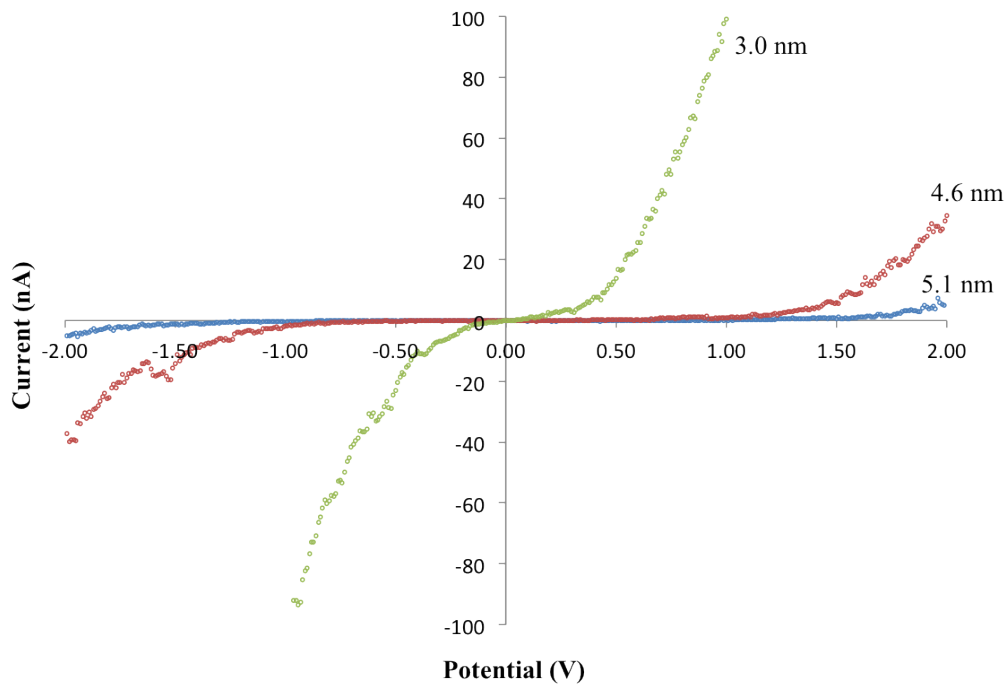


**Figure 4.13:** Current voltage curve of NAB on template stripped gold for various film thicknesses

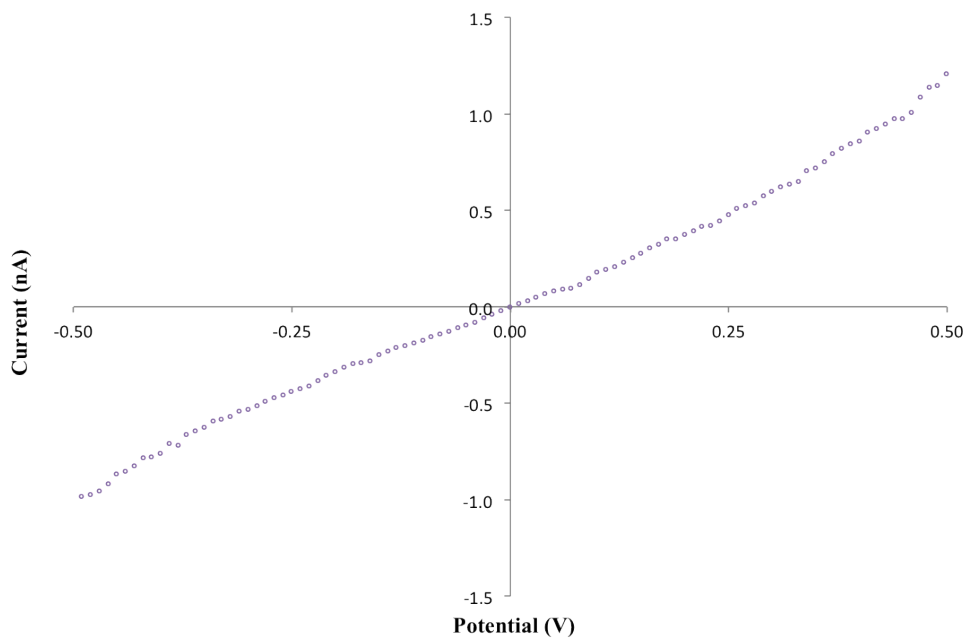


**Figure 4.14:** Current voltage curve for DDT on template stripped gold

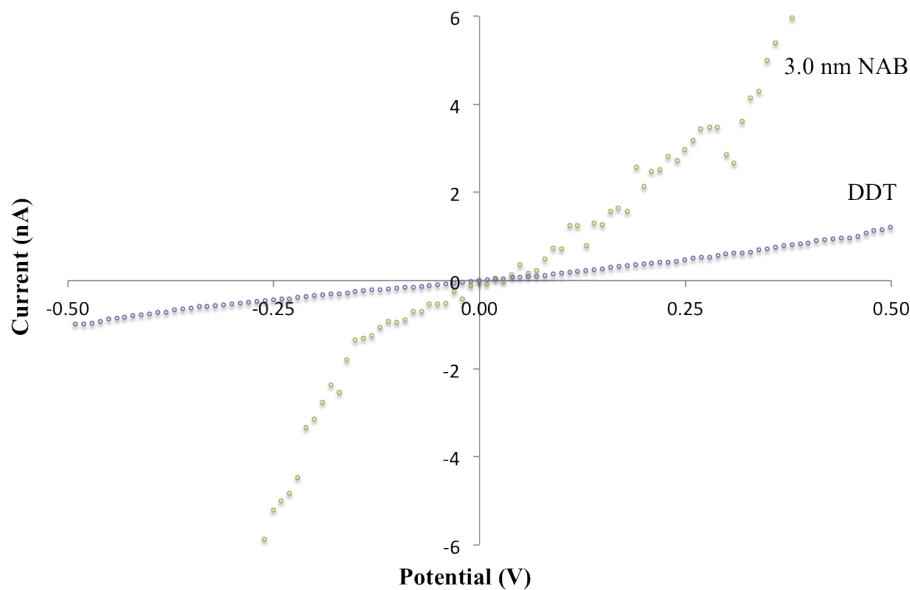


**Figure 4.15:** Current voltage curve for 3.0 nm NAB film and DDT monolayer

is seen at higher potentials [3, 39]; but to avoid junction breakdown[3] -0.5 V to 0.5 V was chosen here. Figure 4.15 displays IV measurements of the 3.0 nm NAB film and the DDT monolayer. It may be unclear why current response is significantly reduced compared to that of NAB due to the fact that tunneling distance is reduced through the DDT layer ( $\sim 2$  nm) [32, 40]. This can be understood by considering bonding structure and frontier orbital energies of the layers.

In molecular junctions of NAB on PPF, tunneling properties such as the attenuation coefficient,  $\beta$ , have been well characterized[41, 42, 43]. It is unclear however, whether there exists structural, chemical or energetic differences that would alter electron transport within junctions composed of different contact materials. Figure 4.16a displays a  $\ln|I|$  vs *Film Thickness* plot for NAB molecular junctions on gold taken at 0.5V. From this, the attenuation coefficient was determined to be  $2.6 \text{ nm}^{-1}$ , similar to values obtained on PPF in Section 2.3 and literature[41, 42, 20]. As a result, because  $\beta$  is highly dependent on structural properties of the layer[42, 41], it is apparent that the nature of film growth within NAB on gold does not differ significantly from that of growth on PPF. This is further demonstrated by Figure 4.16b and Table 4.2 where 3.0 nm NAB IV curve (red) has been fitted to an adapted Simmons model as discussed previously. Note that the current through the 4.6 nm and 5.1 nm NAB layers in the  $\pm 0.5$  V range was insufficient to apply the Simmons model.

The dielectric constant,  $\varepsilon$ , effective electron mass,  $m_e$ , and the transport barrier height,  $\phi_o$ , for the 3.0 nm NAB layer and for DDT were determined, Table 4.2. The results for NAB were found to be in good agreement with molecular junctions on PPF found in literature[43] and values presented in Chapter 2. The transport barrier height can be considered as a gauge of the offset between the HOMO of the NAB layer and the Fermi level of the electrodes. As result, it is apparent that the difference between frontier orbital energies and the Fermi level for molecular layers on PPF and gold are consistent, implying that electrode material has little effect on electron transport.

In order to understand the difference between electron transport through DDT and NAB, Figure 4.15, the structural and energetic properties of the organic layers were compared. Firstly, it can be seen that the attenuation coefficient of NAB ( $\sim 2.5 \text{ nm}^{-1}$ ) is radically different from the accepted,  $\beta$  value for alkanethiols,  $11 \text{ nm}^{-1}$ [3]. This provides the basis as to why the current through the DDT layer is significantly reduced from that of NAB. Furthermore the Simmons model was used to model IV behaviour within molecular junctions of DDT, Figure 4.16b (purple). From Table 4.2 it can be seen the effective electron mass,  $m_e$ , agrees between the layers, implying that electron mobility is similar within each organic film. There are however, distinct differences between the values of  $\varepsilon$  and  $\phi_o$  obtained for DDT and NAB. The dielectric constant of the DDT monolayer (2.14) is in good agreement with values obtained in previous studies [44] but significantly less than that of NAB. Considering the work by McCreery *etal*[20], who measured the dielectric constant of 2.2 nm NAB films to be 2.7, the large discrepancy between the molecular species can be attributed to differences of molecular layer thickness. In addition, from the Simmons model the transport barrier height was found to be 4.90 eV for the DDT monolayer, in agreement with measured (ultraviolet photoelectron spectroscopy) values of  $\sim 5 \text{ eV}$  for similar alkanethiols[39]. Recall that the electron transport barrier height,  $\phi_o$ , can be considered as the off-set between the frontier orbital energies and the Fermi level of the contacts ( $E_f - E_{HOMO}$ ). From Table 4.2 it can be seen that the transport barrier of NAB is significantly less than the DDT monolayer increasing the resistance within the layer. Evidence of this can be seen in Figure 4.15 where current within the NAB layer is nearly 10 times that of DDT. There has been discussion in literature which indicates that the Simmons model is an inadequate method to determine electron transport properties through molecular junctions, due to the fact it can predict physically unreal values[39]. Furthermore, it is unlikely that individual molecular energies govern electron transport due to the crystalline-like packing in alkanethiols. Within these

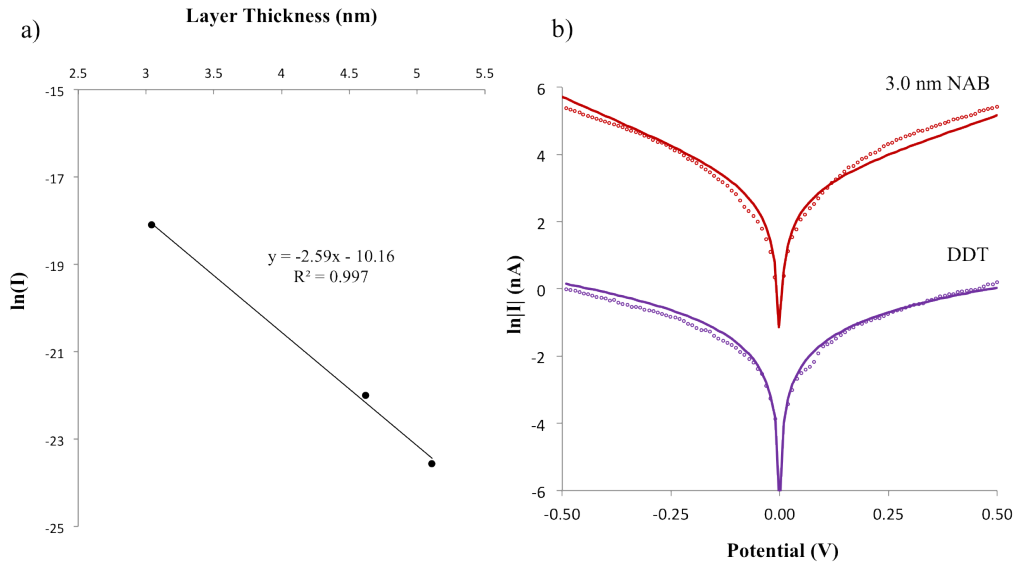


**Figure 4.16:** a)  $\ln(I)$  vs. *Layer Thickness* of NAB on template stripped gold measured at 0.5 V for  $\beta$  determination b)  $\ln|I|$  current voltage curves of (open circles: red) 3.0 nm NAB and (open circles: purple) DDT on template stripped gold along with their respective Simmons model fits (solid line)

**Table 4.2:** Values for dielectric constant,  $\epsilon$ , effective electron mass,  $m_e$ , and electron transport barrier,  $\phi_o$ , of 3.0 NAB and DDT as determined by the Simmons model.

Layer	$\epsilon$	$m_e$	$\phi_o$ (eV)
3.0 nm NAB	7.76	0.38	1.18
DDT	2.14	0.39	4.90

systems the density of states extends over the entire film altering the observed frontier orbital energies[39]. Many studies have described the electron transport barrier through alkanethiols to be  $\sim 1$  eV using the Simmons model[39, 45], indicating that alkanethiol orbital energies are much closer to the gold Fermi level than previously reported[46, 39]. As a result, it is not entirely clear whether the Simmons model is applicable for uniform or mixed molecular layers and will be discussed further below.

#### 4.3.6 Electron Transport Through Mixed-Mode Bonded Layers on Gold

Within the field of molecular devices adapting organic junctions to current electronics is a common goal. However, there exists a need to understand how these organic layers perform in conjunction with materials currently employed in the fabrication of electronic devices such as: silicon, gold and copper. From this, gold offers a route to investigate organic layers with different electrode bonding properties. Individually, diazonium derived and alkanethiol based molecular junctions have been well characterized [47, 3, 48, 49, 39, 33], however there has been little investigation into electron transport properties of mixed layers. Figures 4.17 and 4.18 display cAFM current voltage (IV) measurements of mixed NAB/DDT layers on template stripped gold with various NAB surface densities deposited from 250  $\mu\text{M}$  and 50  $\mu\text{M}$  NAB solutions respectively. NAB coverages were determined in Section 4.3.3 and are presented in Table 4.1. It is evident that NAB surface coverage has a significant effect on IV behaviour. Figures 4.17 and 4.18, show that surface coverage dominated by NAB ( $> 60\%$ ) produce larger, more rapid current responses over the  $\pm 2$  V range. It is expected that the majority of electron transport occurs through the NAB molecular layer producing current magnitudes similar to the NAB only molecular junctions. It is unclear however to what extent tunneling occurs through DDT, due to the attenuation (reduced electron transport) from the increased NAB height (tunneling distance) in mixed layers. Further, as the NAB surface coverage decreases, it is evident that current travelling through the molecular junction is also reduced. This can be understood by considering that at lower NAB densities, a more significant portion of electron transport will occur through the DDT layer. The large attenuation coefficient ( $\sim 11 \text{ nm}^{-1}$ ) and electron transport barrier ( $\sim 5$  eV) limits tunneling through the DDT layer, resulting in low current magnitudes within the mixed NAB/DDT layer.

Within Figure 4.19 it is visible that IV measurements of similar densities, 64% and 68%, produce nearly equivalent final currents (current at 2.00 V). From this however, it

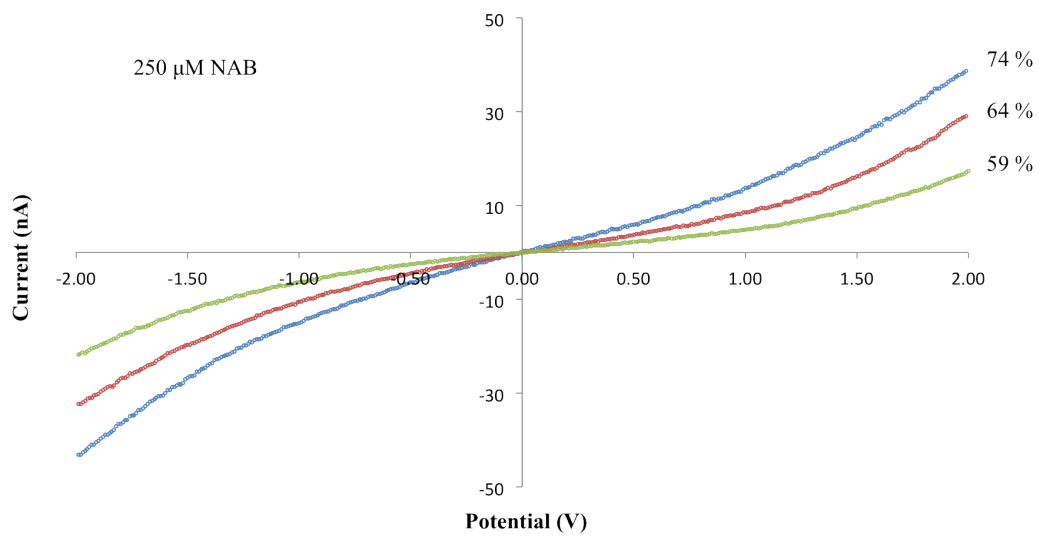


**Figure 4.17:** Current voltage measurements of mixed NAB/DDT at various NAB densities deposited from 250 μM NAB solution

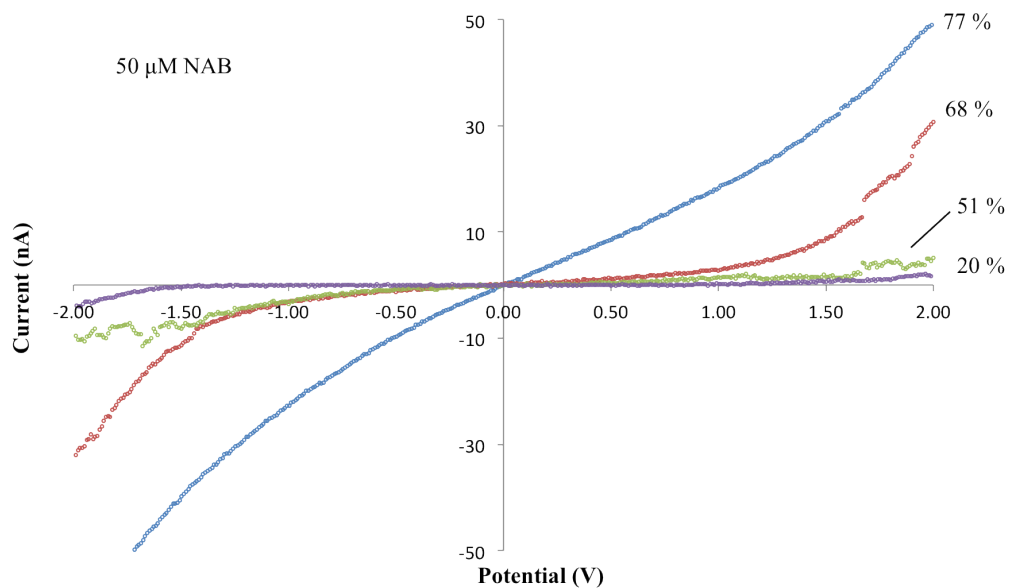


**Figure 4.18:** Current voltage measurements of mixed NAB/DDT at various NAB densities deposited from 50 μM NAB solution

can be seen that IV behaviour between the curves is distinct. The 50  $\mu\text{M}$  68% NAB curve current increases minimally over  $\pm 1$  V from which rapid non-linear current response occurs. Comparatively, the transition between linear and non-linear current response occurs much more gradually within the 250  $\mu\text{M}$  64% NAB curve. It is unclear as to why different IV behaviour is seen in similar NAB coverages, but could possibly result from changes in contact area of the cAFM probe, reduced tunneling distances or differences in NAB structure.

In comparison to other molecular junctions on PPF where “smooth” surface topography allows for a firm understanding of film thickness, mixed NAB/DDT layers produce irregular surfaces in which the layer thickness is not entirely clear. From the heights determined in Section 4.3.3 (1 - 4 nm and 6 - 10 nm) tunneling distance was approximated to 5 nm in order to use the Simmons model to determine the electron transport properties of mixed NAB/DDT layers. Figure 4.20 displays  $\ln|I(nA)|$  against *Potential* plot for the 250  $\mu\text{M}$  NAB mixed film along with their respective fits from the Simmons model. Note that the noise within IV measurements of lower NAB densities inhibited application of the Simmons model over the potential window ( $\pm 0.5$  V). From Table 4.3 it can be seen that the dielectric constant is fairly consistent throughout the various surface coverages, and reflects measurements of NAB on PPF[20] and gold. Similarly, it appears that the effective electron mass within the mixed layer does not significantly change with NAB surface coverage indicating that electron mobility is constant throughout the mixed layers. The electron transport barrier,  $\phi_o$ , appears not to follow any trend with surface densities and lies between the values determined for pure NAB ( $\sim 1$  eV) and DDT ( $\sim 5$  eV) layers. As a result, it is not unreasonable to assume qualitatively, that the electron transport barrier of the mixed NAB/DDT layers will be an average of the NAB and DDT frontier orbital energies. The extent to which each molecular energy is expressed requires a firmer understanding of contact area and tunneling distances.

#### **4.3.7 Inconsistencies within cAFM Measurements of Mixed Mode Bonded Layers**

Conductive AFM measurements require a strong understanding of surface topography. Changes in tunneling distance and contact area; will play a significant role in determining the electron transport properties. Within IV measurements of NAB molecular layers on PPF and TS gold, the uniform nature of the surface allowed for consistent contact area and firm understanding of tunneling distance. Mixed-mode bonded layers however, have been shown

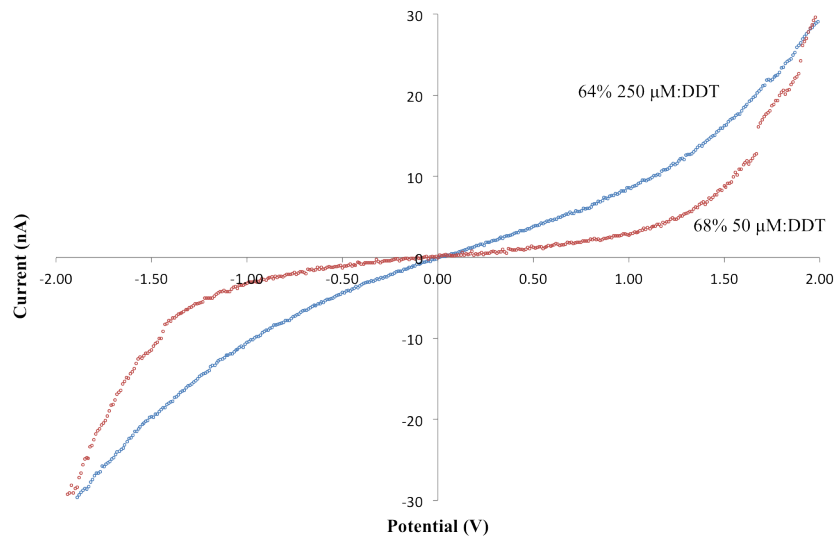


**Figure 4.19:** Current voltage measurements of mixed NAB/DDT layers with 64% and 68% NAB coverages

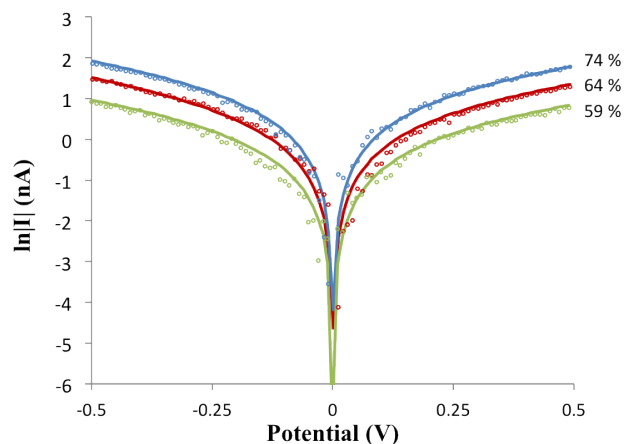


**Figure 4.20:**  $\ln(I)$  current voltage measurements (open circles) of mixed NAB/DDT films with Simmons model fit (solid line) deposited from 250  $\mu\text{M}$  NAB solution

% NAB Coverage	$\epsilon$	$m_e$	$\phi_o$
68 (50 $\mu\text{M}$ )	8.28	0.04	4.68
77 (50 $\mu\text{M}$ )	8.28	0.06	2.48
74 (250 $\mu\text{M}$ )	9.46	0.04	3.99
64 (250 $\mu\text{M}$ )	9.05	0.05	3.56
59 (250 $\mu\text{M}$ )	7.09	0.04	4.81

**Table 4.3:** Values for dielectric constant,  $\epsilon$ , effective electron mass,  $m_e$ , and electron transport barrier,  $\phi_o$ , of mixed NAB/DDT films at various NAB percent coverages as determined by the Simmons model

produce irregular surface topography regardless of the underlying substrate. The semi-spherical nature of NAB growth on TS gold results in a non-uniform interface as shown in Figure 4.7. Thus, the contact area of the tip can no longer be approximated by a sphere contacting a flat surface and cannot be considered uniform throughout IV measurements. Within each IV measurement it is not directly apparent which molecular species is making contact with the cAFM probe. Furthermore with the incorporation of DDT into the mixed layer stress is applied to the NAB species on the surface. NAB structures were found to increase in height significantly and range in size from 1 - 10 nm. The consequence is that the tunneling distances can vary greatly between IV measurements and it is difficult to de-convolute the effect of tunneling distance and NAB density. Further, within the mixed layers studied, NAB and DDT were found to exist in separate phases and were not uniformly deposited over the surface. The work of McCreery and coworkers[20] found that the offset between the Fermi level and the HOMO of NAB varied with film thickness, frontier orbital energies will not only differ between the species in the layer, but be unique to each structure. From this and the varying tunneling distance, the Simmons model cannot accurately determine the transport barrier height from cAFM measurements.

In order to completely understand electron transport within mixed diazonium and alkanethiol layers, contact area and tunneling distance need to be firmly understood. Possible routes to achieve this could encompass; larger area molecular junctions where contact area is strictly controlled and mixed layers where molecular species are more uniformly dispersed.

#### **4.3.8 Modified cAFM Tip Stability**

It was frequently observed during IV measurements on gold, that the electrical contact between the cAFM probe and the molecular layer was lost. In Chapter 2 it was found that current densities were such that irreversible damage to the metallized tip resulted in device failure. During the investigations of molecular junctions on gold it was unclear whether “in house” modified tips suffered from similar instabilities. Figure 4.21 shows a high resolution SEM image of a used cAFM tip. It is clear that the tip has sustained significant damage after IV measurements. Within Figure 4.21a it appears that the gold has melted similar to cAFM measurement of NAB on PPF (Figure 2.16). As a result, it was determined that loss of cAFM conductivity was due irreversible tip damage as discussed in Section 2.3.5.

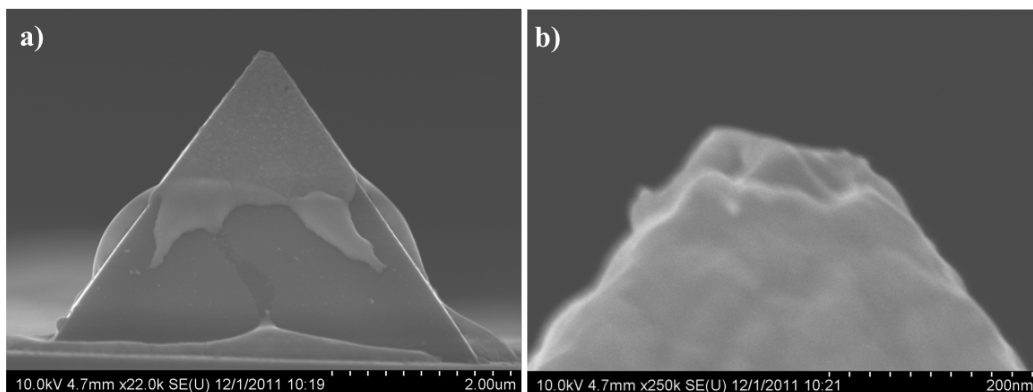


**Figure 4.21:** High resolution secondary electron SEM images of used “in house” modified cAFM tips using 10.0 kV

#### 4.3.9 Conclusion

Electron transport through molecular layers on gold were investigated by cAFM. Mixed organic films were produced by depositing NAB electrochemically and spontaneously adsorbing DDT. Surfaces were characterized by IRRAS, SEM and AFM. It was found that NAB formed submonolayer covalent semi-spherical structures, while DDT self-assembled conforming around the NAB structures. The density of NAB on the surface was found to be controllable through concentration and sweep rate. Electron transport properties of NAB on gold were determined to be consistent with similar junctions on PPF. Furthermore electron transport through DDT was found to agree with literature. Conductive AFM investigation into mixed NAB/DDT layers established that IV behaviour varied with NAB surface density. However, it was determined that quantitative comparison of electron transport properties require further investigation due to the unknown contact area and tunneling distances within the mixed layers.

## References

- [1] Neudeck, P.; Okojie, R.; Chen, L. *Proceedings of the IEEE* **2002**, *90*, 1065–1076.
- [2] McMillan, P. F. *Nature materials* **2002**, *1*, 19–25.
- [3] Wold, D. J.; Frisbie, C. D. *Journal of the American Chemical Society* **2001**, *123*, 5549–56.
- [4] Laibinis, P. E.; Whitesides, G. M.; Allara, D. L.; Tao, Y. T.; Parikh, A. N.; Nuzzo, R. G. *Journal of the American Chemical Society* **1991**, *113*, 7152–7167.
- [5] Vericat, C.; Vela, M. E.; Benitez, G.; Carro, P.; Salvarezza, R. C. *Chemical Society reviews* **2010**, *39*, 1805–34.
- [6] Gooding, J. J.; Ciampi, S. *Chemical Society reviews* **2011**, *40*, 2704–18.
- [7] Halik, M.; Klauk, H.; Zschieschang, U.; Schmid, G.; Dehm, C.; Schütz, M.; Maisch, S.; Effenberger, F.; Brunnbauer, M.; Stellacci, F. *Nature* **2004**, *431*, 963–6.
- [8] Love, J. C.; Estroff, L. a.; Kriebel, J. K.; Nuzzo, R. G.; Whitesides, G. M. *Self-assembled monolayers of thiolates on metals as a form of nanotechnology.*, 2005; Vol. 105.
- [9] Nuzzo, R.; Allara, D. *Journal of the American Chemical Society* **1983**, *105*, 4481–4483.
- [10] Beebe, J. M.; Engelkes, V. B.; Liu, J.; Gooding, J. J.; Eggers, P. K.; Jun, Y.; Zhu, X.; Paddon-Row, M. N.; Frisbie, C. D. *The journal of physical chemistry. B* **2005**, *109*, 5207–15.
- [11] Beebe, J. M.; Kim, B.; Frisbie, C. D.; Kushmerick, J. G. *Journal of the American Chemical Society Nano* **2008**, *2*, 827–832.
- [12] Garrett, D. J.; Lehr, J.; Miskelly, G. M.; Downard, A. J. *Journal of the American Chemical Society* **2007**, *129*, 15456–7.
- [13] Adenier, a.; Barre, N.; Cabetdeliry, E.; Chausse, a.; Griveau, S.; Mercier, F.; Pinson, J.; Vautrinul, C. *Surface Science* **2006**, *600*, 4801–4812.
- [14] Shewchuk, D. M.; McDermott, M. T. *Langmuir : the ACS journal of surfaces and colloids* **2009**, *25*, 4556–63.
- [15] Kariuki, J. K.; McDermott, M. T. *Langmuir* **2001**, *17*, 5947–5951.

- [16] Delamar, M.; Hitmi, R.; Pinson, J.; Saveant, J. *Journal of the American Chemical Society* **1992**, *114*, 5883–5884.
- [17] Liang, H.; Tian, H.; McCreery, R. L. *Applied spectroscopy* **2007**, *61*, 613–20.
- [18] Jayasundara, D. R.; Cullen, R. J.; Soldi, L.; Colavita, P. E. *Langmuir* **2011**.
- [19] Ceccato, M.; Bousquet, A.; Hinge, M.; Pedersen, S.; Daasbjerg, K. *Chemistry of Materials* **2011**, 110218074748045.
- [20] Bergren, A.; McCreery, R.; Stoyanov, S.; Gusarov, S.; Kovalenko, A. *The Journal of Physical Chemistry C* **2010**, 15806–15815.
- [21] Bonifas, A. P.; McCreery, R. L. *Nature nanotechnology* **2010**, *5*, 612–7.
- [22] Salaita, K.; Amarnath, A.; Maspoch, D.; Higgins, T. B.; Mirkin, C. a. *Journal of the American Chemical Society* **2005**, *127*, 11283–7.
- [23] López, G. P.; Biebuyck, H. a.; Frisbie, C. D.; Whitesides, G. M. *Science (New York, N.Y.)* **1993**, *260*, 647–9.
- [24] Wollman, E.; Frisbie, C. D.; Wrighton, M. S. *Langmuir* **1993**, 1517–1520.
- [25] Tamada, K.; Hara, M.; Sasabe, H.; Knoll, W. *Langmuir* **1997**, *13*, 1558–1566.
- [26] Brooksby, P. a.; Downard, A. J. *Langmuir : the ACS journal of surfaces and colloids* **2005**, *21*, 1672–5.
- [27] Leroux, Y. R.; Hui, F.; Noël, J.-M.; Roux, C.; Downard, A. J.; Hapiot, P. *Langmuir : the ACS journal of surfaces and colloids* **2011**, *27*, 11222–8.
- [28] Blackstock, Jason J., Li, Zhiyong, Freeman, Mark R., Stewart, Duncan, R. *Surface Science* **2003**, *546*, 87–96.
- [29] Engelkes, V. B.; Beebe, J. M.; Frisbie, C. D. *The journal of physical chemistry. B* **2005**, *109*, 16801–10.
- [30] Kuo, T.-C. *Electrochemical and Solid-State Letters* **1999**, *2*, 288.
- [31] Shewchuk, D. M.; Reid, M.; Mcdermott, M. T.
- [32] Porter, M. D.; Bright, T. B.; Allara, D. L.; Chidsey, C. E. D. *Journal of the American Chemical Society* **1987**, *109*, 3559–3568.

- [33] Anariba, F.; DuVall, S. H.; McCreery, R. L. *Analytical chemistry* **2003**, *75*, 3837–44.
- [34] Laurentius, L.; Stoyanov, S. R.; Gusarov, S.; Kovalenko, A.; Du, R.; Lopinski, G. P.; McDermott, M. T. *ACS nano* **2011**, *5*, 4219–27.
- [35] Godin, M.; Williams, P. J.; Tabard-Cossa, V.; Laroche, O.; Beaulieu, L. Y.; Lennox, R. B.; Grütter, P. *Langmuir : the ACS journal of surfaces and colloids* **2004**, *20*, 7090–6.
- [36] Lopez, G. P.; Biebuyck, H. A.; Whitesides, G. M. *Langmuir* **1993**, 1513–1516.
- [37] Egerton, R. F. *Principles of Electron Microscopy An introduction to TEM, SEM, and AEM*; Springer: New York, 2005.
- [38] Skulason, H.; Frisbie, C. D. *Langmuir* **2000**, *16*, 6294–6297.
- [39] Engelkes, V. B.; Beebe, J. M.; Frisbie, C. D. *Journal of the American Chemical Society* **2004**, *126*, 14287–96.
- [40] Kondo, T.; Yanagida, M.; Shimazu, K.; Uosaki, K. *Langmuir* **1998**, *14*, 5656–5658.
- [41] Yang, H.-H.; McCreery, R. L. *Analytical Chemistry* **1999**, *71*, 4081–4087.
- [42] Anariba, F.; Steach, J. K.; McCreery, R. L. *The journal of physical chemistry. B* **2005**, *109*, 11163–72.
- [43] Bergren, A. J.; McCreery, R. L. *Annual review of analytical chemistry (Palo Alto, Calif.)* **2010**, *4*, 173–95.
- [44] Wang, B.; Luo, J.; Wang, X.; Wang, H.; Hou, J. G. *Langmuir : the ACS journal of surfaces and colloids* **2004**, *20*, 5007–12.
- [45] Wang, W.; Lee, T.; Reed, M. a. *Reports on Progress in Physics* **2005**, *68*, 523–544.
- [46] Alloway, D. M.; Hofmann, M.; Smith, D. L.; Gruhn, N. E.; Graham, A. L.; Colorado, R.; Wysocki, V. H.; Lee, T. R.; Lee, P. a.; Armstrong, N. R. *The Journal of Physical Chemistry B* **2003**, *107*, 11690–11699.
- [47] Yan, H.; Bergren, A. J.; McCreery, R. L. *Journal of the American Chemical Society* **2011**.
- [48] McCreery, R. L. *Chemistry of Materials* **2004**, *16*, 4477–4496.

- [49] McCreery, R. L.; Wu, J.; Kalakodimi, R. P. *Physical chemistry chemical physics* : *PCCP* **2006**, *8*, 2572–90.

## 5 Conclusions and Future Work

### 5.1 Conclusions

Bridging the gap between single molecule molecular junctions and large scale ensembles, conductive atomic force microscopy provides a crucial insight into the scalability of molecular devices. The work presented has detailed the use of cAFM to study electron transport through small scale diazonium derived junctions as well as mixed-mode bonded layers. Investigations into electron transport through nitroazobenzene on carbon surfaces revealed that current voltage behaviour was consistent nonresonant tunneling as seen in large scale ensembles studied by McCreery *et al*[1]. Similarly, the electron transport properties, as determined by the Simmons model, were in agreement with larger molecular junctions suggesting that electron transport is indeed scaleable. Furthermore, investigation of the effect of force on electron transport revealed that the bonding structure of the molecular layer was maintained and changes in tunneling current were a result of reduced tunneling distances (tip penetration), and increased contact area.

Further electrochemical studies of nitroazobenzene on gold demonstrated that not only were multilayers formed but molecular layer growth could be controlled by sweep rate and solution concentration. Electron transport studies demonstrated that current voltage behaviour of nitroazobenzene on template stripped gold was consistent with molecular layers on carbon suggesting that the work function of the contacts has little effect on the electron transport properties of the layer. In addition to diazonium derived molecular layers, mixed-mode bonded layers involving dodecanethiol and nitroazobenzene were characterized. Spectroscopic and surface probe measurements demonstrated that the percent coverage of nitroazobenzene could be readily controlled by concentration and sweep rate. In addition, incorporation of dodecanethiol within the mixed-mode bonded layer increased the height of the diazonium regions, resultant of “squeezing” during monolayer formation. Although many studies have investigated electron transport through mixed layers, much of this work has focused on the same molecule-contact bond[2, 3, 4, 5, 6]. The work presented here demonstrates the first investigation of electron transport through mixed diazonium-thiol molecular junctions. Qualitatively it was observed that the conductivity increased with nitroazobenzene density, but further investigation into contact area and tunneling distance are needed to fully characterize electron transport.

The findings presented within this work have expanded the understanding of electron

transport through diazonium derived molecular layers, by investigating the current voltage behaviour of nitroazobenzene under the effect of applied force and varying contact material. Furthermore the implementation of mixed-mode bonded layers presents new interesting routes for electron transport studies and molecular device development.

## 5.2 Future Work

The cAFM studies presented within this work have provided insight into the effects of applied force and contact material on electron transport through molecular layers of nitroazobenzene. McCreery and coworkers have investigated molecular junctions formed by a number of other diazonium salts including nitrobenzene, fluorene, biphenyl and nitrobiphenyl[7, 8]. Similarly to the work on nitroazobenzene, cAFM can further add to the understanding of the scalability of molecular junctions formed with other diazonium salts. In addition to new molecular layers, high thickness diazonium films are being explored. Our group has demonstrated control over molecular layer thickness from submonolayer to 100s of nanometers. Using cAFM to form molecular junctions of high thickness provides the unique opportunity to apply force to the surface. Potentially researchers would be able to monitor current as the tip penetrates the layer. From this, fundamental transport mechanisms, such as tunneling distance and molecular rearrangement can be explored.

In addition to diazonium derived molecular layers, the work presented here has provided the first surface probe characterization of mixed-mode bonded layers. The unique and interesting structure of these layers offer many exciting possibilities for not only molecular electronic devices, but other fields such as surface assays. Compared to the lability of SAMs, diazonium layers offer a much more stable platform in which to bind biological molecules such as proteins[9, 10, 11]. By using mixed mode-bonded layers researchers can control the surface density of binding sights to optimize device performance. Further, by selecting specific functional groups for the surrounding thiol molecules, not only can non-specific binding be prevented but additional (and different) binding sights can be deposited.

In order to extend the understanding of electron transport through mixed mode bonded layers, further characterization of the molecular junction is needed. Specifically, the uncertainty associated with the tunneling distance and contact area must to be addressed. An an important aspect of this will be selectively placing the tip at a particular location on the surface. Within the AFM measurements above, the stability of the molecular layer restricted

imaging to non-contact methods. As a result, conductive imaging was not possible as the molecular layer would be removed from the surface (as seen in “scratching” experiments). From this, STM may provide a route in which conductive images can be obtained, due to the fact that the probe does not make contact with the surface. Furthermore, by using this technique, specific regions of the layer can be chosen in which to form molecular junctions and analyze current voltage behaviour. Although, tip-molecule distance will serve to convolute electron transport, STM will provide further insight into transport mechanisms.

As discussed in Chapter 4 it is unclear how the incorporation of the alkanethiol into the molecular layer affects the structure of the nitroazobenzene. It was proposed that the height of the diazonium structures was increased due to “squeezing” within the molecular layer. In order to study the interface between the species, it would be ideal to pattern the surface in an effort to have a controllable boundary. A common platform for studying mixed layers of SAMs is microcontact printing using poly(dimethylsiloxane) (PDMS) stamping techniques[12, 13, 14, 15]. Within this technique a stamp is used to deposit molecular species on the surface after which the open substrate is “backfilled” with another molecule. Downard and coworkers have demonstrated the use of microcontact printing using PDMS stamps to form patterned molecular layers derived from diazonium salts[16]. Using this, diazonium layers could be patterned on the surface in which thiol molecules can be backfilled creating a distinct boundary in which to study the structure of the molecular layer. Furthermore, in an effort to understand mixed-mode bonded layer formation, surfaces could be imaged in solution to monitor the deposition of thiol molecules and structural changes to diazonium species.

## References

- [1] Bergren, A.; McCreery, R.; Stoyanov, S.; Gusarov, S.; Kovalenko, A. *The Journal of Physical Chemistry C* **2010**, 15806–15815.
- [2] Cygan, M. T.; Dunbar, T. D.; Arnold, J. J.; Bumm, L. A.; Shedlock, N. F.; Burgin, T. P.; Li, L. J.; Allara, D. L.; Tour, J. M.; Weiss, P. S. *Journal of the American Chemical Society* **1998**, 7863, 2721–2732.
- [3] Donhauser, Z. J.; Mantooth, B. A.; Kelly, K. F.; Bumm, L. A.; Monnell, J. D.; Stapleton, J. J.; Price, D.; Rawlett, A. M.; Allara, D. L.; Tour, J. M.; Weiss, P. S. *Science* **2001**, 292, 2303–2307.
- [4] Hallbäck, A.-S.; Poelsema, B.; Zandvliet, H. J. W. *Chemphyschem : a European journal of chemical physics and physical chemistry* **2007**, 8, 661–5.
- [5] Wakamatsu, S.; Akiba, U.; Fujihira, M. *Colloids and Surfaces* **2002**, 200, 785–790.
- [6] Wassel, R. A.; Fuierer, R. R.; Kim, N.; Gorman, C. B.; Carolina, N. *Nano* **2003**, 3, 1617–1620.
- [7] McCreery, R. L.; Wu, J.; Kalakodimi, R. P. *Physical chemistry chemical physics : PCCP* **2006**, 8, 2572–90.
- [8] Yan, H.; Bergren, A. J.; McCreery, R. L. *Journal of the American Chemical Society* **2011**.
- [9] Polsky, R.; Harper, J. C.; Dirk, S. M.; Arango, D. C.; Wheeler, D. R.; Brozik, S. M. *Langmuir* **2007**, 23, 364–6.
- [10] Corgier, B. P.; Marquette, C. A.; Blum, L. J. *Journal of the American Chemical Society* **2005**, 127, 18328–32.
- [11] Harper, J. C.; Polsky, R.; Wheeler, D. R.; Lopez, D. M.; Arango, D. C.; Brozik, S. M. *Langmuir : the ACS journal of surfaces and colloids* **2009**, 25, 3282–8.
- [12] Wilbur, J. L.; Kumar, A.; Biebuyck, H. a.; Kim, E.; Whitesides, G. M. *Nanotechnology* **1996**, 7, 452–457.
- [13] Salaita, K.; Amarnath, A.; Maspoch, D.; Higgins, T. B.; Mirkin, C. a. *Journal of the American Chemical Society* **2005**, 127, 11283–7.

- [14] Love, J. C.; Estroff, L. a.; Kriebel, J. K.; Nuzzo, R. G.; Whitesides, G. M. *Self-assembled monolayers of thiolates on metals as a form of nanotechnology.*, 2005; Vol. 105.
- [15] Yan, L.; Zhao, X.-M.; Whitesides, G. M. *Journal of the American Chemical Society* **1998**, *120*, 6179–6180.
- [16] Garrett, D. J.; Lehr, J.; Miskelly, G. M.; Downard, A. J. *Journal of the American Chemical Society* **2007**, *129*, 15456–7.

## 6 Appendix

### 6.1 Simmons Model

The complete Simmons model as outlined by Simmons [1]:

$$J = c(A' + B' + C')$$

with

$$c = \frac{4\pi m_e q}{h^3}$$

where  $m_e$  and  $q$  are the effective electron mass and charge respectively  $h$  is Planck's constant and

$$A' = eV \int_0^{\eta - eV} \exp \sqrt{-A(\eta + \bar{\phi} - E_x)} dE_x$$

$$B' = -\bar{\phi} \int_{\eta - eV}^{\eta} \exp \sqrt{-A(\eta + \bar{\phi} - E_x)} dE_x$$

$$C' = \int_{\eta - eV}^{\eta} (\eta + \bar{\phi} - E_x) \times \exp \sqrt{-A(\eta + \bar{\phi} - E_x)} dE_x$$

where  $\eta$  is the Fermi level of the contacts and  $\bar{\phi}$  is the average barrier height.

$$A = \left( \frac{4\pi \Delta s}{h} \right) \sqrt{2m_e}$$

with  $\Delta s$  as the effective layer thickness. The solutions to the above integrals are given by Huisman *et al.* [2] yielding:

$$J = c(\tilde{A} + \tilde{B} + \tilde{C})$$

where  $\tilde{A}$ ,  $\tilde{B}$ ,  $\tilde{C}$  are solutions to  $A'$ ,  $B'$ ,  $C'$  respectively

$$\tilde{A} = \frac{2qV}{A^2} \left\{ \left( A\sqrt{\bar{\phi}} + qV + 1 \right) \exp \left( -A\sqrt{\bar{\phi} + qV} \right) - A \left( \sqrt{\eta + \bar{\phi}} + 1 \right) \exp \left( -A\sqrt{\eta + \bar{\phi}} \right) \right\}$$

$$\tilde{B} = \bar{\phi} \frac{2}{A^2} \left\{ \left( A\sqrt{\bar{\phi}} + 1 \right) \exp \left( -A\sqrt{\bar{\phi}} \right) - \left( A\sqrt{\bar{\phi} + qV} + 1 \right) \times \exp \left( -A\sqrt{\bar{\phi} + qV} \right) \right\}$$

$$\tilde{C} = \frac{2}{A} \left\{ \left( \bar{\phi}^{3/2} + \frac{3}{A}\bar{\phi} + \frac{6}{A^2}\sqrt{\bar{\phi}} + \frac{6}{A^2} \right) \exp \left( -A\sqrt{\bar{\phi}} \right) - \left( (\bar{\phi} + qV)^{3/2} + \frac{3}{A}(\bar{\phi} + qV) + \frac{6}{A^2}\sqrt{\bar{\phi} + qV} + \frac{6}{A^3} \right) \times \exp \left( -A\sqrt{\bar{\phi} + qV} \right) \right\}$$

The average barrier height is determined by:

$$\bar{\phi} = \phi_o - qV \left( \frac{s_1 + s_2}{2d} \right) - \left[ 1.15\lambda \frac{d}{s_1 - s_2} \right] \times \ln \left[ \frac{s_2(d - s_1)}{s_1(d - s_2)} \right]$$

where  $\phi_o$  is the unmodified barrier height and  $d$  is the thickness of the layer,  $s_1$  and  $s_2$  are the distances between the contact and the barrier at the Fermi level for each contact and

$$\lambda = \frac{q^2 \ln 2}{8\pi\epsilon_0\epsilon d}$$

where  $\epsilon_0$  is the permittivity of free space and  $\epsilon$  is the relative dielectric constant of the layer. Fits were obtained over the linear region of the curves (-0.5V - 0.5V) by least squares analysis in Excel. Initial values for the adjustable parameters,  $\epsilon$ ,  $\phi_o$  and  $m_e$  were set by considering the work by Bergren *et al.*[3]. In order to ensure physically realistic values parameters were bound on a case by case basis.

## 6.2 Conductive AFM Reproducibility

Figure 6.1 shows a representative unaveraged current voltage curve of NAB on PPF measured via cAFM.

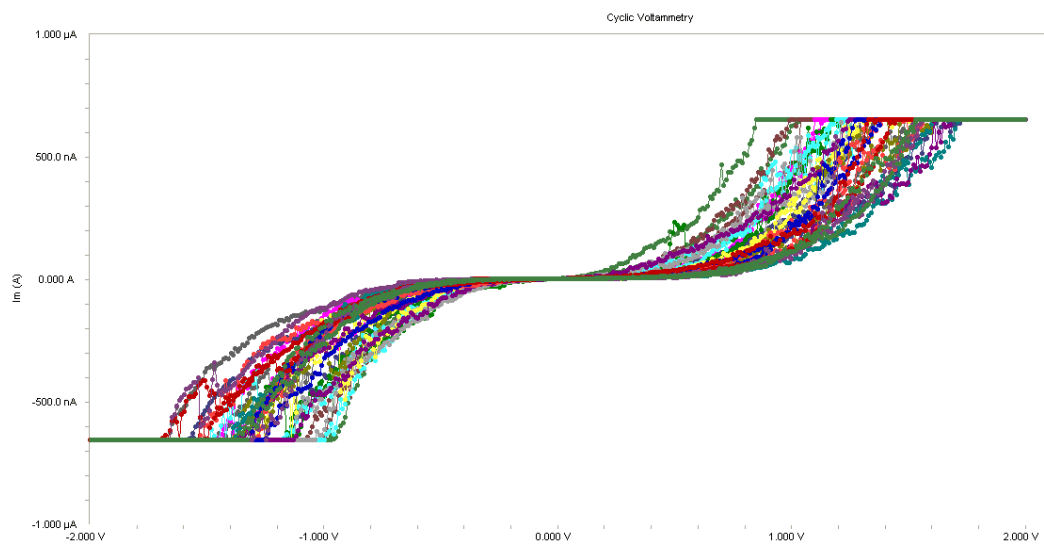


**Figure 6.1:** Representative unaveraged conductive atomic force microscopy current voltage curves

## References

- [1] Simmons, J. G. *Journal of Applied Physics* **1963**, *34*, 238.
- [2] Huisman, E. H.; Guédon, C. M.; van Wees, B. J.; van der Molen, S. J. *Nano letters* **2009**, *9*, 3909–13.
- [3] Bergren, A.; McCreery, R.; Stoyanov, S.; Gusarov, S.; Kovalenko, A. *The Journal of Physical Chemistry C* **2010**, 15806–15815.